HOKKAIDO UNIVERSITY

Title	Development of solvatochromic fluorophores incorporating boron complex and application for biothiols detection in live-cell imaging
Author(s)	張, 帥
Degree Grantor	北海道大学
Degree Name	博士(環境科学)
Dissertation Number	甲第16209号
Issue Date	2025-03-25
DOI	https://doi.org/10.14943/doctoral.k16209
Doc URL	https://hdl.handle.net/2115/94902
Type	doctoral thesis
File Information	ZHANG_Shuai.pdf

Hokkaido University Collection of Scholarly and Academic Papers : HUSCAP

Development of solvatochromic fluorophores incorporating boron complex and application for biothiols detection in live-cell imaging

ホウ素複合体を含むソルバトクロミック蛍光色素の開発と生体内細胞イメージングにおける生体チオール検出への応用

Zhang Shuai

Division of Development of Environmental Science

Graduate School of Environmental Science

Hokkaido University

A dissertation submitted for

the degree of Doctor of Philosophy

2025

Table of Contents

Chapter 1. General Introduction **3**

1.1 Overview of Luminescence 5

1.2 Introduction of Fluorescence Microscopy 8

1.3 Introduction of Fluorescent Probes 10

1.3.1 Cyanine-Based Fluorescent Dyes 12

1.4 Fluorescent Probes with Large Stokes Shift 15

1.4.1 Significance of large Stokes shift 15

1.4.2 Design strategies for large Stokes shift probes 16

1.5 Introduction of PET-Based Probes 22

1.5.1 Mechanism of PET-Based Probes 23

1.5.2 Strategy for PET-Based Probes 25

1.6 Importance of Biothiols Sensing 29

1.7 Objectives and Outline 31

1.7.1 Objectives 31

1.7.2 Outline 32

References 33

Chapter 2. Synthesis, Characterization and Biothiols Detection **47**

Abstract 48

2.1 Introduction 48

2.2 Materials, Instruments and Methods 50

2.3 Synthesis Scheme 51

2.4 Photophysical properties of PT/BT-Boc 63

2.5 Optimization of Spectroscopic Testing Conditions 66

2.6 Spectroscopic analysis of BT-DNBS towards biothiols 67

2.7 Selectivity analysis of BT-DNBS towards analytes 71

2.8 Time and pH-dependent spectra analysis 73

2.9 Sensing mechanism 75

2.10 Density functional theory (DFT) calculation 77
2.11 Reported Probes with a DNBS Group 79
2.12 Conclusion 81
References 82
Chapter 3. Cell Imaging **84**
Abstract 85
3.1 Introduction 85
3.2 Instruments and Methods 87
3.2.1 Cell culture 88
3.2.2 Cell viability assay 88
3.2.3 Fluorescent probe treatment 88
3.2.4 Thiol-blocking agent pre-treatment 89
3.2.5 Fluorescence Imaging 89
3.3 Results and Discussion 90
3.3.1 Cytotoxicity evaluation 90
3.3.2 Fluorescence response in cells 91
3.3.3 Effect of pre-treatment with NEM 96
3.4 Conclusion 98
References 99
Chapter 4. Summary and Conclusion **100**
Acknowledgment **103**

Chapter 1. General Introduction

Fluorescent probes are integral to the advancement of biological imaging, providing powerful tools for visualizing and tracking molecular events within living cells [1-3]. These probes have been widely applied in various areas of life sciences, including cell biology, molecular diagnostics, and drug development, owing to their ability to deliver real-time insights into complex biological systems [4-8]. Among the various targets for fluorescent probes, biothiols such as glutathione (GSH) and cysteine (Cys), are of particular importance due to their critical roles in maintaining cellular redox balance and protecting cells from oxidative damage [9]. Aberrations in biothiol levels are associated with a range of diseases, including cancer, neurodegenerative disorders, and metabolic syndromes [10].

One of the challenges in the field of fluorescence imaging is overcoming background noise and ensuring precise detection of target molecules [11]. Traditional fluorescent probes can suffer from issues such as small Stokes shifts, which lead to spectral overlap between the excitation and emission wavelengths, diminishing the clarity of the imaging [12]. Large Stokes shift probes, which exhibit a greater separation between these wavelengths, offer a solution by reducing background interference and improving signal resolution [13]. This improvement enhances the specificity and sensitivity of biomolecule detection, particularly in live-cell applications where autofluorescence and other sources of noise are prevalent [14].

The development of advanced fluorescent probes with optimized properties, such as large Stokes shifts, continues to play a crucial role in biological and medical research [15]. These innovations not only allow for clearer imaging of biomolecules in living systems but also contribute to our understanding of fundamental cellular processes and the molecular basis of diseases.

1.1 Overview of Luminescence

Luminescence refers to the emission of light by a substance that has absorbed energy, typically without a significant increase in temperature [16]. This phenomenon is widely utilized in fields such as analytical chemistry, materials science, and bioimaging. Based on the energy source and the underlying mechanisms, luminescence can be categorized into several types, including photoluminescence, chemiluminescence, electroluminescence, triboluminescence, and cathodoluminescence (Fig. 1.1).

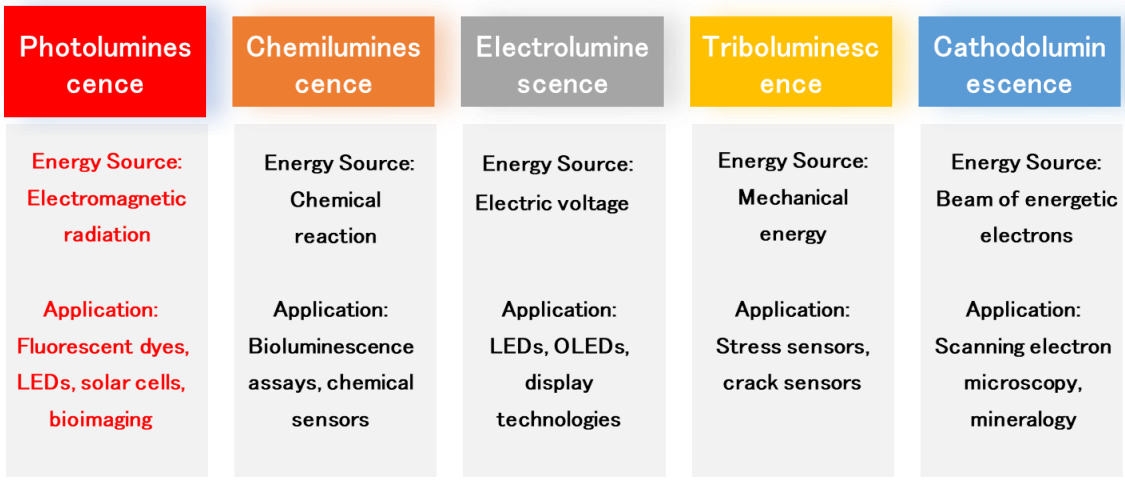


Fig. 1.1 Overview of luminescence types and applications.

Photoluminescence (PL) occurs when a material absorbs photons and re-emits them as light. This category is further divided into fluorescence and phosphorescence, depending on the timescale of emission and the involvement of spin states. Fluorescent dyes, such as cyanine and fluorescein, are widely used in imaging applications due to their high brightness and tunable emission [17]. The fast emission of fluorescence (nanoseconds) makes it ideal for real-time monitoring, while phosphorescence, with longer lifetimes, is more suited for time-resolved applications (Fig. 1.2).

Chemiluminescence (CL) results from a chemical reaction that generates an electronically excited state, which subsequently releases energy as light. It does not require an external light source, reducing background interference [18]. This property

makes it particularly useful in sensitive applications like immunoassays and forensic analysis. However, the limited availability of chemiluminescent compounds poses challenges.

Electroluminescence (EL) is the emission of light induced by an electric current or a strong electric field. It is the foundation of many modern display technologies, such as organic light-emitting diodes (OLEDs) [19]. The advantages of electroluminescence include low power consumption and high brightness, but the operational stability of electroluminescent devices remains a key area of research.

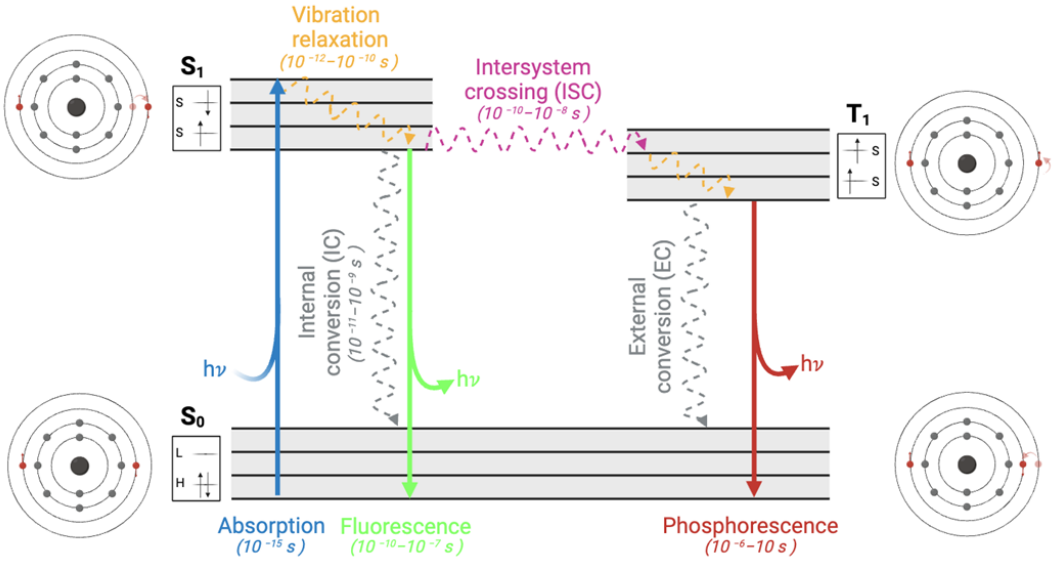


Fig. 1.2 Modified Jabłoński diagram.

Triboluminescence (TL) is a relatively rare phenomenon where light is emitted upon mechanical action, such as grinding, scratching, or fracturing of a material [20]. It has potential applications in stress sensing and material diagnostics, although its practical use is limited due to the low intensity and unpredictable nature of the emitted light.

Cathodoluminescence (CL) occurs when a material emits light upon excitation by an electron beam. This method is widely employed in electron microscopy to study the optical and electronic properties of materials at a nanoscale resolution [21]. Its main

drawback is the need for specialized equipment and a vacuum environment.

Among the various luminescence phenomena, photoluminescence, particularly fluorescence, has obtained significant attention due to its wide applicability in chemical sensing, biological imaging, and material science. Fluorescence occurs when a molecule absorbs photons and transitions to an excited electronic state, followed by radiative relaxation to the ground state. This emission process is highly sensitive to the molecular structure and surrounding environment, making it ideal for use in fluorescent dyes.

1.2 Introduction of Fluorescence Microscopy

Fluorescence microscopy is a widely used imaging technique in biological and chemical research, enabling the visualization of specific molecules, organelles, and biochemical processes within cells [22]. It relies on the selective detection of fluorescence emitted by fluorophores upon excitation by a specific wavelength of light, allowing for high-contrast imaging against a dark background. The key components of a fluorescence microscope include a light source, an excitation filter, a dichroic mirror, an emission filter, and a sensitive detector (Fig. 1.3).

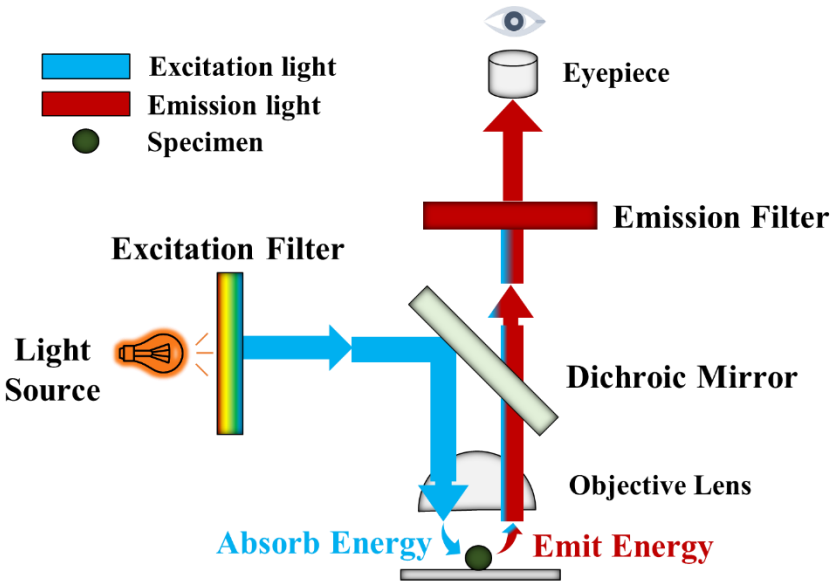


Fig.1.3 Mechanism of fluorescence microscope.

The optical system of a fluorescence microscope functions through a series of precise filtering and reflection processes to ensure that only the desired fluorescence signal is detected. First, the excitation light source, such as a mercury or xenon arc lamp, LED, or laser, produces a broad spectrum of light. This light passes through the excitation filter, which selects the specific wavelength needed to excite the fluorophore in the sample. The filtered excitation light is then directed toward the sample by a dichroic mirror (also called a dichroic beam splitter). This specialized mirror reflects the excitation light toward the objective lens while allowing longer-wavelength emitted fluorescence to pass through. As the fluorophores in the sample emit fluorescence, the emitted light travels back through the objective lens and reaches the dichroic mirror

again. Unlike excitation light, the emitted fluorescence has a longer wavelength, allowing it to pass through the dichroic mirror rather than being reflected. The emitted light then passes through the emission filter, which blocks any residual excitation light and allows only the desired fluorescence signal to reach the detector. Finally, the filtered fluorescence signal is captured by an imaging system, such as an eyepiece, a CCD/CMOS camera, or a photomultiplier tube (PMT) in confocal microscopes.

The combination of excitation and emission filters, along with the dichroic mirror, ensures that only fluorescence from the sample is detected, reducing background noise and improving image contrast. Advanced fluorescence microscopes, such as confocal and two-photon microscopes, further refine this process by eliminating out-of-focus light and improving spatial resolution. These optical principles make fluorescence microscopy an essential tool for studying intracellular processes, molecular interactions, and biochemical dynamics with high specificity and sensitivity [23].

1.3 Introduction of Fluorescent Probes

Fluorescent probes have transformed biological research by providing powerful tools to visualize and track molecular events in real-time within live cells [24]. Their ability to convert molecular interactions into measurable fluorescent signals has made them indispensable in both basic research and clinical diagnostics [25]. These probes work by interacting with target molecules or environments, producing detectable fluorescence that corresponds to specific biological events, such as the presence of particular ions, proteins, or small biomolecules (Fig.1.4) [26-28].

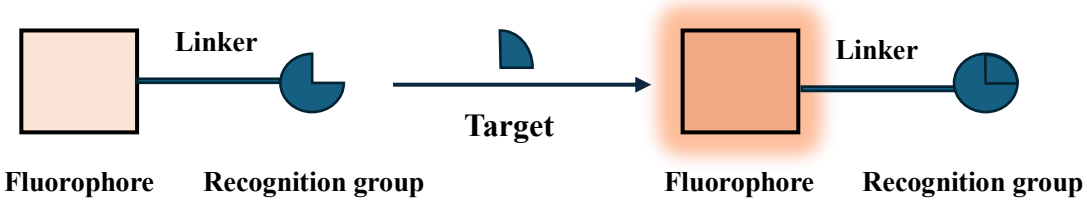


Fig.1.4 The structure of small molecule fluorophore probes.

The development of fluorescent probes dates back to the early use of natural fluorescent substances. However, the field truly advanced with the introduction of synthetic organic dyes, such as fluorescein and rhodamine (Fig. 1.5) [29,30]. These early dyes enabled researchers to label and observe specific biological molecules under the microscope. Over time, the field has evolved to produce a wide range of fluorescent probes tailored for different biological applications, from detecting calcium ions to visualizing cancer biomarkers [31,32].

Fluorescent probes are highly valued for their sensitivity, selectivity, and non-

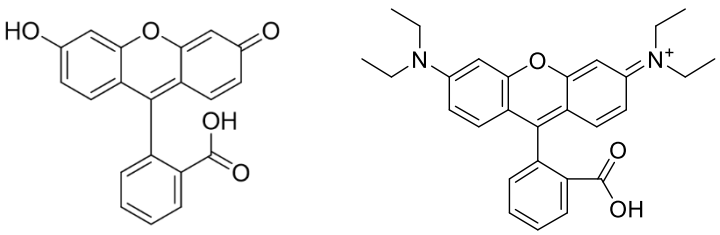


Fig.1.5 Typical small-molecule fluorophores, left: fluorescein, λ_{ex}=495 nm, λ_{em}=520 nm. Right: rhodamine B, λ_{ex}=550 nm, λ_{em}=626 nm.

invasive nature, making them ideal for live-cell imaging [33]. By providing the ability to detect molecules at low concentrations, they allow researchers to study intricate cellular processes with minimal disruption. In addition to cell biology, these probes are widely used in medical diagnostics for detecting disease markers and tracking the efficacy of treatments [34-36]. Modern advancements have expanded the scope of fluorescent probes to include more photostable, brighter, and responsive molecules. New designs allow for the detection of dynamic changes in the cellular environment, such as pH fluctuations [37], reactive oxygen species (ROS) production [38], and redox state variations [39]. The ability to fine-tune these probes to respond to specific biomolecular targets has enabled significant progress in areas like cancer research, neuroscience, and drug discovery [40-42]. Fluorescent probes also play a pivotal role in high-throughput screening technologies and imaging-based assays, where their sensitivity and selectivity make them invaluable for drug development [43]. Moreover, their capacity for multiplexed imaging, where several probes are used simultaneously, enables the observation of multiple molecular pathways at once, providing a more comprehensive view of cellular function [44].

As the field of fluorescent probes continues to evolve, there is a growing demand for dyes with specific properties to overcome limitations of traditional fluorophores. For instance, achieving longer emission wavelengths in the near-infrared (NIR) region has become a key goal, as it minimizes background interference from biological autofluorescence and enables deeper tissue penetration [45, 46]. Additionally, probes with large Stokes shifts are particularly sought after to reduce self-quenching and spectral overlap, improving signal-to-noise ratios in complex biological environments [47].

1.3.1 Cyanine-Based Fluorescent Dyes

Among the diverse classes of fluorophores, cyanine-based dyes have emerged as a prominent choice due to their tunable photophysical properties, high molar absorptivity, and bright fluorescence [48]. Their origins can be traced back to the mid-19th century, when they were first synthesized as textile dyes [49]. Over time, their unique photophysical properties captured the attention of the scientific community, and they began to be explored for use in various imaging applications. The development of cyanine-based fluorescent dyes has since progressed, becoming pivotal in modern fluorescence microscopy and bioimaging.

Structurally, cyanine dyes (Fig. 1.6) are characterized by a conjugated system in which two nitrogen-containing heterocycles are connected by a polymethine chain [50]. This structure is responsible for their vibrant fluorescence, as well as the ability to adjust their absorption and emission properties by modifying the length of the conjugated chain or substituents on the nitrogen atoms [51]. This tunability allows cyanine dyes to cover a broad spectral range, from the visible to near-infrared (NIR) regions, making them highly versatile for different imaging applications [52]. One of the most



n= 0, 1, 2, 3

Fig. 1.6 Schematic illustration of classic cyanine structures.

significant advantages of cyanine dyes is their high molar absorption coefficients and quantum yields, which provide bright and stable fluorescence signals [53]. These dyes are particularly beneficial in live-cell imaging due to their low toxicity and good membrane permeability [54]. In addition, cyanine dyes often have strong photostability, which is essential for long-term imaging experiments where continuous or repeated excitation is necessary [55]. Another notable feature of cyanine dyes is their ability to undergo modifications that enhance their biological relevance. For example, the introduction of functional groups can allow cyanine dyes to target specific biomolecules

or cellular components, enabling selective imaging of proteins, nucleic acids, or cellular structures [56-58]. Moreover, cyanine dyes can be chemically linked to biomolecules, such as antibodies or peptides, to create highly specific probes for targeting particular cells or tissues [59-61].

In recent years, many cyanine (Fig. 1.7) dyes have been developed and widely used in biological imaging due to their strong fluorescence and tunable properties [62-

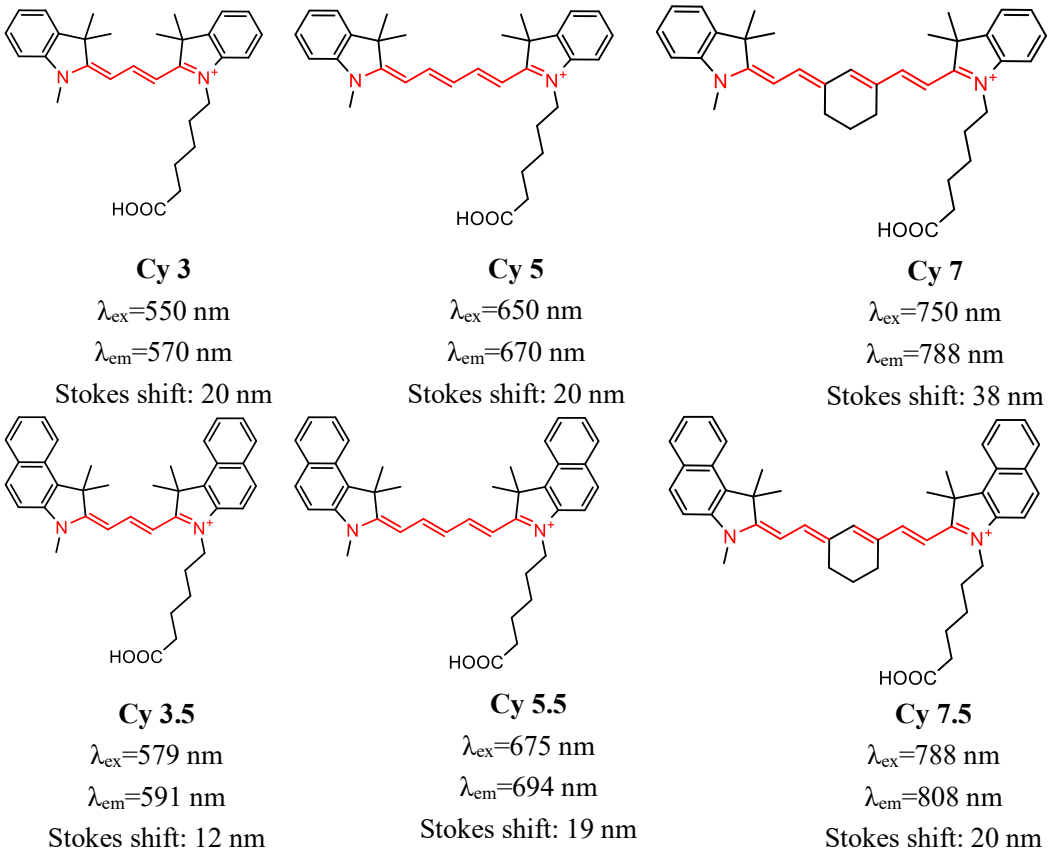


Fig. 1.7 The structures of common cyanine derivatives

64]. While cyanine-based dyes offer many advantages, they also face certain challenges common to most fluorescent probes. One significant issue is the overlap between absorption and emission spectra, known as self-absorption or reabsorption, which can severely limit the sensitivity and accuracy of detection in complex biological systems [65]. This problem becomes particularly prominent in densely labeled samples or when performing multiplexed imaging, where spectral overlap can lead to signal crosstalk and reduced imaging resolution [66]. To address these challenges, fluorescent probes with large Stokes shifts have garnered considerable attention. In particular, designing

probes with large Stokes shifts involves careful molecular engineering to achieve specific electronic transitions. The incorporation of unique functional groups, structural modifications, and advanced donor-acceptor designs has paved the way for the development of probes tailored for challenging imaging applications.

1.4 Fluorescent Probes with Large Stokes Shift

1.4.1 Significance of large Stokes shift

Fluorescent probes with large Stokes shifts have gained considerable attention in fluorescence imaging due to their ability to overcome limitations associated with spectral overlap, autofluorescence, and reabsorption. These probes are essential in achieving clear, high-contrast fluorescence signals, which are critical for biological and

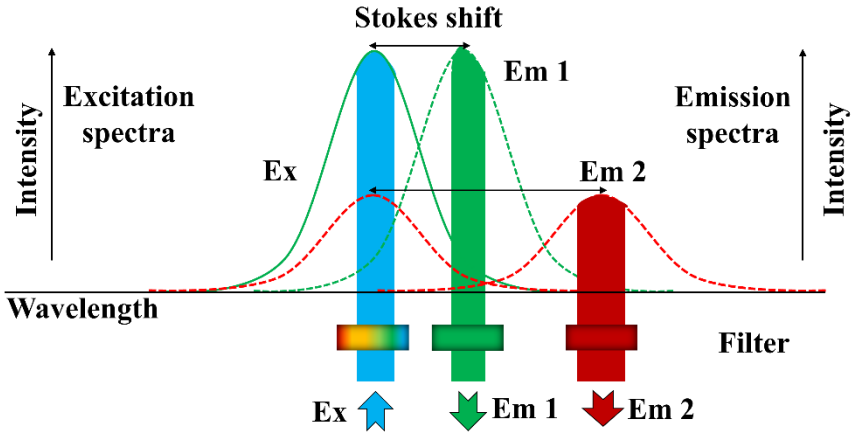


Fig. 1.8 Diagram of the Stokes shift between absorption and emission spectra.

medical applications. The Stokes shift (Fig. 1.8), defined as the energy difference between the absorption and emission maxima of a fluorophore, is a critical factor in determining the effectiveness of fluorescent probes. Large Stokes shifts provide several advantages in fluorescence-based applications. First, they minimize the overlap between excitation and emission spectra, reducing self-quenching and cross-talk. This is particularly important for imaging in complex biological systems, where autofluorescence from cellular components can interfere with signals [67]. Second, large Stokes shift dyes improve the signal-to-noise ratio, enabling more precise and reliable detection of fluorescence signals [68]. Finally, large Stokes shifts facilitate multiplexed imaging by allowing multiple fluorophores to operate in the same system without spectral interference, providing comprehensive insight into complex biological processes [69].

1.4.2 Design strategies for large Stokes shift probes

Designing fluorescent probes with large Stokes shifts requires careful molecular engineering to control their photophysical properties. Several strategies have been developed to achieve this:

POLARIC (Polarity Indicating Chromophore)

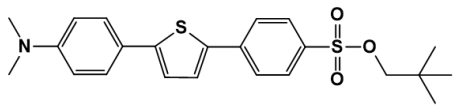
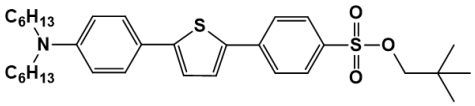
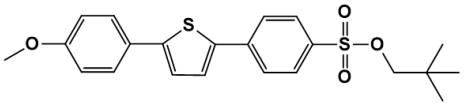
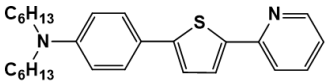
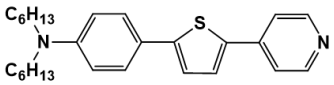
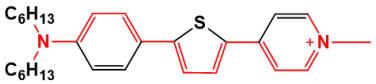
Structure	$\lambda_{abs}/\lambda_{em}$/nm	Stokes shift/nm	$\varepsilon/M^{-1}cm^{-1}$
	394/482	88	27000
	404/479	75	30000
	358/434	76	29000
	387/451	64	32000
	390/456	66	31000
	**470/570**	**100**	33000

Table 1.1 Previous research in Yamada Lab [70].

POLARIC dyes are a class of fluorescent molecules, featuring a donor–π–acceptor (D–π–A) structure that enables strong intramolecular charge transfer (ICT) (Table 1.1). This design results in large Stokes shifts, high photostability, and sensitivity to environmental changes, making them ideal for biological imaging.

By modifying the donor and acceptor groups, POLARIC dyes can be tuned to emit across a broad spectral range, including the near-infrared region. Their fluorescence properties are highly responsive to polarity and viscosity, allowing for applications in membrane dynamics and microenvironment sensing. Additionally, their low cytotoxicity and reduced self-quenching improve imaging performance in live-cell experiments.

With their excellent optical properties and versatility, POLARIC dyes serve as powerful tools for fluorescence imaging, biosensing, and diagnostic applications, enabling the visualization of complex biological processes at the molecular level.

Incorporation of asymmetric vibration structure

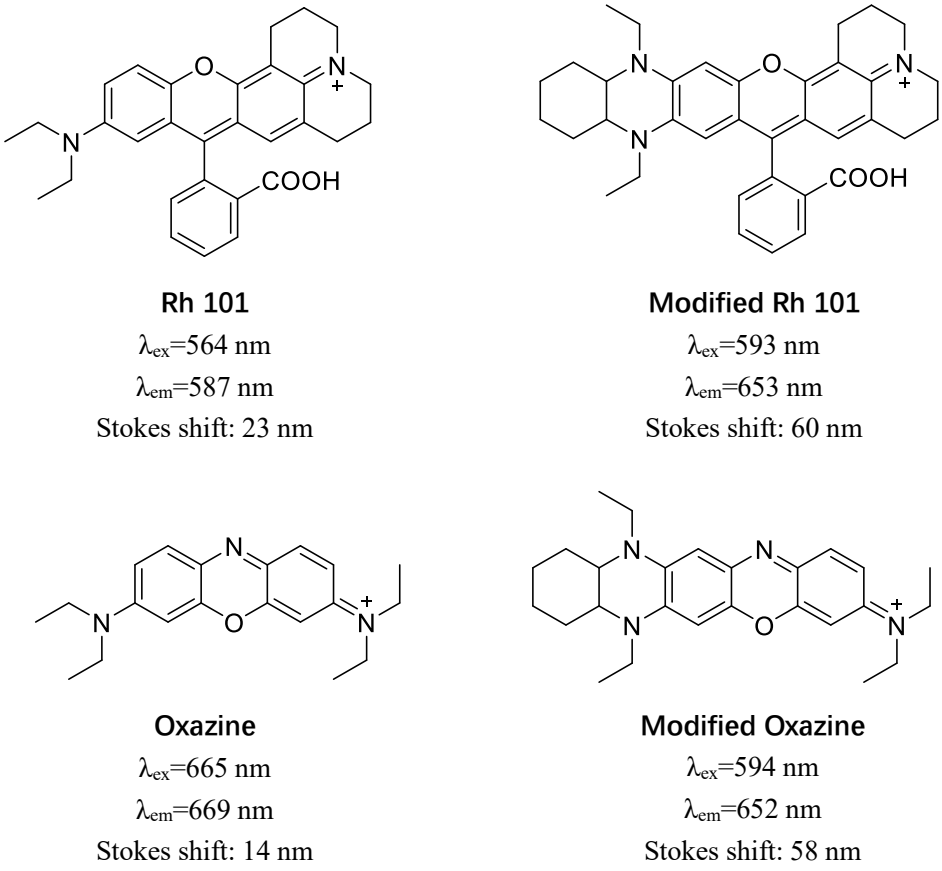
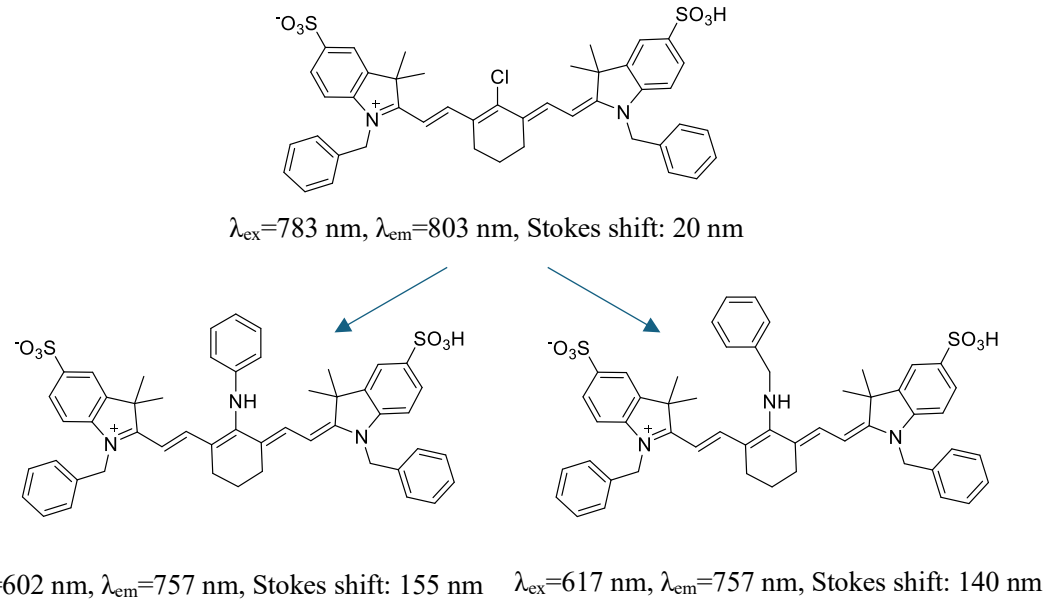


Fig. 1.9 Increasing Stokes shift of fluorophores by incorporation of asymmetric vibronic structures [71,72].

According to the luminescence principles illustrated by the Jabłoński diagram, Stokes shift is associated with vibrational relaxation processes. Generally, the greater the energy dissipation during vibrational relaxation, the larger the resulting Stokes shift of fluorophores. Conventional fluorophores, such as cyanine, squaraine, fluorescein, and rhodamine, typically exhibit highly symmetrical molecular structures and evenly distributed electron densities in their HOMO and LUMO orbitals. This symmetry contributes to their high quantum yields while minimizing the presence of vibrational sub-levels [73,74]. Consequently, disrupting molecular symmetry can enhance

vibrational relaxation, thereby leading to an increased Stokes shift in fluorophores (Fig.1.9).

Insertion of the intermediate N atom



λ_{ex}=783 nm, λ_{em}=803 nm, Stokes shift: 20 nm

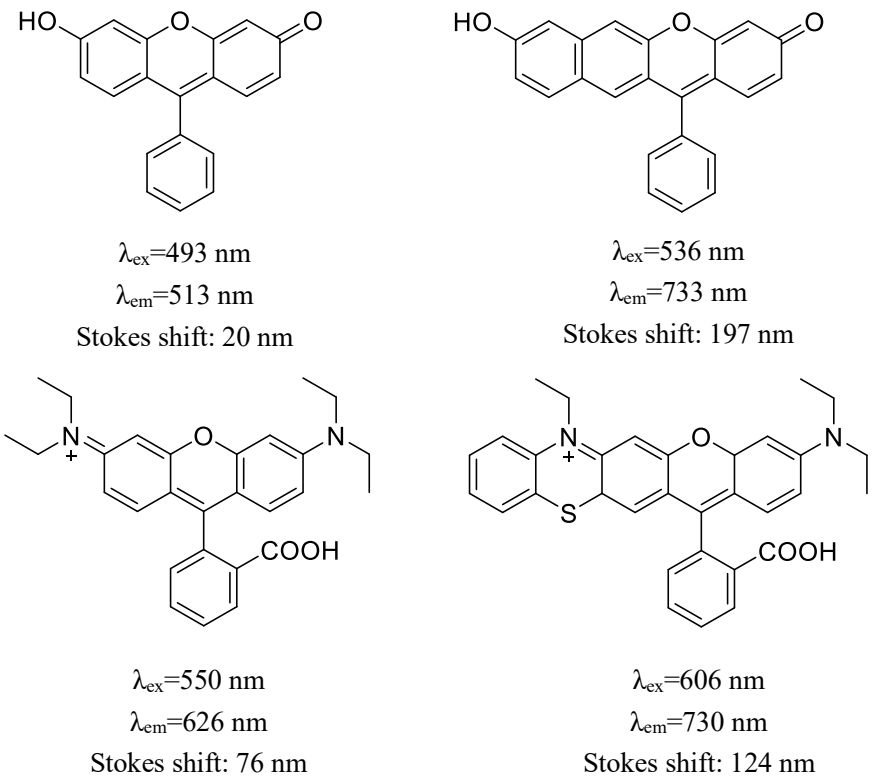
λ_{ex}=602 nm, λ_{em}=757 nm, Stokes shift: 155 nm

λ_{ex}=617 nm, λ_{em}=757 nm, Stokes shift: 140 nm

Fig. 1.10 The insertion of the intermediate N atom to increase Stokes shift [75].

Inserting N atoms into fluorophore structures has proven to be an effective strategy for increasing Stokes shift. For example, Peng and colleagues (Fig. 1.10) introduced alkylamino groups into a symmetrical heptamethine cyanine dye, resulting in derivatives with dramatically enhanced Stokes shifts (up to 155/144 nm compared to the parent dye's 20 nm). This enhancement is attributed to intramolecular charge transfer (ICT), where nitrogen substitution disrupts molecular symmetry in the ground state. Partial symmetry restoration in the excited state leads to significant structural rearrangement during electron relaxation, increasing vibrational relaxation and the Stokes shift [76]. This approach has since been applied to various fluorophore frameworks, such as pyronin and BODIPY dyes, offering a versatile design strategy for large Stokes shift probes [77].

Introducing aromatic/aromatic-heterocyclic ring



λ_{ex}=493 nm
λ_{em}=513 nm
Stokes shift: 20 nm

λ_{ex}=536 nm
λ_{em}=733 nm
Stokes shift: 197 nm

λ_{ex}=550 nm
λ_{em}=626 nm
Stokes shift: 76 nm

λ_{ex}=606 nm
λ_{em}=730 nm
Stokes shift: 124 nm

Fig. 1.11 Introducing aromatic/aromatic-heterocyclic ring to increase Stokes shift [78-81].

Incorporating aromatic or aromatic-heterocyclic rings into one side of symmetrical fluorophores effectively enhances intramolecular charge transfer (ICT), leading to larger Stokes shifts. For instance (Fig. 1.11), Strongin's group developed seminaphthofluorophores by introducing a naphthol structure into xanthene dyes, achieving a Stokes shift of 197 nm compared to 20 nm for the parent dye. Similarly, the Zeng group demonstrated that incorporating aromatic-heterocyclic rings into rhodamine dyes significantly increases Stokes shifts while red-shifting absorption and emission wavelengths. This strategy is also effective in other fluorophore types, such as oxazine [82]. Furthermore, introducing heteroatoms provides additional reactive sites, expanding the potential for developing functional probes for biomarker detection.

Boron Complexation

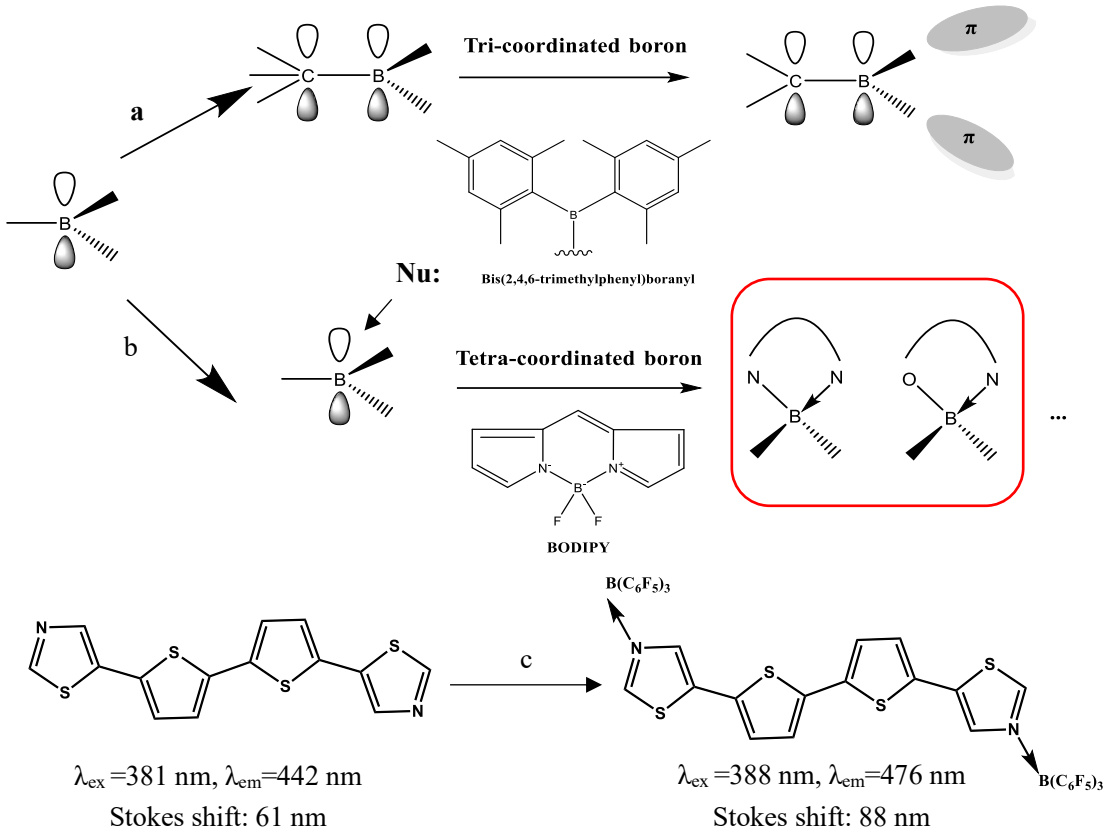


Fig. 1.12 Principles of designing organic boron-containing molecules [83].

Boron complexation is an effective strategy to enhance Stokes shift by leveraging the Lewis acidity of the boron atom's vacant p-orbital. This approach typically involves coordination between the electron-deficient boron center and electron-rich aromatic compounds containing O or N atoms, such as hydroxyquinolines or nitrogen heterocycles (Fig. 1.12, a). The resulting intramolecular Lewis acid-base adducts create rigid π-conjugated structures, which facilitate electron delocalization across the molecule. By modifying the ligands with various substituents, the electronic properties of the boron complexes can be finely tuned, significantly altering their photophysical characteristics before and after coordination. Additionally, boron can be incorporated into the molecular framework by utilizing the electron-deficient nature of trivalent boron centers. Functional molecules with D-π-A or D-A structures are designed by attaching electron-donating groups to the π-conjugated system (Fig 1.12, b, c). To enhance stability and protect the boron's vacant p-orbital from nucleophilic attack,

sterically hindered aromatic groups such as 2,4,6-trimethylphenyl or 2,4,6-triisopropylphenyl are often introduced. This p-π* conjugation imparts strong electron-withdrawing properties to the boron center, enhancing intramolecular charge transfer (ICT) within the molecule. This ICT effect, coupled with the rigid and planar structure, effectively increases the Stokes shift, making boron complexes valuable tools in the development of functional fluorophores.

1.5 Introduction of PET-Based Probes

The concept of fluorescent PET (photoinduced electron transfer) sensors and switches, first proposed over six decades ago, has become a cornerstone in the development of fluorescence-based detection systems [84]. This principle leverages the thermodynamic insights laid out by Weller in the 1960s, who demonstrated the competition between fluorescence emission and PET processes during excited-state deactivation [85]. Later, Marcus's theoretical contributions to PET kinetics provided a deeper understanding of the interplay between these mechanisms, forming a solid theoretical foundation for further exploration [86]. A key feature of PET-based systems is their ability to produce distinct fluorescence signal changes in response to external stimuli, often manifesting as "off–on" or "on–off" transitions [87]. Such properties have not only broadened their applications in chemical sensing and molecular recognition but have also laid the groundwork for innovative approaches in molecular information processing [88]. This binary behavior, driven by analyte-induced modulation of PET, allows for straightforward detection, either visually or with minimal instrumentation [89]. The simplicity and reliability of the PET mechanism have led to its widespread adoption, with significant advancements reported annually [90-93].

In recent years, PET-based fluorescent probes have demonstrated their versatility in a variety of applications, particularly in small-molecule systems designed for selective and sensitive detection [94-98]. These systems operate by comparing the fluorescence behavior in the presence and absence of target analytes, resulting in observable differences that are both qualitative and quantitative. The sustained interest and rapid development in this field underscore the robustness and adaptability of the PET principle [99].

In this dissertation, the discussion on PET-based fluorescent probes will focus on their design strategies, theoretical underpinnings, and applications, particularly in the imaging of biothiols. This approach builds on decades of foundational research while addressing the specific challenges and opportunities in the context of cellular imaging and analyte detection.

1.5.1 Mechanism of PET-Based Probes

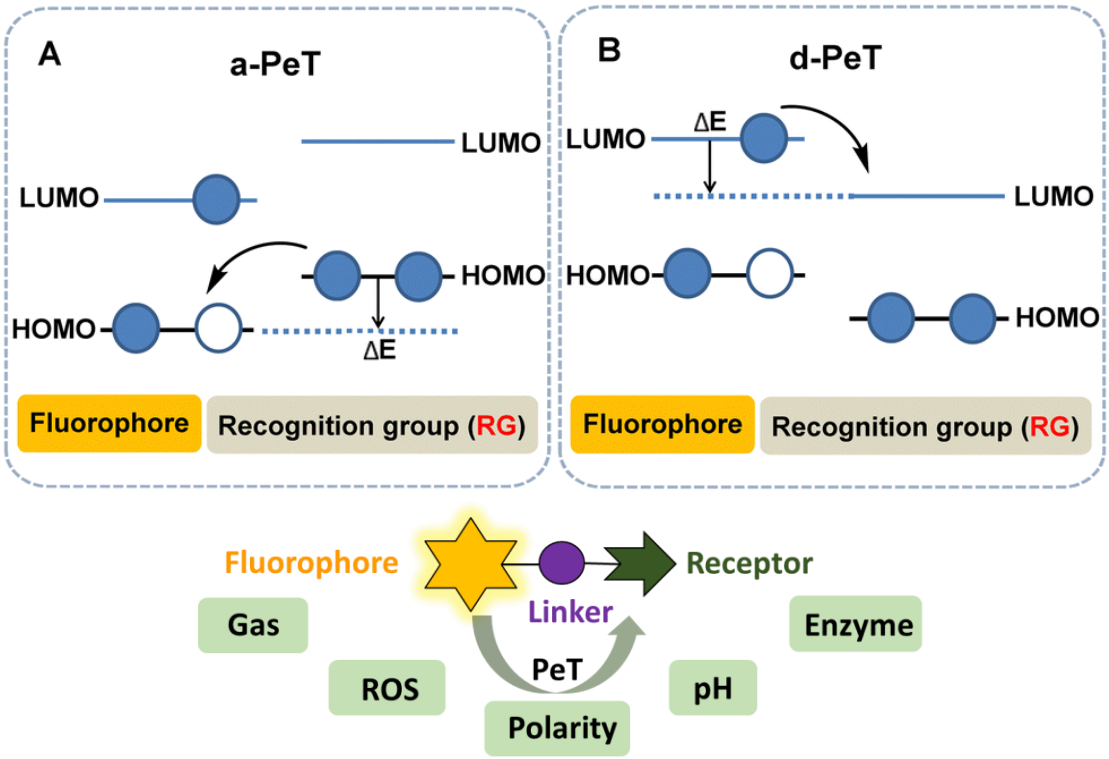


Fig. 1.13 The frontier orbital theory of the PET mechanism [100] and applications.

The mechanism of photoinduced electron transfer (PET) can be divided into two main types, acceptor-PET (a-PET) and donor-PET (d-PET), based on the direction of electron flow between the recognition/activating group and the fluorophore. Both types rely on the relative energy levels of the fluorophore and the recognition/activating group, which determine whether fluorescence is quenched.

a-PET Mechanism

In the a-PET process, the recognition or activating group acts as the donor. Its highest occupied molecular orbital (HOMO) energy level lies between the HOMO and lowest unoccupied molecular orbital (LUMO) energy levels of the fluorophore. When the fluorophore is excited, its "empty" HOMO (or excited state HOMO) becomes energetically favorable for electron transfer from the recognition/activating group's HOMO. This electron transfer prevents the electron in the LUMO of the fluorophore from returning to its ground state, thereby leading to fluorescence quenching (Fig. 1.13A).

In the d-PET process, the recognition/activating group functions as an electron acceptor. Its LUMO energy level is positioned between the HOMO and LUMO of the fluorophore. Upon excitation, an electron in the fluorophore's HOMO transitions to its LUMO, followed by a non-radiative transfer of this excited electron to the vacant LUMO of the recognition/activating group. This transition prevents the fluorophore from emitting fluorescence, resulting in fluorescence quenching (Fig. 1.13B).

Regardless of the type of PET mechanism, the outcome is the same—fluorescence quenching due to efficient electron transfer. The energy level alignment between the fluorophore and the recognition/activating group is critical in designing effective PET probes, enabling selective responses to specific analytes. The PET process is widely exploited in the development of fluorescence-based sensors, where the binding of a target molecule alters the electronic properties of the recognition/activating group, thereby switching fluorescence "on" or "off." This principle forms the foundation of PET probe design and its application in chemical sensing, biological imaging, and environmental monitoring.

1.5.2 Strategy for PET-Based Probes

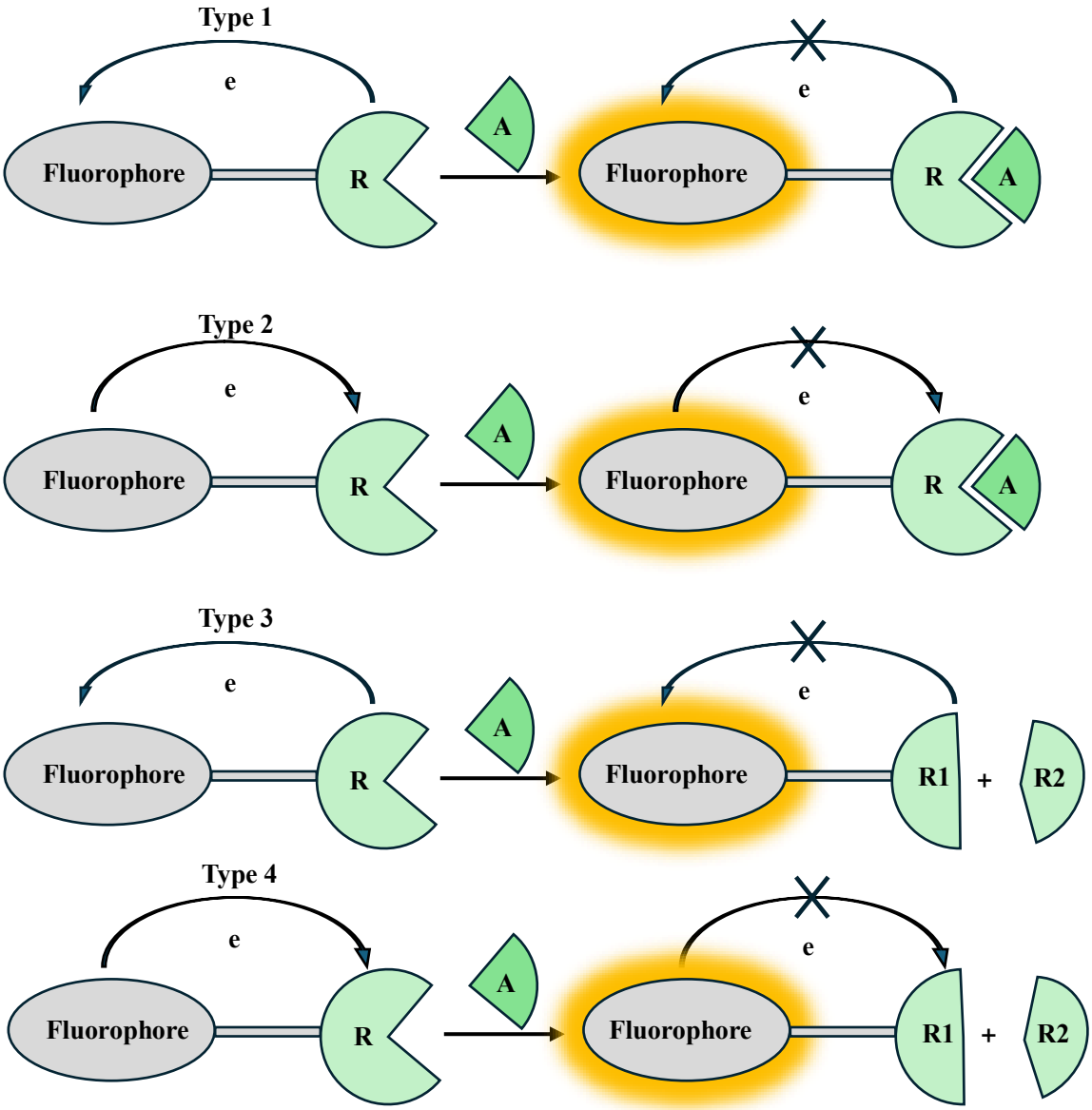


Fig. 1.14 The four design types of PET-based fluorescent probes: **Type 1**: Upon binding to the target, the oxidation potential of the recognition/activating group increases, thereby inhibiting the a-PET process. **Type 2**: Interaction with the target leads to a decrease in the oxidation potential of the recognition/activating group, suppressing the d-PET process. **Type 3**: The recognition/activating group is cleaved after interaction with the analyte, preventing the a-PET mechanism. **Type 4**: Cleavage of the recognition/activating group upon target binding stops the d-PET process.

R represents the recognition group responsible for interacting with the target analyte A, e represents electron.

The oxidation and reduction potentials reflect the ability of a molecule to donate or accept electrons. PET occurs due to electron transfer between the fluorophore and the recognition/activating group. Based on how the recognition process influences the oxidation or reduction potential of the recognition/activating unit, PET-based fluorescent probes can generally be categorized into four types (Fig. 1.14).

Type 1

After binding with the target, the oxidation potential of the recognition/activating group increases, rendering it unable to serve as an effective electron donor. This inhibition prevents the occurrence of a-PeT (Fig. 1.15) [101].

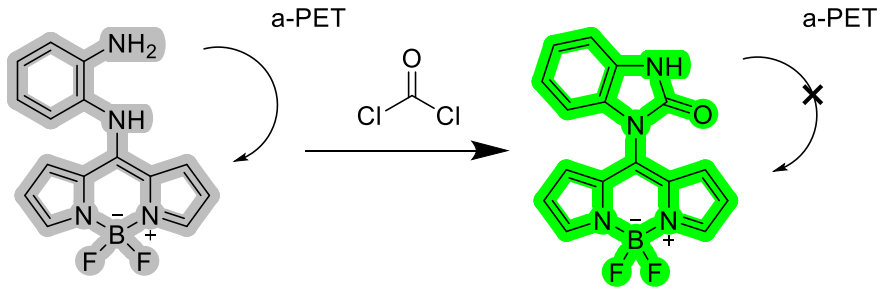


Fig 1.15 Example of **type 1**.

Type 2

If the recognition/activating group's oxidation potential decreases upon target recognition, it becomes incapable of efficiently accepting electrons, thereby suppressing the d-PeT process (Fig. 1.16) [102].

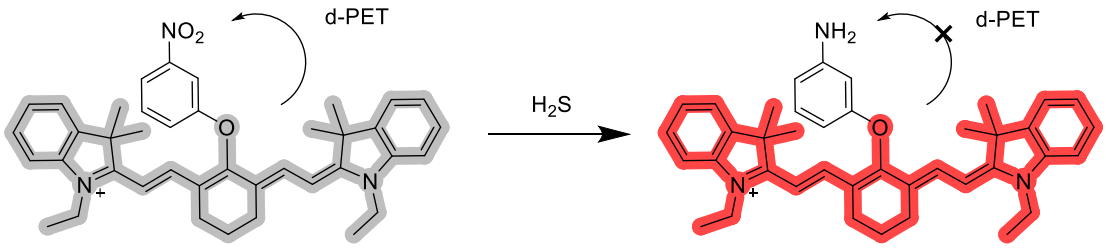


Fig 1.16 Example of **type 2**.

Type 3

In some cases, the recognition/activating group is cleaved by the analyte, disrupting the a-PET process and restoring fluorescence (Fig. 1.17) [103].

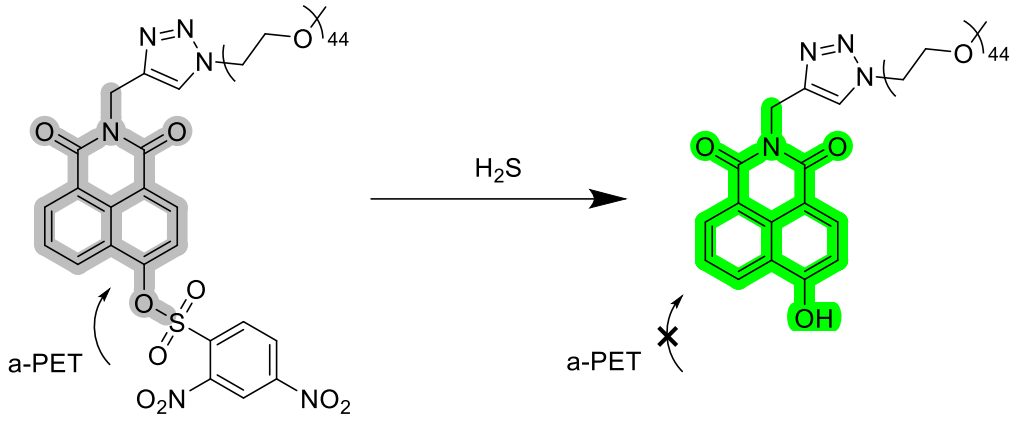


Fig 1.17 Example of **type 3**.

Type 4

Similarly, cleavage of the recognition/activating group by the target can also block the d-PET mechanism, enabling fluorescence activation (Fig. 1.18) [104]. In recent years,

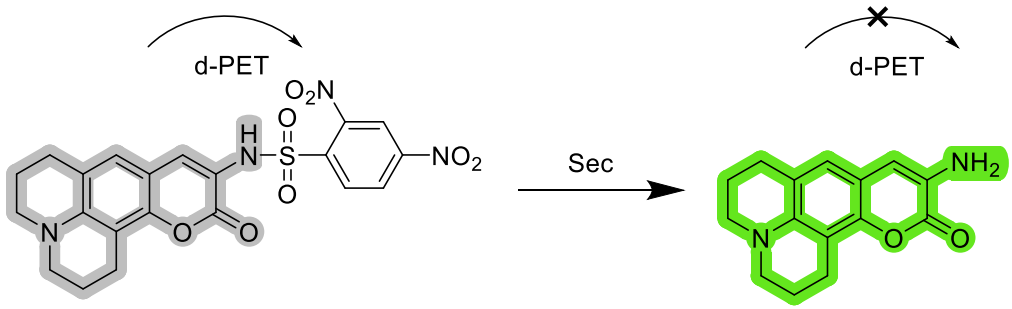


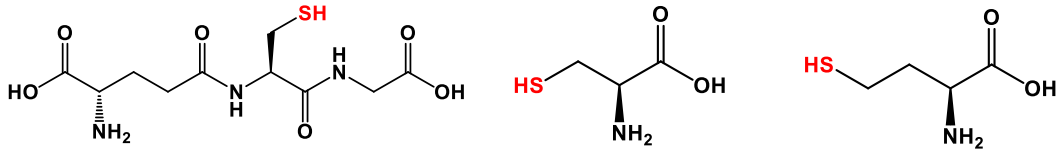
Fig 1.18 Example of **type 4**.

PET-based fluorescent probes, designed using the aforementioned strategies, have found extensive applications in detecting and imaging various intracellular processes. These include analyzing the cellular microenvironment, monitoring reactive small molecules such as reactive oxygen species, gaseous molecules, and biothiols, as well as detecting reactive biological macromolecules [105-113]. Additionally, their application has expanded to the diagnosis and treatment of diseases, particularly cancer. The flexibility of these probes lies in their ability to couple a single fluorophore with

either electron-rich or electron-deficient recognition units, enabling roles as electron donors or acceptors. This adaptability allows the same fluorophore to facilitate both “off–on” and “on–off” detection modes, thereby enabling the development of a wide variety of PET-based probes from a relatively small pool of fluorophores.

1.6 Importance of Biothiols Sensing

Biothiols (Fig. 1.19), such as glutathione (GSH), cysteine (Cys), and homocysteine (Hcy), are critical molecules in maintaining cellular redox balance and regulating various biological processes [114]. These small sulfur-containing compounds play key roles in protecting cells from oxidative stress, detoxifying harmful substances, and supporting enzyme function [115]. Given their importance, dysregulation of biothiols is associated with a range of diseases, including cancer, neurodegenerative disorders, and cardiovascular diseases [116]. As such, detecting biothiols in live cells is vital for understanding cellular homeostasis and the pathological mechanisms of disease.



Glutathione **Cysteine** **Homocysteine**

Fig. 1.19 The structures of biothiols.

Among biothiols, glutathione (1-10 mM) is the most abundant and essential, acting as a major antioxidant that defends against reactive oxygen species (ROS). It plays a central role in the cellular redox environment, con tributing to detoxification processes and the regulation of cell signaling pathways [117]. An imbalance in GSH levels is often linked to oxidative stress, which can lead to cellular damage and contribute to the progression of diseases like cancer and Alzheimer's disease [118]. Therefore, the ability to monitor GSH levels in real-time within living cells can provide insights into the cellular response to oxidative stress and disease progression. Cysteine (30-200 μM), another important biothiol, serves as a precursor to GSH and is involved in protein synthesis, enzyme activity regulation, and cell signaling [119]. Like GSH, cysteine is implicated in redox homeostasis and its altered levels are associated with conditions such as metabolic disorders, immune deficiencies, and liver diseases [120]. Furthermore, homocysteine (12-15 μM) is known to be involved in cardiovascular health, and elevated levels of this biothiol have been linked to a higher risk of heart

disease and stroke [121].

Fluorescent probes designed for biothiol detection have become indispensable tools for studying these molecules in live-cell environments. They allow for selective, real-time imaging of biothiols, providing researchers with critical information about redox processes, thiol-based signaling pathways, and the onset of oxidative stress-related diseases [122]. By targeting specific biothiols, these probes enable a deeper understanding of the role of these molecules in maintaining cellular health and their involvement in pathological conditions [123]. In the context of disease, biothiol detection is particularly valuable for cancer research. Tumor cells often exhibit altered redox states, including elevated GSH levels, which help them survive in oxidative environments and resist chemotherapy [124]. Detecting and understanding these shifts in biothiol concentrations can help identify potential therapeutic targets and improve strategies for treating cancer and other redox-related diseases [125].

In summary, biothiol detection in live cells is critical for studying cellular redox biology and understanding the mechanisms of diseases linked to oxidative stress. Fluorescent probes designed for this purpose offer a powerful means of investigating how biothiols contribute to both normal cellular function and the development of pathological conditions.

1.7 Objectives and Outline

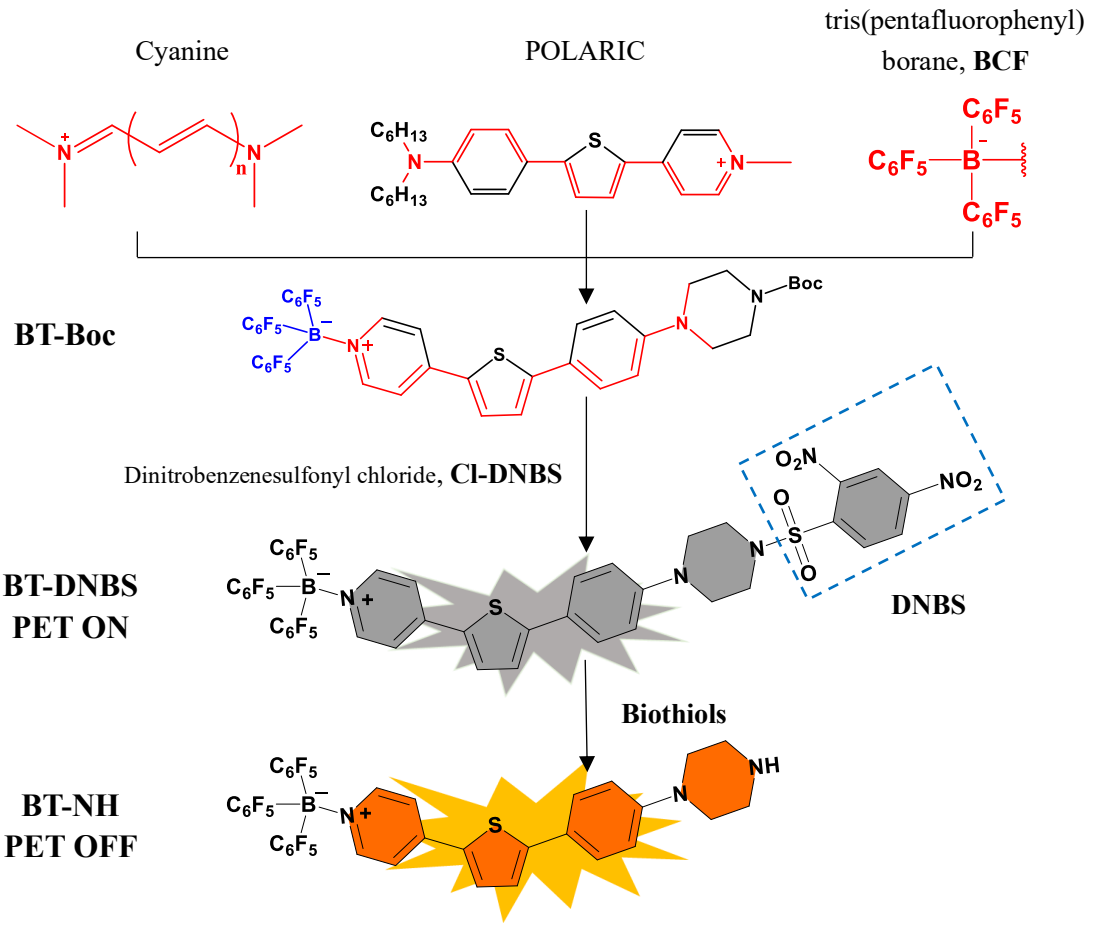


Fig. 1.20 Structures of **BT-Boc** (4-(5-(4-(4-(*tert*-butoxycarbonyl)piperazin-1-yl)phenyl)thiophen-2-yl)-1-(tris(pentafluorophenyl)-λ^4-boraneyl)pyridin-1-ium), **BT-DNBS** (4-(5-(4-(4-((2,4-dinitro phenyl)sulfonyl)piperazin-1-yl)phenyl)thiophen-2-yl)-1-(tris(pentarfluorophenyl)-λ^4-boraneyl) pyridine-1-ium) and **BT-NH** (4-(5-(4-(piperazin-1-yl)phenyl)thiophen-2-yl)-1-(tris(pentafluorophenyl)-λ^4-boraneyl)pyridin-1-ium).

1.7.1 Objectives

The design of the probes was inspired by the need to address the limitations of existing biothiol-targeting fluorescent probes, such as small Stokes shift, low photostability, and limited specificity. The probe **BT-Boc** features a D-π-A framework (Fig. 1.20) based on cyanine dyes, with pyridinium as the electron-withdrawing group and piperazine as the electron-donating group. POLARIC^{TM} was selected as the structural backbone due to their excellent photophysical properties, including high molar absorptivity, efficient

fluorescence quantum yield, and tunable optical characteristics. Additionally, the pyridinium moiety introduced by BCF [tris(pentafluorophenyl) borane, $B(C_6F_5)_3$)] enhances electron deficiency. DNBS serves as a commonly used fluorescence quenching moiety and reaction site for biothiols.

1. To develop a fluorescent probe with an ultra-large Stokes shift.
2. To develop a PET-based turn-on fluorescent probe for detecting intracellular biothiols.
3. To demonstrate the probe's effectiveness in detecting intracellular biothiols and evaluate its imaging performance under live-cell conditions.

1.7.2 Outline

This dissertation explores the development of a PET-based fluorescent probe with a large Stokes shift for biothiol detection and live-cell imaging. **Chapter 1** introduces luminescence, fluorescence microscopy, and fluorescent probes, with a focus on cyanine-based dyes and strategies for achieving large Stokes shifts. The significance and design principles of PET-based probes are discussed, along with the importance of biothiol sensing. **Chapter 2** details the synthesis and characterization of the probe, including its photophysical properties. Also, it examines the fluorescence activation mechanism of BT-DNBS upon reaction with biothiols, assessing its selectivity and sensitivity, etc. **Chapter 3** presents live-cell imaging experiments, optimizing staining conditions and confirming intracellular biothiol detection. Finally, **Chapter 4** summarizes the findings and discusses future applications in bioimaging and molecular sensing.

References

1. Choy G, Choyke P, Libutti SK. Current Advances in Molecular Imaging: Noninvasive in Vivo Bioluminescent and Fluorescent Optical Imaging in Cancer Research. *Molecular Imaging*. **2003**, 2(4). DOI: 10.1162/15353500200303142.
2. Ntziachristos V. Fluorescence molecular imaging. *Annu. Rev. Biomed. Eng.*, **2006**, 8(1): 1-33. DOI: 0.1146/annurev.bioeng.8.061505.095831
3. Gao P, Pan W, Li N, et al. Fluorescent probes for organelle-targeted bioactive species imaging. *Chemical science,* **2019**, 10(24): 6035-6071. DOI: 10.1039/C9SC01652J
4. Gonçalves M S T. Fluorescent labeling of biomolecules with organic probes. *Chemical reviews*, **2009**, 109(1): 190-212. DOI: 10.1021/cr0783840
5. Massoud T F, Gambhir S S. Molecular imaging in living subjects: seeing fundamental biological processes in a new light. *Genes & development*, **2003**, 17(5): 545-580. DOI: 10.1101/gad.1047403.
6. Carter K P, Young A M, Palmer A E. Fluorescent sensors for measuring metal ions in living systems. *Chemical reviews*, **2014**, 114(8): 4564-4601. DOI: 10.1021/cr400546e.
7. Walter M, Chaban C, Schütze K, et al. Visualization of protein interactions in living plant cells using bimolecular fluorescence complementation. *The Plant Journal*, **2004**, 40(3): 428-438.DOI: 10.1111/j.1365-313X.2004.02219.x.
8. Yao J, Yang M, Duan Y. Chemistry, biology, and medicine of fluorescent nanomaterials and related systems: new insights into biosensing, bioimaging, genomics, diagnostics, and therapy. *Chemical reviews*, **2014**, 114(12): 6130-6178. DOI: 10.1021/cr200359p.
9. Forman H J, Fukuto J M, Torres M. Redox signaling: thiol chemistry defines which reactive oxygen and nitrogen species can act as second messengers. *American Journal of Physiology-Cell Physiology*, **2004**, 287(2): C246-C256. DOI: 10.1152/ajpcell. 00516.2003.
10. Deneke S M. Thiol-based antioxidants. *Current topics in cellular regulation*, **2001**,

36: 151-180. DOI: 10.1016/S0070-2137(01)80007-8.

11. Louie A. Multimodality imaging probes: design and challenges. *Chemical reviews*, **2010**, 110(5): 3146-3195. DOI: 10.1021/cr9003538.
12. Jung J, Lin C H, Yoon Y J, et al. Crafting Core/Graded Shell–Shell Quantum Dots with Suppressed Re-absorption and Tunable Stokes Shift as High Optical Gain Materials. *Angewandte Chemie,* **2016**, 128(16): 5155-5159. DOI: 10.1002/anie. 201601198.
13. Ding F, Zhan Y, Lu X, et al. Recent advances in near-infrared II fluorophores for multifunctional biomedical imaging. *Chemical science*, **2018**, 9(19): 4370-4380. DOI: 10.1039/C8SC01153B.
14. Ebenezar J, Pu Y, Liu C H, et al. Diagnostic potential of stokes shift spectroscopy of breast and prostate tissues—a preliminary pilot study. *Technology in cancer research & treatment*, **2011**, 10(2): 153-161. DOI: 10.7785/tcrt.2012.500190.
15. Sednev M V, Belov V N, Hell S W. Fluorescent dyes with large Stokes shifts for super-resolution optical microscopy of biological objects: a review. *Methods and applications in fluorescence*, **2015,** 3(4): 042004. DOI: 10.1088/2050-6120/3/4/042004.
16. Walton A J. Triboluminescence. *Advances in Physics*, **1977**, 26(6): 887-948. DOI: 10.1080/00018737700101483.
17. Shinde K N, Dhoble S J, Swart H C, et al. Basic mechanisms of photoluminescence. *Phosphate Phosphors for Solid-State Lighting*, **2012**: 41-59. DOI：10.1007/978-3-642-34312-4_2.
18. Dodeigne C, Thunus L, Lejeune R. Chemiluminescence as diagnostic tool. A review. *Talanta*, **2000**, 51(3): 415-439. DOI: 10.1016/S0039-9140(99)00294-5.
19. Mitschke U, Bäuerle P. The electroluminescence of organic materials. *Journal of Materials Chemistry*, **2000**, 10(7): 1471-1507. DOI: 10.1039/A908713C.
20. Walton A J. Triboluminescence. *Advances in Physics*, **1977**, 26(6): 887-948. DOI: 10.1080/00018737700101483.
21. Götze J, Plötze M, Habermann D. Origin, spectral characteristics and practical

applications of the cathodoluminescence (CL) of quartz–a review. *Mineralogy and petrology*, **2001**, 71: 225-250. DOI: 10.1007/s007100170040.

22. Lichtman J W, Conchello J A. Fluorescence microscopy. *Nature methods*, **2005**, 2(12): 910-919. DOI: 10.1038/nmeth817.
23. Sanderson M J, Smith I, Parker I, et al. Fluorescence microscopy. *Cold Spring Harbor Protocols*, **2014**, 2014(10). DOI:10.1101/pdb.top071795.
24. Zhang J, Campbell R E, Ting A Y, et al. Creating new fluorescent probes for cell biology. *Nature reviews Molecular cell biology*, **2002**, 3(12): 906-918. DOI: 10.1038/nrm976.
25. Kobayashi H, Ogawa M, Alford R, et al. New strategies for fluorescent probe design in medical diagnostic imaging. *Chemical reviews*, **2010**, 110(5): 2620-2640. DOI: 10.1021/cr900263j.
26. Park S H, Kwon N, Lee J H, et al. Synthetic ratiometric fluorescent probes for detection of ions. *Chemical Society Reviews*, **2020**, 49(1): 143-179. DOI: 10.1039/C9CS00243J.
27. Giepmans B N G, Adams S R, Ellisman M H, et al. The fluorescent toolbox for assessing protein location and function. *Science*, **2006**, 312(5771): 217-224. DOI: 10.1126/science.1124618.
28. HeeáLee M, SeungáKim J. Small molecule-based ratiometric fluorescence probes for cations, anions, and biomolecules. *Chemical Society Reviews*, **2015**, 44(13): 4185-4191. DOI: 10.1039/C4CS00280F.
29. Sjöback R, Nygren J, Kubista M. Absorption and fluorescence properties of fluorescein. *Spectrochimica Acta Part A: Molecular and Biomolecular Spectroscopy*, 1**995**, 51(6): L7-L21. DOI: 10.1016/0584-8539(95)01421-P.
30. Beija M, Afonso C A M, Martinho J M G. Synthesis and applications of Rhodamine derivatives as fluorescent probes. *Chemical Society Reviews*, **2009**, 38(8): 2410-2433. DOI: 10.1039/B901612K.
31. Gao M, Li Y, Chen X, et al. Aggregation-induced emission probe for light-up and in situ detection of calcium ions at high concentration. *ACS applied materials &*

interfaces, **2018**, 10(17): 14410-14417. DOI: 10.1021/acsami.8b00952.

32. Chinen A B, Guan C M, Ferrer J R, et al. Nanoparticle probes for the detection of cancer biomarkers, cells, and tissues by fluorescence. *Chemical reviews*, **2015**, 115(19): 10530-10574. DOI: 10.1021/acs.chemrev.5b00321.
33. Eastmond D A, Schuler M, Rupa D S. Advantages and limitations of using fluorescence in situ hybridization for the detection of aneuploidy in interphase human cells. *Mutation Research Letters*, **1995**, 348(4): 153-162. DOI: 10.1016/0165-7992(95)90003-9.
34. Yao J, Yang M, Duan Y. Chemistry, biology, and medicine of fluorescent nanomaterials and related systems: new insights into biosensing, bioimaging, genomics, diagnostics, and therapy. *Chemical reviews*, **2014**, 114(12): 6130-6178. DOI: 10.1021/cr200359p.
35. Juzeniene A, Peng Q, Moan J. Milestones in the development of photodynamic therapy and fluorescence diagnosis. *Photochemical & Photobiological Sciences*, **2007**, 6(12): 1234-1245. DOI: 10.1039/B705461K.
36. Van Hung N, Sy D N, Anthony R M, et al. Fluorescence microscopy for tuberculosis diagnosis. *The Lancet infectious diseases*, **2007**, 7(4): 238-239. DOI: 10.1016/S1473-3099(07)70059-2.
37. Han J, Burgess K. Fluorescent indicators for intracellular pH. *Chemical reviews*, **2010**, 110(5): 2709-2728. DOI: 10.1021/cr900249z.
38. Moradi F, Ismail A M. Responses of photosynthesis, chlorophyll fluorescence and ROS-scavenging systems to salt stress during seedling and reproductive stages in rice. *Annals of botany*, **2007**, 99(6): 1161-1173. DOI: 10.1093/aob/mcm052.
39. Hanson G T, Aggeler R, Oglesbee D, et al. Investigating mitochondrial redox potential with redox-sensitive green fluorescent protein indicators. *Journal of Biological Chemistry*, **2004**, 279(13): 13044-13053. DOI: 10.1074/jbc.M312846200.
40. Kobayashi H, Choyke P L. Target-cancer-cell-specific activatable fluorescence imaging probes: rational design and in vivo applications. *Accounts of chemical*

research, **2011**, 44(2): 83-90. DOI: 10.1021/ar1000633.

41. Hama H, Kurokawa H, Kawano H, et al. Sca le: a chemical approach for fluorescence imaging and reconstruction of transparent mouse brain. *Nature neuroscience*, **2011**, 14(11): 1481-1488. DOI: 10.1038/nn.2928.
42. Lo M C, Aulabaugh A, Jin G, et al. Evaluation of fluorescence-based thermal shift assays for hit identification in drug discovery. *Analytical biochemistry*, **2004**, 332(1): 153-159. DOI: 10.1016/j.ab.2004.04.031.
43. Fujimura H, Dekura E, Kurabe M, et al. Cell-based fluorescence assay for evaluation of new-drugs potential for phospholipidosis in an early stage of drug development. *Experimental and Toxicologic Pathology*, **2007**, 58(6): 375-382. DOI: 10.1016/j.etp.2007.01.004.
44. Seo J, Sim Y, Kim J, et al. PICASSO allows ultra-multiplexed fluorescence imaging of spatially overlapping proteins without reference spectra measurements. *Nature Communications*, **2022**, 13(1): 2475. DOI: 10.1038/s41467-022-30168-z.
45. Luo S, Zhang E, Su Y, et al. A review of NIR dyes in cancer targeting and imaging. *Biomaterials*, **2011**, 32(29): 7127-7138. DOI: 10.1016/j.biomaterials.2011.06.024.
46. Escobedo J O, Rusin O, Lim S, et al. NIR dyes for bioimaging applications. *Current opinion in chemical biology*, **2010**, 14(1): 64-70. DOI: 10.1016/j.cbpa.2009.10.022.
47. Yang L, Su Y, Sha Z, et al. A red-emitting fluorescent probe for hydrogen sulfide in living cells with a large Stokes shift. *Organic & Biomolecular Chemistry*, **2018**, 16(7): 1150-1156. DOI:10.1039/C7OB02641B.
48. Shindy H A. Fundamentals in the chemistry of cyanine dyes: A review. *Dyes and Pigments*, **2017**, 145: 505-513. DOI: 10.1016/j.dyepig.2017.06.029.
49. Williams C G. XXVI. Researches on Chinoline and its Homologues. *Earth and Environmental Science Transactions of The Royal Society of Edinburgh*, **1857**, 21(3): 377-401. DOI: 10.1017/S0080456800032208.
50. Sun W, Guo S, Hu C, et al. Recent development of chemosensors based on cyanine platforms. *Chemical reviews*, **2016**, 116(14): 7768-7817. DOI: 10.1021/acs.chemrev.6b00001.

51. Gorka A P, Nani R R, Schnermann M J. Harnessing cyanine reactivity for optical imaging and drug delivery. *Accounts of chemical research*, **2018**, 51(12): 3226-3235. DOI: 10.1021/acs.accounts.8b00384.
52. Sun C, Li B, Zhao M, et al. J-aggregates of cyanine dye for NIR-II in vivo dynamic vascular imaging beyond 1500 nm. *Journal of the American Chemical Society*, **2019**, 141(49): 19221-19225. DOI: 0.1021/jacs.9b10043.
53. Lin Y, Weissleder R, Tung C H. Novel near-infrared cyanine fluorochromes: synthesis, properties, and bioconjugation. *Bioconjugate chemistry*, **2002**, 13(3): 605-610. DOI: 10.1021/bc0155723.
54. Zhang S, Fan J, Li Z, et al. A bright red fluorescent cyanine dye for live-cell nucleic acid imaging, with high photostability and a large Stokes shift. *Journal of Materials Chemistry B*, **2014**, 2(18): 2688-2693. DOI: 10.1039/C3TB21844A.
55. Altman R B, Zheng Q, Zhou Z, et al. Enhanced photostability of cyanine fluorophores across the visible spectrum. *Nature methods*, **2012**, 9(5): 428-429. DOI: 10.1038/nmeth.1988.
56. Fang F, Zheng H, Li L, et al. Determination of nucleic acids with a near infrared cyanine dye using resonance light scattering technique. *Spectrochimica Acta Part A: Molecular and Biomolecular Spectroscopy*, **2006**, 64(3): 698-702. DOI: 10.1016/j.saa.2005.07.071.
57. Lin C M, Usama S M, Burgess K. Site-specific labeling of proteins with near-ir heptamethine cyanine dyes. *Molecules*, **2018**, 23(11): 2900. DOI: 10.3390/molecules23112900.
58. Zheng M L, Fujita K, Chen W Q, et al. Comparison of staining selectivity for subcellular structures by carbazole-based cyanine probes in nonlinear optical microscopy. *ChemBioChem*, **2011**, 12(1): 52-55. DOI: 10.1002/cbic.201000593.
59. Ballou B, Fisher G W, Waggoner A S, et al. Tumor labeling in vivo using cyanine-conjugated monoclonal antibodies. *Cancer Immunology, Immunotherapy*, **1995**, 41: 257-263. DOI: 10.1007/BF01517001.
60. Berezin M Y, Guo K, Akers W, et al. Rational approach to select small peptide

molecular probes labeled with fluorescent cyanine dyes for in vivo optical imaging. *Biochemistry*, **2011**, 50(13): 2691-2700. DOI: 10.1021/bi2000966.

61. Yin J, Kwon Y, Kim D, et al. Cyanine-based fluorescent probe for highly selective detection of glutathione in cell cultures and live mouse tissues. *Journal of the American chemical society*, **2014**, 136(14): 5351-5358. DOI: 10.1021/ja412628z.
62. Mujumdar R B, Ernst L A, Mujumdar S R, et al. Cyanine dye labeling reagents: sulfoindocyanine succinimidyl esters. *Bioconjugate chemistry*, **1993**, 4(2): 105-111. DOI: 10.1021/bc00020a001.
63. Pauli J, Licha K, Berkemeyer J, et al. New fluorescent labels with tunable hydrophilicity for the rational design of bright optical probes for molecular imaging. *Bioconjugate chemistry*, **2013**, 24(7): 1174-1185. DOI: 10.1021/bc4000349.
64. Gruber H J, Hahn C D, Kada G, et al. Anomalous fluorescence enhancement of Cy3 and Cy3. 5 versus anomalous fluorescence loss of Cy5 and Cy7 upon covalent linking to IgG and noncovalent binding to avidin. *Bioconjugate chemistry*, **2000**, 11(5): 696-704. DOI: 10.1021/bc000015m.
65. Zhou R, Lu X, Yang Q, et al. Nanocrystals for large Stokes shift-based optosensing. *Chinese Chemical Letters*, **2019**, 30(10): 1843-1848. DOI: 10.1016/j.cclet.2019.07.062.
66. Dixon A R, Bathany C, Tsuei M, et al. Recent developments in multiplexing techniques for immunohistochemistry. *Expert review of molecular diagnostics*, **2015**, 15(9): 1171-1186. DOI:10.1586/14737159.2015.1069182.
67. García-Plazaola J I, Fernández-Marín B, Duke S O, et al. Autofluorescence: biological functions and technical applications. *Plant Science*, **2015**, 236: 136-145. DOI: 10.1016/j.plantsci.2015.03.010.
68. Yue Y, Zhao T, Xu Z, et al. Enlarging the Stokes Shift by Weakening the π-Conjugation of Cyanines for High Signal-to-Noise Ratiometric Imaging. *Advanced Science*, **2023**, 10(3): 2205080. DOI: 10.1002/advs.202205080.
69. Wang Y W, Reder N P, Kang S, et al. Multiplexed optical imaging of tumor-directed nanoparticles: a review of imaging systems and approaches. *Nanotheranostics*,

2017, 1(4): 369. DOI: 10.7150/ntno.21136.

70. Son S H, Yamagishi Y, Tani M, et al. Spectral shifts of the environment-sensitive fluorophore POLARIC™ in heterogeneous interfaces. *Chemistry Letters*, **2011**, 40(9): 989-991. DOI: 10.1246/cl.2011.989.
71. Chen W, Xu S, Day J J, et al. A general strategy for development of near-infrared fluorescent probes for bioimaging. *Angewandte Chemie*, **2017**, 129(52): 16838-16842. DOI: 10.1002/ange.201710688.
72. Ren T B, Xu W, Zhang W, et al. A general method to increase stokes shift by introducing alternating vibronic structures. *Journal of the American Chemical Society,* **2018**, 140(24): 7716-7722. DOI: 10.1021/jacs.8b04404.
73. Koide Y, Urano Y, Hanaoka K, et al. Development of an Si-rhodamine-based far-red to near-infrared fluorescence probe selective for hypochlorous acid and its applications for biological imaging. *Journal of the American Chemical Society*, **2011**, 133(15): 5680-5682. DOI: 10.1021/ja111470n.
74. Koide Y, Urano Y, Hanaoka K, et al. Development of NIR fluorescent dyes based on Si–rhodamine for in vivo imaging. *Journal of the American Chemical Society*, **2012**, 134(11): 5029-5031. DOI: 10.1021/ja210375e.
75. Peng X, Song F, Lu E, et al. Heptamethine cyanine dyes with a large stokes shift and strong fluorescence: a paradigm for excited-state intramolecular charge transfer. *Journal of the American Chemical Society*, **2005**, 127(12): 4170-4171. DOI: 10.1021/ja043413z.
76. Sissa C, Painelli A, Terenziani F, et al. About the origin of the large Stokes shift in aminoalkyl substituted heptamethine cyanine dyes. *Physical Chemistry Chemical Physics*, **2020**, 22(1): 129-135. DOI: 10.1039/c9cp05473a.
77. Wu L, Burgess K. Fluorescent amino-and thiopyronin dyes. *Organic Letters*, **2008**, 10(9): 1779-1782. DOI: 10.1021/ol800526s.
78. Yang Y, Lowry M, Xu X, et al. Seminaphthofluorones are a family of water-soluble, low molecular weight, NIR-emitting fluorophores. P*roceedings of the National Academy of Sciences*, **2008**, 105(26): 8829-8834. DOI: 10.1073/pnas.0710341105.

79. Urano Y, Kamiya M, Kanda K, et al. Evolution of fluorescein as a platform for finely tunable fluorescence probes. *Journal of the American Chemical Society*, **2005**, 127(13): 4888-4894. DOI: 10.1021/ja043919h.

80. Jiang G, Ren T B, D'Este E, et al. A synergistic strategy to develop photostable and bright dyes with long Stokes shift for nanoscopy. *Nature Communications*, **2022**, 13(1): 2264. DOI: 10.1038/s41467-022-29547-3.

81. Liu C, Jiao X, Wang Q, et al. A unique rectilinearly π-extended rhodamine dye with large Stokes shift and near-infrared fluorescence for bioimaging. *Chemical Communications*, **2017**, 53(77): 10727-10730. DOI: 10.1039/C7CC06220F.

82. Li W, Yin S, Shen Y, et al. Molecular engineering of pH-responsive NIR oxazine assemblies for evoking tumor ferroptosis via triggering lysosomal dysfunction. *Journal of the American Chemical Society*, **2023**, 145(6): 3736-3747. DOI: 10.1021/jacs.2c13222.

83. Huang Z, Wang S, Dewhurst R D, et al. Boron: its role in energy-related processes and applications. *Angewandte Chemie International Edition*, **2020**, 59(23): 8800-8816. DOI: 10.1002/anie.201911108.

84. de Silva A P, Rupasinghe R A D D. A new class of fluorescent pH indicators based on photo-induced electron transfer. *Journal of the Chemical Society*, *Chemical Communications*, **1985** (23): 1669-1670. DOI: 10.1039/C39850001669.

85. Weller A. Electron-transfer and complex formation in the excited state. *Pure and Applied Chemistry*, **1968**, 16(1): 115-124. DOI: 10.1351/pac196816010115.

86. Marcus R A. On the theory of oxidation-reduction reactions involving electron transfer. I. *The Journal of chemical physics*, **1956**, 24(5): 966-978. DOI: 10.1063/1.1742723.

87. De Silva A P, Gunaratne H Q N, Gunnlaugsson T, et al. Signaling recognition events with fluorescent sensors and switches. *Chemical reviews*, **1997**, 97(5): 1515-1566. DOI: 10.1021/cr960386p.

88. de Silva A P, Uchiyama S. Molecular logic gates and luminescent sensors based on photoinduced electron transfer. *Luminescence Applied in Sensor Science*, **2011**: 1-28. DOI: 10.1007/128_2010_96.
89. De Silva A P, Moody T S, Wright G D. Fluorescent PET (Photoinduced Electron Transfer) sensors as potent analytical tools. *Analyst*, **2009**, 134(12): 2385-2393. DOI: 10.1039/B912527M.
90. de Silva P A, Gunaratne N H Q, McCoy C P. A molecular photoionic AND gate based on fluorescent signalling. *Nature,* **1993**, 364(6432): 42-44. DOI: 10.1038/364042a0.
91. Grabchev I, Qian X, Xiao Y, et al. Novel heterogeneous PET fluorescent sensors selective for transition metal ions or protons: polymers regularly labelled with naphthalimide. *New Journal of Chemistry*, **2002**, 26(7): 920-925. DOI: 10.1039/B111519G.
92. Ariztia J, Solmont K, Moïse N P, et al. PET/fluorescence imaging: An overview of the chemical strategies to build dual imaging tools. *Bioconjugate Chemistry*, **2022**, 33(1): 24-52. DOI: 10.1021/acs.bioconjchem.1c00503.
93. Sun H, Dong X, Liu S, et al. Excellent BODIPY dye containing dimesitylboryl groups as PeT-based fluorescent probes for fluoride. *The Journal of Physical Chemistry C*, **2011**, 115(40): 19947-19954. DOI: 10.1021/jp206396v.
94. Kwon Y D, Byun Y, Kim H K. 18F-labelled BODIPY dye as a dual imaging agent: Radiofluorination and applications in PET and optical imaging. *Nuclear Medicine and Biology*, **2021**, 93: 22-36. DOI: 10.1016/j.nucmedbio.2020.11.004.
95. Xu Y, Liu Y, Qian X. Novel cyanine dyes as fluorescent pH sensors: PET, ICT mechanism or resonance effect. *Journal of Photochemistry and Photobiology A: Chemistry*, **2007**, 190(1): 1-8. DOI: 10.1016/j.jphotochem.2007.03.004.
96. Liu T, Liu X, Spring D R, et al. Quantitatively mapping cellular viscosity with detailed organelle information via a designed PET fluorescent probe. *Scientific reports,* **2014**, 4(1): 5418. DOI: 10.1038/srep05418.

97. Paulus A, Desai P, Carney B, et al. Development of a clickable bimodal fluorescent/PET probe for in vivo imaging. *EJNMMI research*, **2015**, 5: 1-9. DOI: 10.1186/s13550-015-0120-4.

98. Liu S, Li D, Zhang Z, et al. Efficient synthesis of fluorescent-PET probes based on [18 F] BODIPY dye. *Chemical Communications*, **2014**, 50(55): 7371-7373. DOI: 10.1039/C4CC01411A.

99. De Clerck K, Van Oostveldt P, Rahier H, et al. Dye diffusion studies in PET fibres by confocal laser scanning microscopy and the interrelation with the glass transition. *Polymer*, **2004**, 45(12): 4105-4112. DOI: 10.1016/j.polymer.2004.03.103.

100. Niu H, Liu J, O'Connor H M, et al. Photoinduced electron transfer (PeT) based fluorescent probes for cellular imaging and disease therapy. *Chemical Society Reviews*, **2023**, 52(7): 2322-2357. DOI: 10.1039/D1CS01097B.

101. Xia H C, Xu X H, Song Q H. BODIPY-based fluorescent sensor for the recognization of phosgene in solutions and in gas phase. *Analytical chemistry*, **2017**, 89(7): 4192-4197. DOI: 10.1021/acs.analchem.7b00203.

102. Wang R, Yu F, Chen L, et al. A highly selective turn-on near-infrared fluorescent probe for hydrogen sulfide detection and imaging in living cells. *Chemical Communications*, **2012**, 48(96): 11757-11759. DOI: 10.1039/C2CC36088H.

103. Xiao P, Liu J, Wang Z, et al. A color turn-on fluorescent probe for real-time detection of hydrogen sulfide and identification of food spoilage. *Chemical Communications*, **2021**, 57(41): 5012-5015. DOI: 10.1039/D1CC01369F.

104. Sun Q, Yang S H, Wu L, et al. Detection of intracellular selenol-containing molecules using a fluorescent probe with near-zero background signal. *Analytical chemistry*, **2016**, 88(11): 6084-6091. DOI: 10.1021/acs.analchem.6b01545.

105. Zhang W, Li P, Yang F, et al. Dynamic and reversible fluorescence imaging of superoxide anion fluctuations in live cells and in vivo. *Journal of the American Chemical Society*, **2013**, 135(40): 14956-14959. DOI: 10.1021/ja408524j.

106. Wu Y, Peng X, Guo B, et al. Boron dipyrromethene fluorophore based fluorescence sensor for the selective imaging of Zn (II) in living cells. *Organic & biomolecular chemistry*, **2005**, 3(8): 1387-1392. DOI: 10.1039/B501795E.

107. Fan J, Guo K, Peng X, et al. A Hg^{2+} fluorescent chemosensor without interference from anions and Hg^{2+}-imaging in living cells. *Sensors and Actuators B: Chemical*, **2009**, 142(1): 191-196. DOI: 10.1016/j.snb.2009.08.002.

108. Fan J, Liu X, Hu M, et al. Development of an oxidative dehydrogenation-based fluorescent probe for Cu^{2+} and its biological imaging in living cells. *Analytica chimica acta*, **2012**, 735: 107-113. DOI: 10.1016/j.aca.2012.05.027.

109. Tian M, Peng X, Feng F, et al. Fluorescent pH probes based on boron dipyrromethene dyes. *Dyes and Pigments*, **2009**, 81(1): 58-62. DOI: 10.1016/j.dyepig.2008.09.004.

110. Lee M H, Park N, Yi C, et al. Mitochondria-immobilized pH-sensitive off–on fluorescent probe. *Journal of the American Chemical Society*, **2014**, 136(40): 14136-14142. DOI: 10.1021/ja506301n.

111. Zhu H, Fan J, Wang J, et al. An “enhanced PET”-based fluorescent probe with ultrasensitivity for imaging basal and elesclomol-induced HClO in cancer cells. *Journal of the American Chemical Society*, **2014**, 136(37): 12820-12823. DOI: 10.1021/ja505988g.

112. Fan J, Han Z, Kang Y, et al. A two-photon fluorescent probe for lysosomal thiols in live cells and tissues. *Scientific reports*, **2016**, 6(1): 19562. DOI: 10.1038/srep19562.

113. Zhang D, Xu N, Li H, et al. Probing thiophenol pollutant in solutions and cells with BODIPY-based fluorescent probe. *Industrial & Engineering Chemistry Research*, **2017**, 56(33): 9303-9309. DOI: 10.1021/acs.iecr.7b02557.

114. Yin G, Niu T, Gan Y, et al. A multi-signal fluorescent probe with multiple binding sites for simultaneous sensing of cysteine, homocysteine, and glutathione. *Angewandte Chemie*, **2018**, 130(18): 5085-5088. DOI: 10.1002/ange.201813935.

115. Francioso A, Baseggio Conrado A, Mosca L, et al. Chemistry and biochemistry of sulfur natural compounds: Key intermediates of metabolism and redox biology. *Oxidative Medicine and Cellular Longevity*, **2020**, 2020(1): 8294158. DOI: 10.1155/2020/8294158.

116. Liedhegner E A S, Gao X H, Mieyal J J. Mechanisms of altered redox regulation in neurodegenerative diseases—focus on S-glutathionylation. *Antioxidants & Redox Signaling*, **2012**. DOI: 10.1089/ars.2011.411.

117. Hasanuzzaman M, Bhuyan M H M B, Zulfiqar F, et al. Reactive oxygen species and antioxidant defense in plants under abiotic stress: Revisiting the crucial role of a universal defense regulator. *Antioxidants*, **2020**, 9(8): 681. DOI: 10.3390/antiox9080681.

118. Townsend D M, Tew K D, Tapiero H. The importance of glutathione in human disease. *Biomedicine & pharmacotherapy*, **2003**, 57(3-4): 145-155. DOI: 10.1016/S0753-3322(03)00043-X.

119. Filomeni G, Rotilio G, Ciriolo M R. Cell signalling and the glutathione redox system. *Biochemical pharmacology*, **2002**, 64(5-6): 1057-1064. DOI: 10.1016/S0006-2952(02)01176-0.

120. Oteiza P I. Zinc and the modulation of redox homeostasis. *Free Radical Biology and Medicine*, **2012**, 53(9): 1748-1759.DOI: 10.1016/j.freeradbiomed.2012.08.568.

121. Ganguly P, Alam S F. Role of homocysteine in the development of cardiovascular disease. *Nutrition journal*, **2015**, 14: 1-10. DOI: 10.1186/1475-2891-14-6.

122. Liu W, Chen J, Xu Z. Fluorescent probes for biothiols based on metal complex. *Coordination Chemistry Reviews*, **2021**, 429: 213638. DOI: 10.1016/j.ccr.2020.213638.

123. Sen C K, Packer L. Thiol homeostasis and supplements in physical exercise. T*he American journal of clinical nutrition*, **2000**, 72(2): 653S-669S. DOI: 10.1093/ajcn/72.2.653S.

124. Cook J A, Gius D, Wink D A, et al. Oxidative stress, redox, and the tumor microenvironment. *Seminars in radiation oncology*, **2004,** 14(3): 259-266. DOI: 10.1016/j.semradonc.2004.04.001.

125. Xie X, Peng Z, Wang Z, et al. Monitoring biothiols dynamics in living cells by ratiometric fluorescent gold carbon dots. *Talanta*, **2020**, 218: 121214. DOI: 10.1016/j.talanta.2020.121214.

Chapter 2. Synthesis, Characterization and Biothiols Detection

Abstract

This chapter describes the synthesis of PT/BT-Boc and BT-DNBS, both obtained with high yields. The impact of introducing the BCF group on photophysical properties was analyzed, revealing increased molar absorptivity, redshifted absorption and emission wavelengths, and a significantly enlarged Stokes shift. Furthermore, the in vitro response of BT-DNBS to biothiols was systematically evaluated, including optimization of detection conditions, concentration-dependent fluorescence changes, selectivity analysis, and time- and pH-dependent studies. The recognition mechanism was investigated using ^{1}H NMR and mass spectrometry, supported by DFT calculations. Finally, BT-DNBS was compared with other DNBS-based probes, demonstrating its enhanced performance for biothiol detection.

2.1 Introduction

In this chapter, we systematically describe the synthesis, structural characterization, and photophysical properties of **BT-DNBS**, a novel fluorescent probe designed for the detection of biothiols. **BT-DNBS** incorporates a donor-π-acceptor (D-π-A) framework and a DNBS group that acts as a fluorescence quencher via photoinduced electron transfer (PET). Upon interaction with biothiols, the DNBS group is cleaved, effectively restoring the fluorescence of the probe.

The chapter begins by outlining the synthetic pathway for **BT-DNBS**, highlighting its efficiency and scalability. Following this, the photophysical properties precursor molecules (PT-Boc and BT-Boc) are explored, including their absorption and emission spectra, Stokes shifts. These analyses provide a comprehensive understanding of the inherent properties of **BT-DNBS**, laying the groundwork for evaluating its performance as a biothiol-specific fluorescent probe. Additionally, we optimized the spectroscopic testing conditions to ensure the reproducibility and reliability of **BT-DNBS**'s fluorescence response. Through detailed spectroscopic analysis, we validated its selectivity, time dependence, and pH responsiveness in detecting biothiols. Finally, the sensing mechanism was investigated using both experimental and computational

approaches, including density functional theory (DFT) calculations, to gain insights into the molecular orbital interactions that govern the fluorescence switching process.

This chapter establishes the foundational properties of **BT-DNBS**, providing essential context for its application in live-cell imaging.

2.2 Materials, Instruments and Methods

Unless otherwise noted, all solvents and chemicals were of reagent grade, with purity ranging from 95% to 99%. Solvents used for spectral analysis were of high purity, at 99.8%. All chemicals and solvents were purchased from Sigma-Aldrich, Kanto Chemical, Tokyo Chemical Industry, Fuji Film, and Wako Pure Chemical Industries, and were used without further purification. Reaction processes were monitored by thin-layer chromatography (TLC) on pre-coated silica gel plates (silica gel 60, 0.25, F-254), visualized under UV light and/or by chromogenic reaction. Silica gel 60 (230-400 mesh) was used for column chromatography.

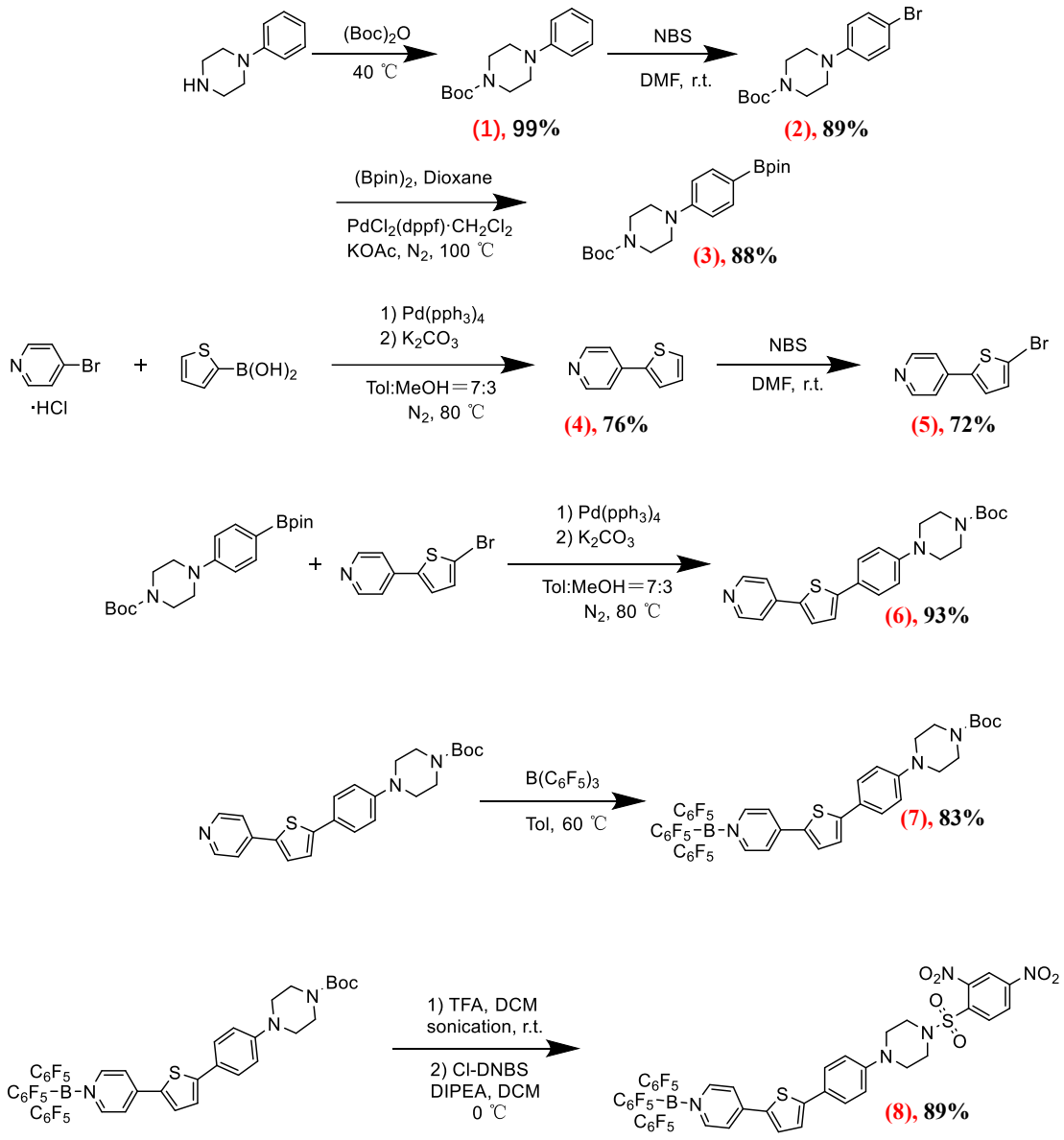
^{1}H-NMR spectra were recorded on JEOL JNN-EX 400 MHz or JEOL JNM-ECZR 500 MHz spectrometers at room temperature. ^{13}C NMR spectra were recorded at 125 MHz. Chemical shifts (δ) were reported as ppm in $CDCl_3$ or DMSO-d_6, with TMS as the internal standard. Coupling constants (J) were expressed in hertz (Hz). Mass spectra were carried out under ESI conditions (Thermo Scientific Exactive, Thermo Fisher Scientific K.K., Tokyo, Japan, and JMS-T100LP (JEOL) USA Inc.).

Absorption spectra were measured on a JASCO V-560 spectrophotometer. Fluorescence spectra were measured by a HITACHI F-7000 fluorescence spectrometer. pH was measured by a compact pH meter LAQUATWIN-PH-11B.

Preparation for Spectroscopic Analysis

BT-DNBS was dissolved in DMSO to prepare a 50 μM stock solution. All analytes were dissolved in PBS buffer to prepare 1 mM stock solutions, freshly prepared before each experiment. Unless otherwise noted, all spectroscopic analyses were conducted at room temperature with an incubation period of 20 minutes. The experimental conditions included **BT-DNBS** at 10 μM and analytes at 100 μM, in a DMSO/PBS buffer (9:1, v/v), with excitation at 434 nm and emission at 630 nm. Limit of detection (LOD) was calculated using the formula: Detection limit = 3**σ**/**k** (where **σ** represents the standard deviation of the blank measurements, **k** is the slop of the fluorescence intensity (**FI**) versus analytes concentration curve.

2.3 Synthesis Scheme

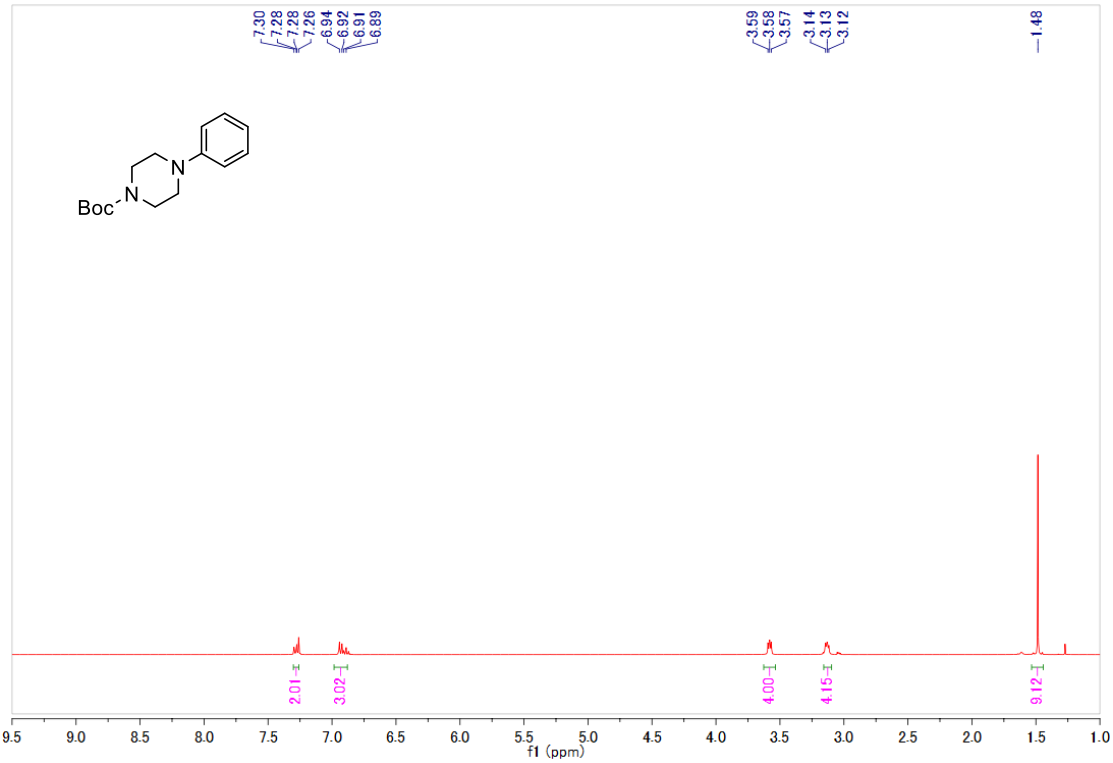


The yields are expressed as percentages.

***Tert*-butyl 4-phenylpiperazine-1-carboxylate (1).**

1-Phenylpiperazine (6.15 g, 37.9 mmol) and di-*tert*-butyl pyrocarbonate (9.10 g, 41.7 mmol) were combined and subjected to sonication for 40 minutes in a water bath at 40 ℃. Upon the completion of the reaction, as monitored by thin-layer chromatography (TLC) (R_f=0.3, hexane: ethyl acetate=5:1). the mixture was cooled down and transitioned into a transparent solid compound **1.** (11 g, 99%).

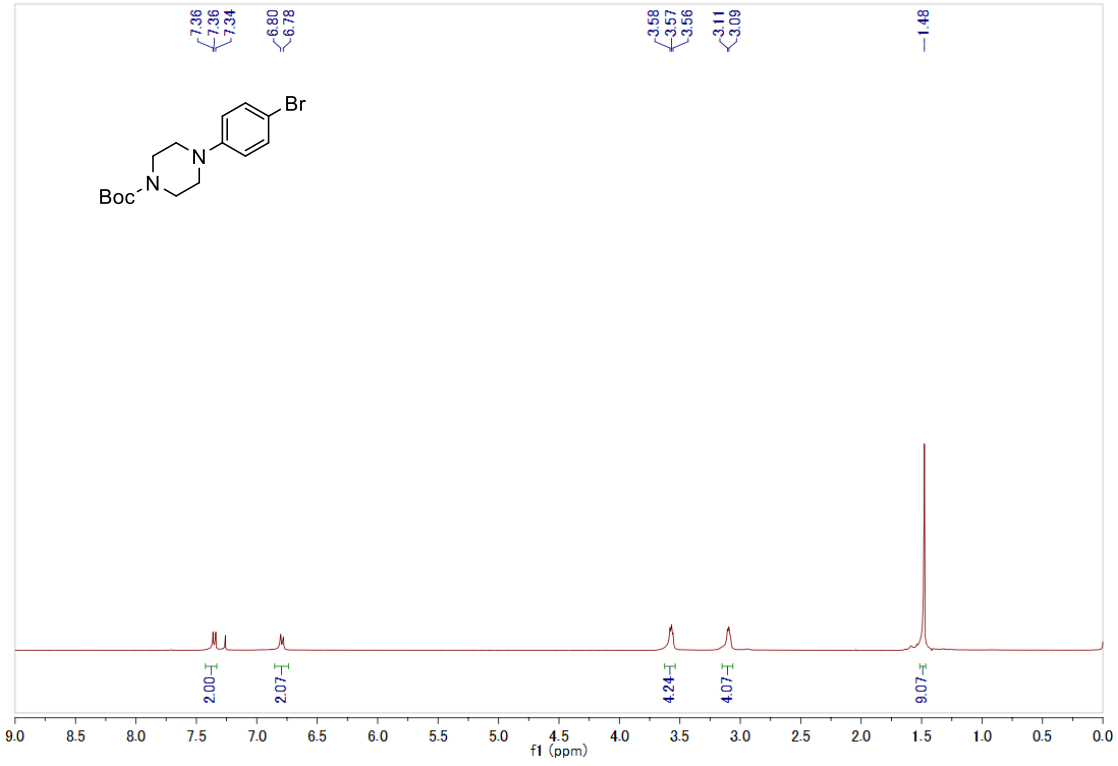
^{1}H NMR (400 MHz, $CDCl_3$, TMS, r.t.): δ 7.31-7.25 (m, 2H), 6.99-6.85 (m, 3H), 3.58 (t, J = 5.2 Hz, 4H), 3.13 (t, J = 5.2 Hz, 4H), 1.48 (s, 9H).



***Tert*-butyl 4-(4-bromophenyl) piperazine-1-carboxylate (2).**

N-Bromosuccinamide (2.39 g, 12.58 mmol) was dissolved in 15 mL of anhydrous DMF and added dropwise to a stirred solution of compound **1** (3 g, 11.43 mmol) in 15 mL of anhydrous DMF, which has been shielded from light with aluminum foil at 0 ℃. After the addition of NBS, the reaction mixture was then allowed to reach room temperature and stirred for 24 hours. Upon completion of the reaction, as confirmed by TLC (R_f=0.4, hexane: ethyl acetate = 2:1), ice-water (10 mL) was then introduced, leading to the precipitation of the product. The resulting precipitate was isolated by filtration, and the crude product was subsequently purified by silica gel column chromatography (hexane: ethyl acetate = 15:1) and evaporated to yield a white solid **2**. (3.47g, 89%)

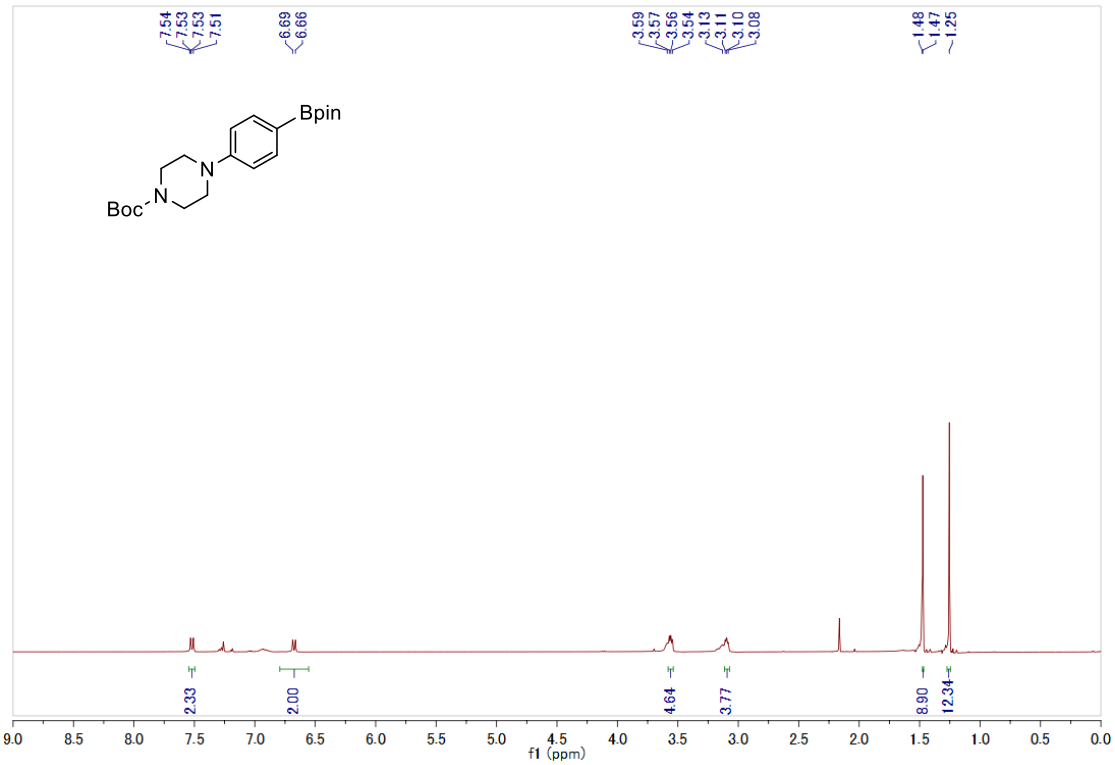
^{1}H NMR (400 MHz, $CDCl_3$, TMS, r.t.): δ 7.35 (d, J = 8.8 Hz, 2H), 6.79 (d, J = 8.8 Hz, 2H), 3.57 (t, J = 5.2 Hz, 4H), 3.10 (t, J = 5.2 Hz, 4H), 1.48 (s, 9H).



***Tert*-butyl 4-(4-(4,4,5,5-tetramethyl-1,3,2-dioxaborolan-2-yl) phenyl) piperazine-1-carboxylate (3).**

In a dry two-necked flask, compound **2** (1.5 g, 4.4 mmol), KOAc (518 mg, 5.27 mmol), and $PdCl_2(dppf)\cdot CH_2Cl_2$ (72 mg, 0.09 mmol) were dissolved in 1,4-dioxane (20 mL). The resulting mixture was purged with N_2 three times and refluxed at 100 ℃ for 5 minutes. Subsequently, a mixture of bis(pinacolato)diboron (1.34 g, 5.27 mmol) and 1,4-dioxane (15 mL) was added slowly, and the reaction stirred for 14 hours. After the completion of the reaction, as confirmed by TLC (R_f=0.2, hexane: ethyl acetate = 9:1), the mixture was then extracted with ethyl acetate, washed with water and brine, and dried over anhydrous Na_2SO_4 successively. The drying agent was then removed by filtration. The crude product was further purified by silica gel chromatography (hexane: ethyl acetate = 9:1) and evaporated to yield a white solid **3**. (1.5 g, 88%)

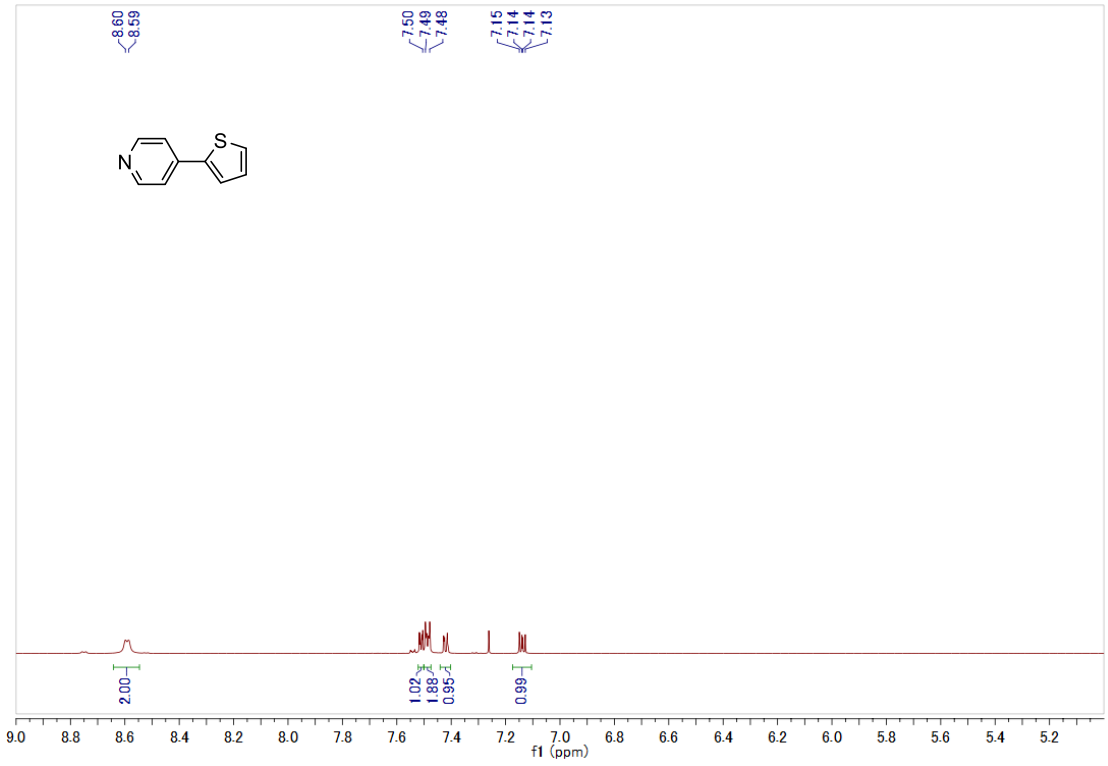
^{1}H NMR (400 MHz, $CDCl_3$, TMS, r.t.): δ 7.52 (d, *J* = 8.8 Hz, 2H), 6.68 (d, *J* = 8.8 Hz, 2H), 3.56 (t, *J* = 5.2 Hz, 4H), 3.10 (t, *J* = 5.2 Hz, 4H), 1.48 (s, 9H) 1.25 (s, 12H).



4-(thiophen-2-yl) pyridine (4).

In a dried flask, 4-Bromopyridine hydrochloride (2 g, 10.28 mmol), 2-thienylboronic acid (1.32 g, 10.28 mmol), K_2CO_3 (2.84 g, 20.56 mmol), and Pd $(PPh_3)_4$ (593 mg, 0.50 mmol) were dissolved in a mixed solvent (Toluene/MeOH = 7/3, 50 mL). The reaction proceeded under a nitrogen atmosphere at 80 ℃ for 18 hours, monitored by TLC (R_f=0.2, hexane: ethyl acetate = 3:2). Upon completion, the reaction mixture was quenched with ice-water and extracted with ethyl acetate. The combined organic extracts were concentrated, resulting in a 10% volume of the initial amount. The concentrated organic phase underwent extraction with 0.5 N HCl (5 × 20 mL), followed by neutralization using a saturated $NaHCO_3$ solution until no more gas bubbles were produced. Then the mixture underwent an additional extraction with ethyl acetate, followed by drying over anhydrous Na_2SO_4. Concentration of the organic phase yielded a gray solid product **4** (1,27 g, 76%).

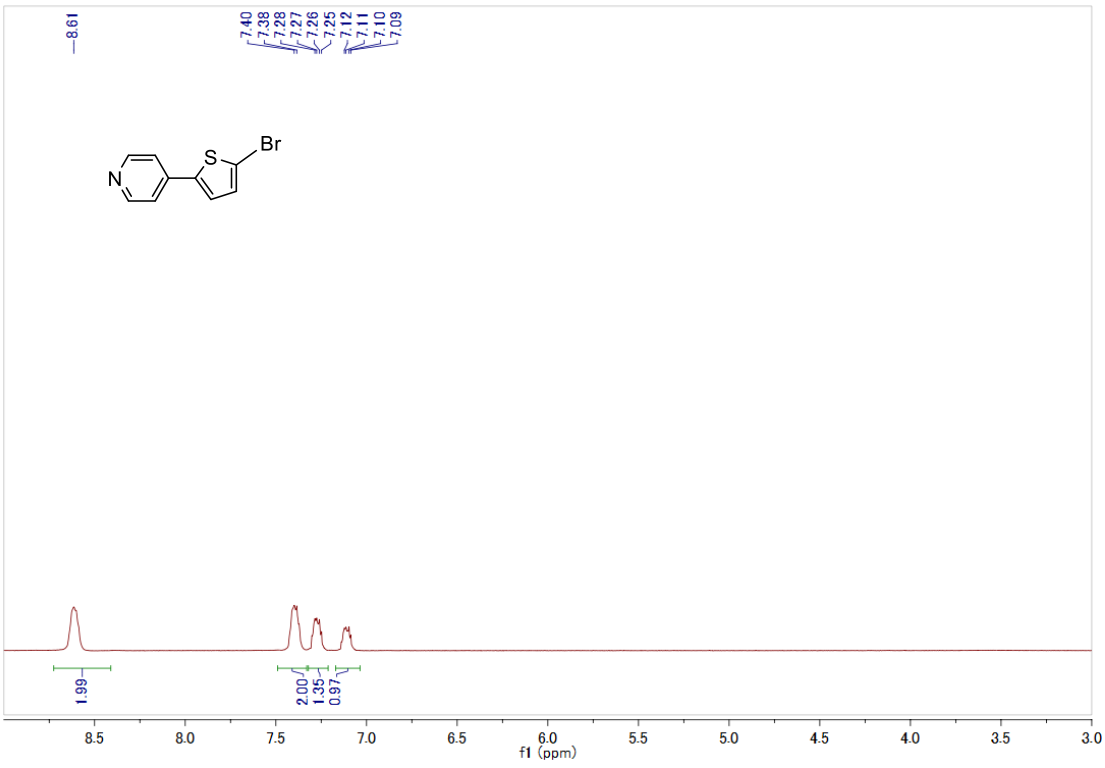
^{1}H NMR (400 MHz, $CDCl_3$, TMS, r.t.): δ 8.60 (d, *J* = 4.8 Hz, 2H), 7.50 (dd, *J* = 3.6 Hz, 1.2 Hz, 1H), 7.48 (dd, *J* = 4.8 Hz, 2.0 Hz, 2H), 7.42 (dd, *J* = 5.2 Hz, 1.2 Hz, 1H), 7.14 (dd, *J* = 5.2 Hz, 1.2 Hz, 1H).



4-(5-bromothiophen-2-yl) pyridine (5).

Compound **4** (990 mg, 6.14 mmol) was dissolved in dehydrated DMF 20 mL in a dried flask at 0 ℃. A mixture of N-Bromosuccinamide (1.31 g, 7.37 mmol) and DMF 5 mL was then added dropwise to the reaction system under darkness. After 30 minutes, the reaction mixture was further stirred for 18 hours at room temperature. Upon completion of the reaction, as monitored by TLC (R_f=0.15, hexane: ethyl acetate = 5:1), the mixture was extracted with ethyl acetate, washed by $NaHCO_{3(aq)}$, $NaCl_{(aq)}$, dried over anhydrous Na_2SO_4. The drying agent was then removed by filtration. The crude product was subsequently purified by silica gel chromatography (hexane: ethyl acetate = 5:1) and evaporated to yield a brown solid **5**. (1.06 g, 72%)

^{1}H NMR (400 MHz, $CDCl_3$, TMS, r.t.): δ 8.61 (br, 2H), 7.39 (d, J = 5.6 Hz, 2H), 7.27 (d, J = 1.6 Hz, 1H), 7.10 (d, J = 4.0 Hz, 1H).

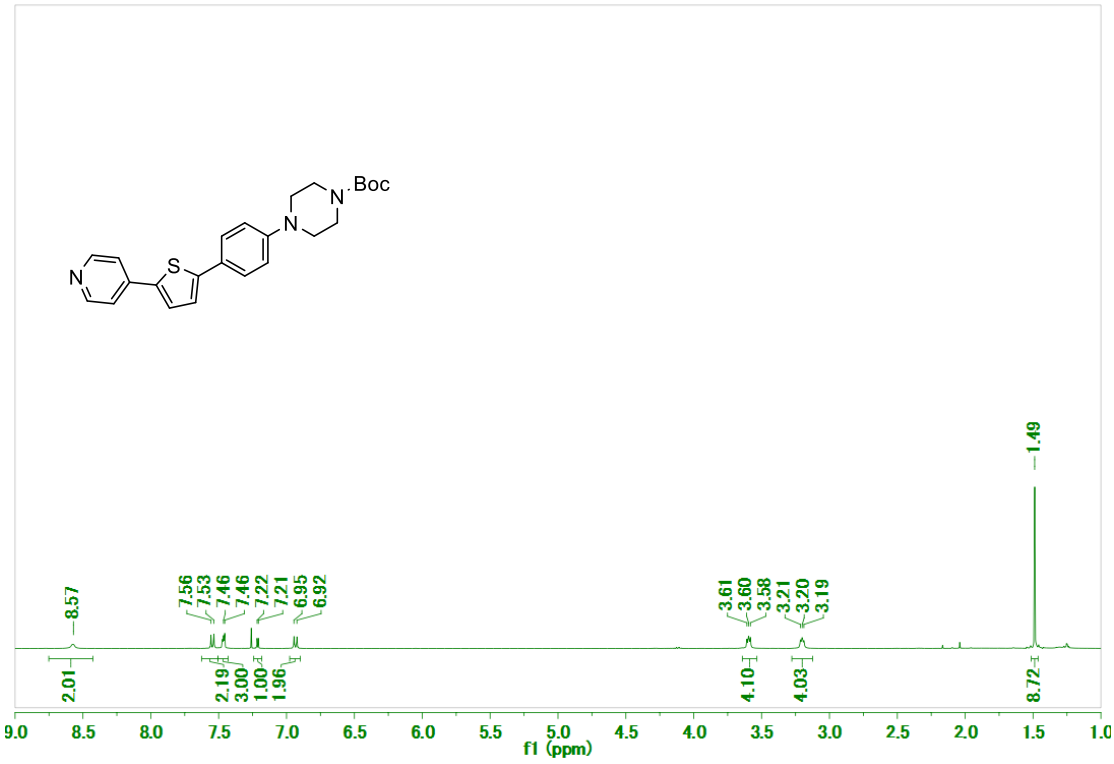


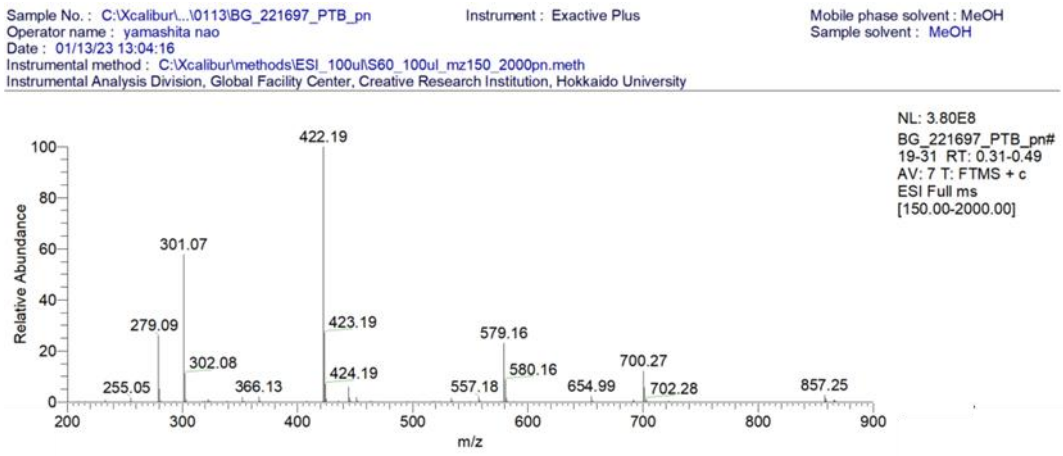
***Tert*-butyl 4-(4-(5-(pyridin-4-yl) thiophen-2-yl) phenyl) piperazine-1-carboxylate (6), PT-Boc.**

In a dried flask, compound **3** (888 mg, 2.29 mmol), compound **5** (500 mg, 2.08 mmol), K_2CO_3 (575 mg, 4.16 mmol), and Pd $(PPh_3)_4$ (170 mg, 0.14 mmol) were dissolved in a mixed solvent (Toluene/MeOH = 7/3, 25 mL). The reaction proceeded under a nitrogen atmosphere at 80 ℃ for 12 hours, monitored by TLC (R_f=0.2, hexane: ethyl acetate = 3:2). Upon completion, the reaction mixture was quenched with ice-water and extracted with ethyl acetate, washed with H_2O, and brine, then dried over anhydrous Na_2SO_4. The drying agent was then removed by filtration. The crude product was subsequently purified by silica gel chromatography (hexane: ethyl acetate = 1:1) and evaporated to yield a yellow powder **6**. (815 mg, 93%)

^{1}H NMR (400 MHz, $CDCl_3$, TMS, r.t.): δ 8.57 (br, 2H), 7.55 (d, *J* = 8.8 Hz, 2H), 7.46 (m, 3H), 7.21 (d, *J* = 4.0 Hz, 1H), 6.93 (d, *J* = 8.8 Hz, 2H), 3.60 (t, *J* = 5.2 Hz, 4H), 3.20 (t, *J* = 5.2 Hz, 4H), 1.49 (s, 9H).

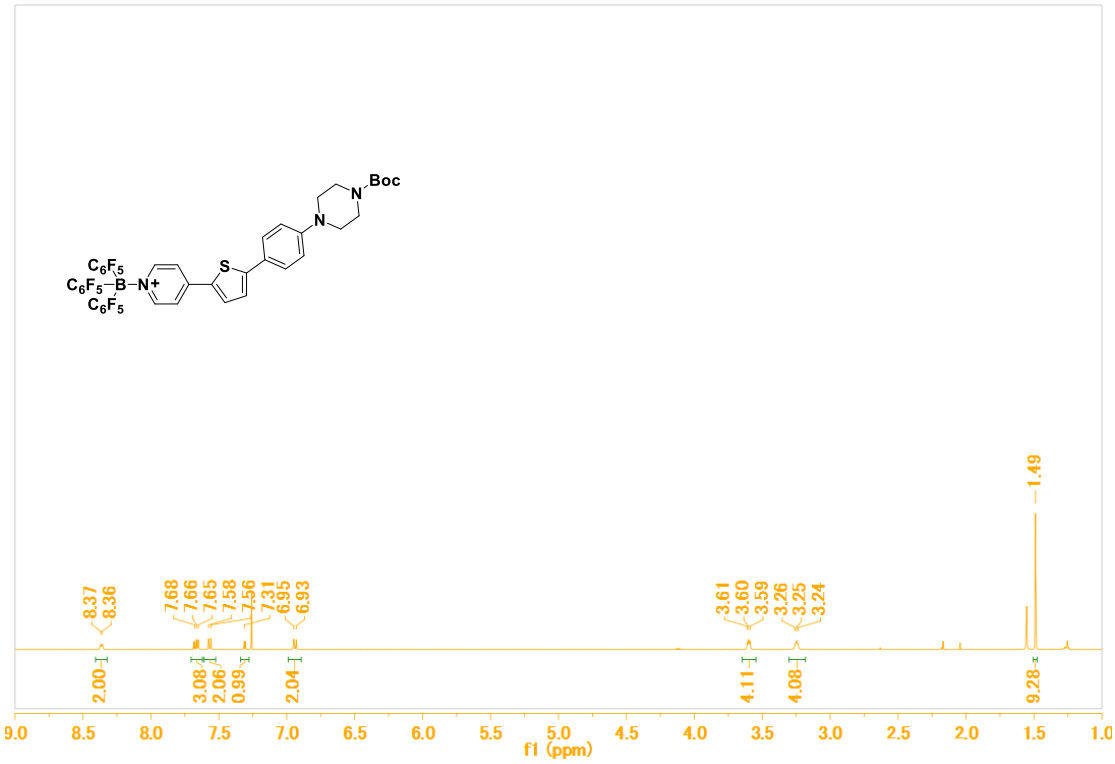
ESI-Mass (m/z): $[M+H]^+$ calcd for $C_{24}H_{28}N_3O_2S^+$: 422.1902; Found: 422.19.


Boc
N
N
S
N
8.57
7.56
7.53
7.46
7.46
7.22
7.21
6.95
6.92
3.61
3.60
3.58
3.21
3.20
3.19
1.49
2.01
2.19
3.00
1.00
1.96
4.10
4.03
8.72
9.0
8.5
8.0
7.5
7.0
6.5
6.0
5.5
5.0
4.5
4.0
3.5
3.0
2.5
2.0
1.5
1.0
f1 (ppm)


Sample No. : C:\Xcalibur\...\0113\BG_221697_PTB_pn
Operator name : yamashita nao
Date : 01/13/23 13:04:16
Instrumental method : C:\Xcalibur\methods\ESI_100ul\S60_100ul_mz150_2000pn.meth
Instrumental Analysis Division, Global Facility Center, Creative Research Institution, Hokkaido University
Instrument : Exactive Plus
Mobile phase solvent : MeOH
Sample solvent : MeOH
NL: 3.80E8
BG_221697_PTB_pn#
19-31 RT: 0.31-0.49
AV: 7 T: FTMS + c
ESI Full ms
[150.00-2000.00]
Relative Abundance
m/z
422.19
301.07
279.09
423.19
579.16
302.08
580.16
700.27
424.19
255.05
366.13
557.18
654.99
702.28
857.25

4-(5-(4-(4-(*tert*-butoxycarbonyl) piperazin-1-yl) phenyl) thiophen-2-yl)-1λ^4-pyridin-1-yl) tris(pentafluorophenyl) borate (7), BT-Boc.

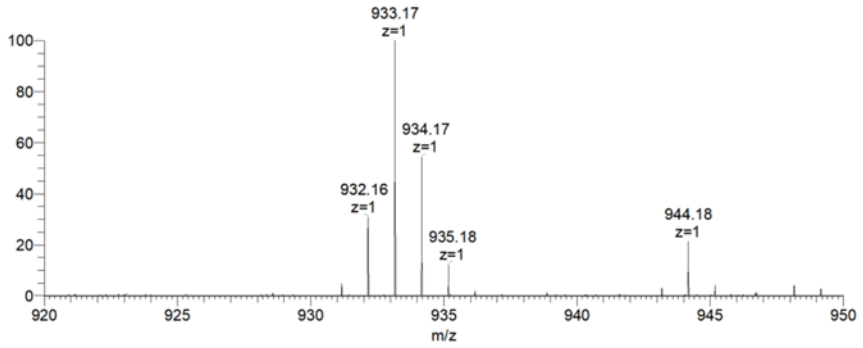
In a dried flask, **PT-Boc** (200 mg, 0.48 mmol) and tris(pentafluorophenyl)borane (270 mg, 0.53 mmol) were dissolved in toluene (5 mL) at 60 ℃ under nitrogen condition and stirred for 24 hours. Following the completion of the reaction, as monitored by TLC (R_f=0.5, hexane: ethyl acetate = 1:1), the reaction mixture was extracted with ethyl acetate, subjected to $NaHCO_{3(aq)}$ and brine washes, dried over anhydrous Na_2SO_4. The drying agent was then removed by filtration. The crude product was further purified via silica gel chromatography (hexane: ethyl acetate = 5:1) and evaporated, resulting in the isolation of compound **7** as a yellow solid. (371 mg, 83%)
^{1}H NMR (500 MHz, $CDCl_3$, TMS, r.t.): δ 8.36 (d, *J* = 6.0 Hz, 2H), 7.68 (d, *J* = 4.0 Hz, 1H), 7.66 (d, *J* = 7.5 Hz, 2H), 7.57 (d, *J* = 9.0 Hz, 2H), 7.31 (d, *J* = 4.0 Hz, 1H), 6.94 (d, *J* = 9.0 Hz, 2H), 3.60 (t, *J* = 5.0 Hz, 4H), 3.25 (t, *J* = 5.0 Hz, 4H), 1.49 (s, 9H).
ESI-Mass (m/z): $[M]^+$ calcd for $C_{42}H_{27}BF_{15}N_3O_2S^+$: 933.1672; Found: 933.17



Sample No. : C:\Xcalibur\...\0113\221707_B_PTB_pn
Operator name : yamashita nao
Date : 01/13/23 12:26:45
Instrumental method : C:\Xcalibur\methods\ESI_100ul\S60_100ul_mz150_2000pn.meth
Instrumental Analysis Division, Global Facility Center, Creative Research Institution, Hokkaido University

Instrument : Exactive Plus

Mobile phase solvent : MeOH
Sample solvent : MeOH



NL: 1.56E4
221707_B_PTB_pn#18-32 RT: 0.30-0.52 AV: 8 T: FTMS - p ESI Full ms [150.0000-2000.0000]

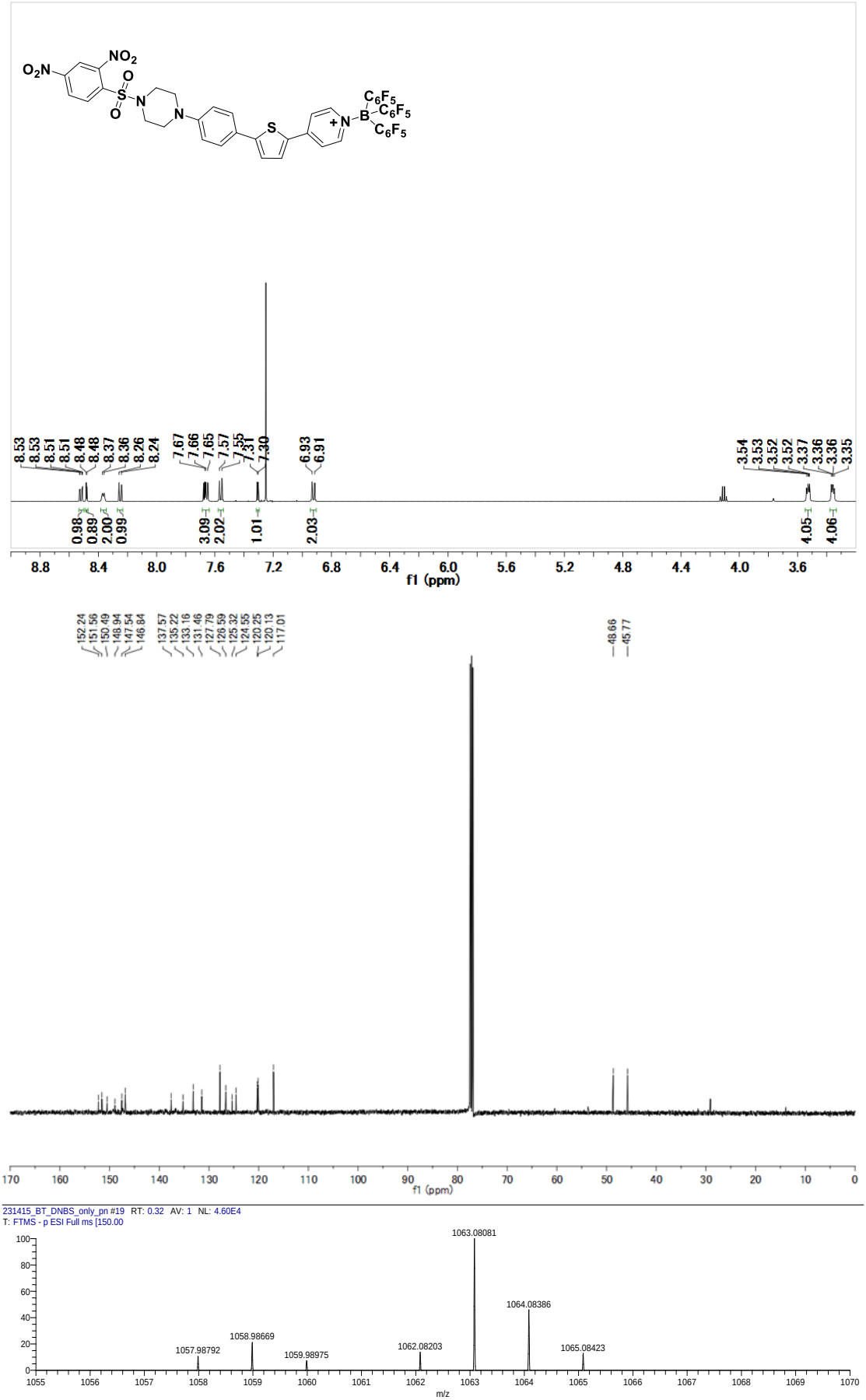
4-(5-(4-(4-((2,4-dinitrophenyl) sulfonyl) piperazin-1-yl) phenyl) thiophen-2-yl)-1λ^4-pyridin-1-yl) tris (pentafluorophenyl) borate (8), BT-DNBS.

BT-Boc (100 mg, 0.11 mmol) was dissolved in dichloromethane (3 mL) in a dried flask. Trifluoroacetic acid (0.6 mL) was subsequently added dropwise to the flask, and the resulting mixture was sonicated for 1 hour at room temperature. The solvent was then evaporated, and the residue underwent vacuum drying for 15 hours. Following this, the resultant material was dissolved in dichloromethane (3 mL), and N,N-diisopropylethylamine (57 μL, 0.33 mmol) was added, maintaining the reaction at 0 ℃. A mixture of dinitrobenzenesulfonyl chloride (59 mg, 0.22 mmol) and dichloromethane (2 mL) was then slowly added to the reaction system and stirred for 30 minutes. The reaction mixture was subsequently allowed to return to room temperature and stirred for an additional 16 hours. Upon completion of the reaction, as monitored by TLC (R_f=0.2, hexane: ethyl acetate = 1:1), the mixture was subjected to purification via silica gel chromatography (hexane: ethyl acetate = 2:1) employing the dry loading technique and evaporation, resulting in the isolation of compound **8** as a brown solid. (104 mg, 89%)

^{1}H NMR (500 MHz, $CDCl_3$, TMS, r.t.): δ 8.53 (dd, *J* = 8.5, 2.0 Hz, 1H), 8.49 (d, *J* = 2.0 Hz, 1H) 8.38 (d, *J* = 6.5 Hz, 2H), 8.26 (d, *J* = 9.0 Hz, 1H), 7.68 (d, *J* = 4.0 Hz, 1H), 7.67 (d, *J* = 7.5 Hz, 2H), 7.57 (d, *J* = 9.0 Hz, 2H), 7.32 (d, *J* = 4.0 Hz, 1H), 6.93 (d, *J* = 9.0 Hz, 2H), 3.54 (t, *J* = 5.0 Hz, 4H), 3.37 (t, *J* = 5.0 Hz, 4H).

^{13}C NMR (125 MHz): δ 152.24, 151.56, 150.49, 148.94, 147.54, 146.84, 137.57, 135.22, 133.16, 131.46, 127.79, 126.59, 125.32, 124.55, 120.19, 117.01, 48.66, 45.77.

ESI-Mass (m/z): $[M]^+$ calcd for $C_{43}H_{21}BF_{15}N_5O_6S_2^+$: 1063.0787; Found: 1063.0808.


8.53
8.53
8.51
8.51
8.48
8.48
8.37
8.36
8.26
8.24
7.67
7.66
7.65
7.57
7.55
7.31
7.30
6.93
6.91
3.54
3.53
3.52
3.52
3.37
3.36
3.36
3.35
0.98
0.89
2.00
0.99
3.09
2.02
1.01
2.03
4.05
4.06
f1 (ppm)
152.24
151.56
150.49
148.94
147.54
146.84
137.57
135.22
133.16
131.46
127.79
126.59
125.32
124.55
120.25
120.13
117.01
48.66
45.77
f1 (ppm)
231415_BT_DNBS_only_pn #19 RT: 0.32 AV: 1 NL: 4.60E4
T: FTMS - p ESI Full ms [150.00
1063.08081
1064.08386
1058.98669
1057.98792
1059.98975
1062.08203
1065.08423
m/z

2.4 Photophysical properties of PT/BT-Boc

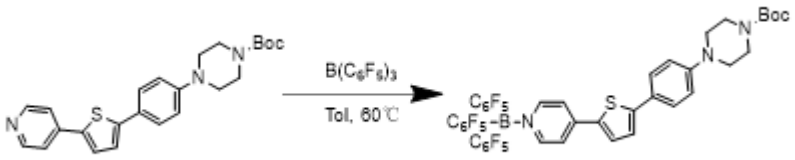


Fig. 2.1 Structure of **PT/BT-Boc**. Left: **PT-Boc**. Right: **BT-Boc**,

To explore the potential application of **BT-Boc** as a precursor for the biothiol-responsive probe **BT-DNBS**, the photophysical properties of **PT-Boc** and **BT-Boc** were investigated in various solvents. The comparison highlights how the structural modification of **BT-Boc**, specifically the coordination of the pyridine nitrogen to a BCF group, affects its optical properties, which are crucial for designing functional fluorescent probes. Both **PT-Boc** and **BT-Boc** exhibit distinct absorption and emission behaviors depending on the solvent polarity (Fig. 2.2 and Table 2.1). In general, **BT-Boc** demonstrates a red-shifted emission and significantly larger Stokes shifts compared to **PT-Boc** across all solvents. For example, in hexane, **PT-Boc** shows an absorption maximum at 355 nm and an emission maximum at 420 nm, with a Stokes shift of 65 nm. In contrast, **BT-Boc** absorbs at 437nm and emits at 531 nm in the same solvent, with a larger Stokes shift of 94 nm. This trend is consistent in polar solvents such as acetonitrile (ACN) and dimethylformamide (DMF), where **BT-Boc** exhibits absorption and emission maxima at 429/438 nm and 633/643 nm, respectively, with Stokes shifts reaching up to 205 nm.

The incorporation of the BCF group in **BT-Boc** enhances intramolecular charge transfer (ICT) interactions, making its optical properties more sensitive to solvent polarity. This increased polarity sensitivity is evidenced by the pronounced bathochromic shifts in both absorption and emission spectra as the solvent polarity increases, particularly in polar aprotic solvents like DMF and DMSO. Additionally, the

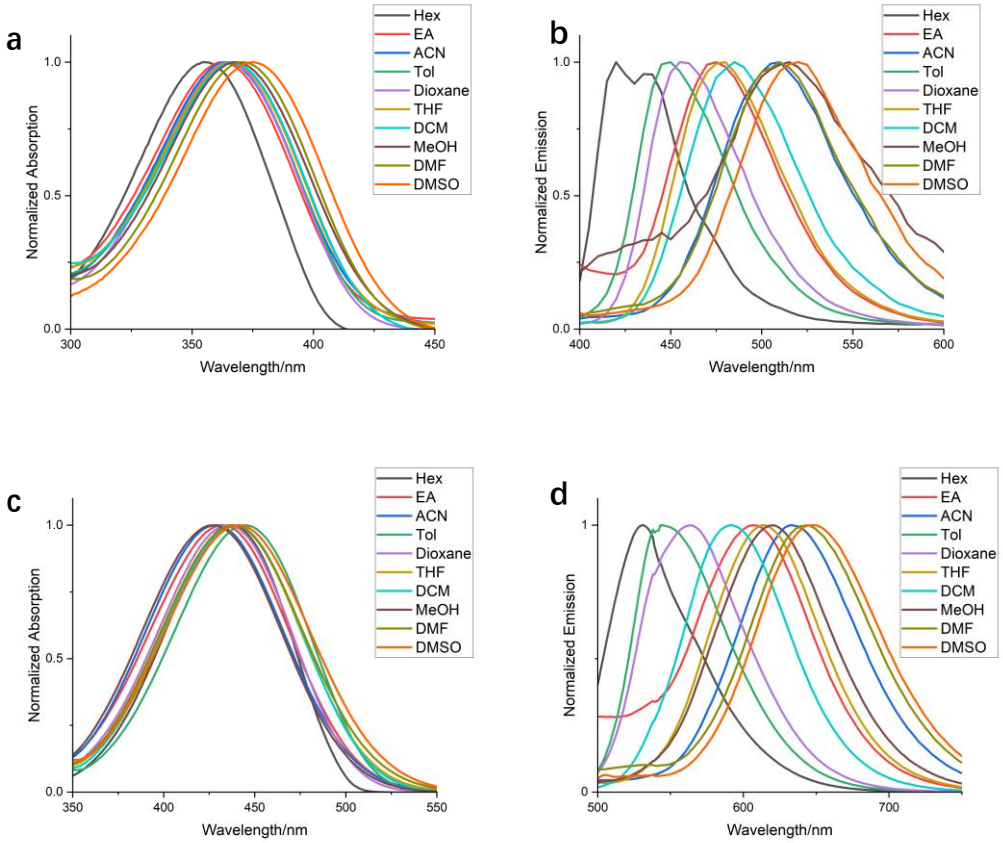


Fig. 2.2 Absorption and emission spectra of PT-Boc and BT-Boc in various solvents. **a/c**: Absorption spectra of PT-Boc/BT-Boc. **b/d**: Emission spectra of PT-Boc/BT-Boc.

larger Stokes shifts of BT-Boc compared to PT-Boc suggest notable differences between their ground and excited states. This characteristic might be attributed to the influence of the BCF group on the electronic structure of **BT-Boc**, which could facilitate enhanced separation between absorption and emission peaks [1]. Such a property is advantageous for fluorescence-based detection, as it minimizes spectral overlap and improves the accuracy of signal measurement.

These findings underscore **BT-Boc**'s advantages as a precursor for biothiol detection. Its red-shifted emission and strong polarity sensitivity suggest potential for high signal-to-noise ratio imaging in complex biological environments. Moreover, the observed photophysical properties lay a solid foundation for the investigation of **BT-DNBS**'s biothiol-responsive mechanism.

Table 2.1 Spectroscopic data of PT-Boc (black font) and BT-Boc (red font).

Solvent	λ_{abs}/nm		λ_{em}/nm		$\varepsilon/M^{-1}cm^{-1}$		Stokes shift/nm	
Hex	355	437	420	531	1.4×10^4	4.3×10^4	65	94
Tol	365	445	450	543	2.4×10^4	3.0×10^4	85	98
DCM	367	439	487	591	2.2×10^4	3.2×10^4	120	152
THF	366	438	480	614	2.6×10^4	4.2×10^4	114	176
EA	363	432	473	607	2.6×10^4	4.9×10^4	110	175
Dioxane	365	435	455	563	2.4×10^4	3.4×10^4	90	128
ACN	364	429	505	633	2.1×10^4	2.9×10^4	141	204
DMF	371	438	511	643	2.8×10^4	3.0×10^4	140	205
MeOH	367	427	517	621	2.2×10^4	2.7×10^4	150	194
DMSO	375	441	520	648	2.2×10^4	2.6×10^4	145	207

Hex: Hexane, Tol: Toluene, DCM: Dichloromethane, THF: Tetrahydrofuran

EA: Ethyl acetate, Dioxane: 1,4-Dioxane, ACN: Acetonitrile

DMF: Dimethylformamide, MeOH: Methanol, DMSO: Dimethyl sulfoxide

2.5 Optimization of Spectroscopic Testing Conditions

To optimize the experimental conditions for biothiol detection, the fluorescence intensity of **BT-DNBS** (10 μM) was evaluated in different DMSO/PBS ratios (Fig. 2.3). The results demonstrated that the fluorescence intensity was significantly influenced by the solvent composition, with the highest intensity observed at a DMSO/PBS ratio of 9:1 (v/v). This ratio likely provides an optimal balance between the dye's solubility in the organic phase and the biological relevance of the aqueous phase. Consequently, subsequent experiments involving biothiol detection was conducted under this optimized solvent condition.

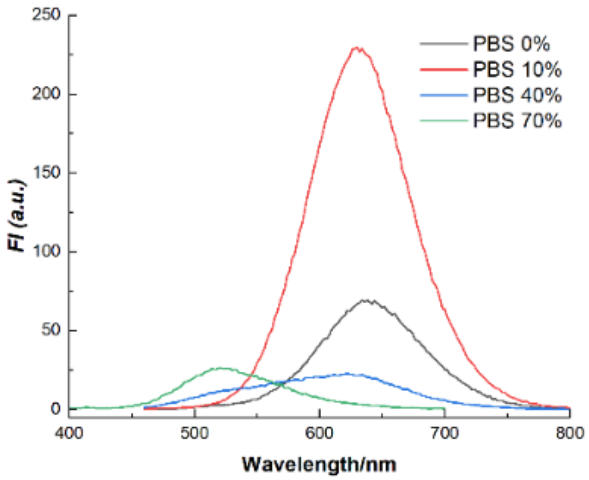


Fig. 2.3 Fluorescence spectra of **BT-DNBS** (10 μM) in DMSO with varying PBS fractions after a 20-minute incubation with GSH (100 μM).

2.6 Spectroscopic analysis of BT-DNBS towards biothiols

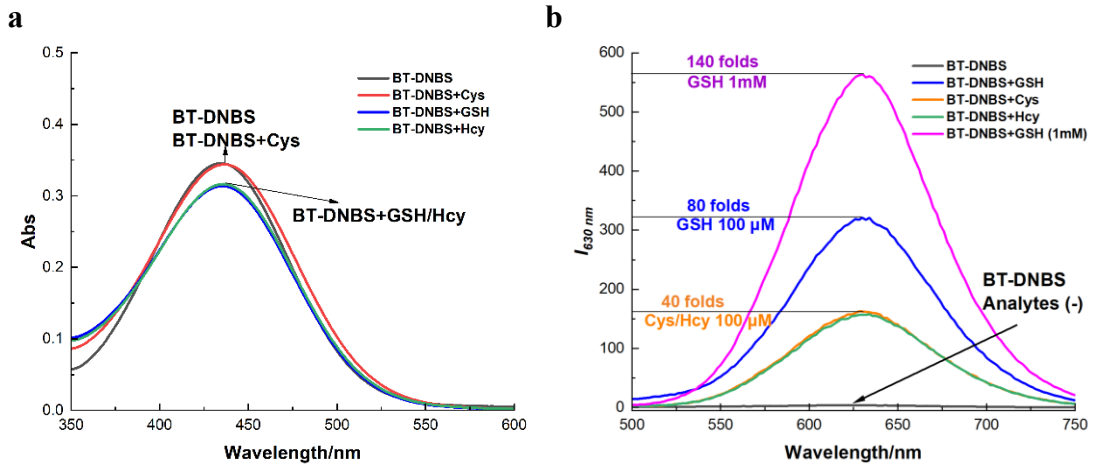


Fig. 2.4 Spectral analysis of **BT-DNBS** towards biothiols. a): absorption spectra, b): emission spectra of **BT-DNBS** (10 μM) in DMSO/PBS (9:1, v/v, pH 7.4) in the presence of biothiols (100 μM). Incubated for 20 min, λ_{ex}=434 nm, λ_{em}=630 nm.

To evaluate the interaction between the fluorescent dye **BT-DNBS** and biothiols, we recorded both absorption and emission spectra of **BT-DNBS** (10 μM) in the presence and absence of biothiols (100 μM). As illustrated in Fig. 2.4, the absorption spectra showed negligible differences between the two conditions, indicating that the electronic absorption properties of the dye remain largely unchanged upon reaction with biothiols. This consistency suggests that the interaction with biothiols does not significantly alter the ground-state electronic structure of the dye. In contrast, the emission spectra demonstrated pronounced differences. Without biothiols, **BT-DNBS** exhibited only weak fluorescence, which can be attributed to efficient quenching by the DNBS group via a photoinduced electron transfer (PET) mechanism. The DNBS moiety effectively suppresses fluorescence, likely by acting as an electron acceptor that interrupts the normal radiative decay pathway of the fluorophore. However, upon the addition of biothiols, a remarkable turn-on fluorescence response was observed (Fig. 2.5). The fluorescence intensity increased significantly, with a strong and distinct orange fluorescence signal becoming evident. This response is due to the cleavage of the DNBS

group by biothiols, which restores the emissive state of the fluorophore by disrupting the PET-based quenching.

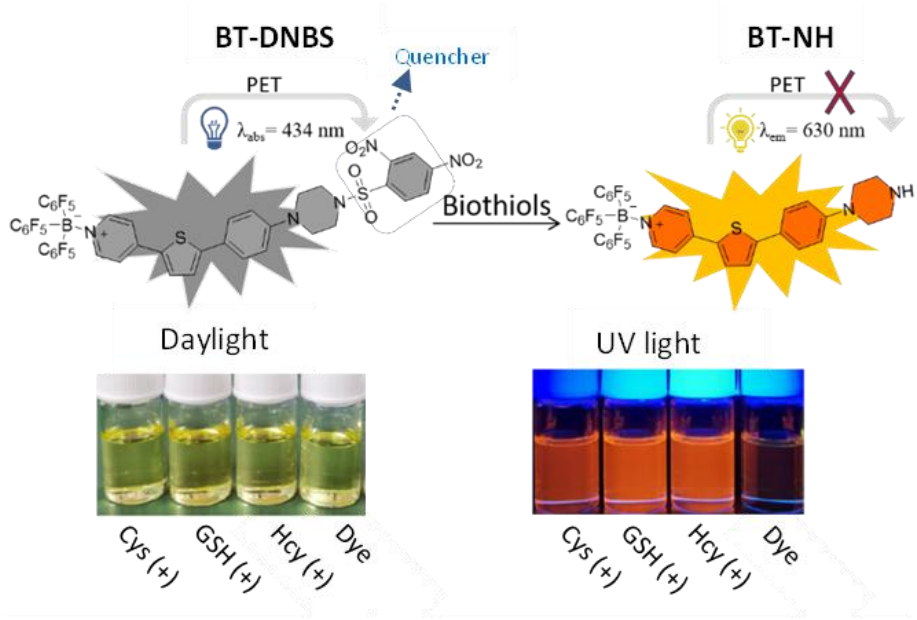


Fig 2.5 Structure of **BT-DNBS** and proposed sensing mechanism.

Moreover, the fluorescence intensity of **BT-DNBS** demonstrated a highly sensitive and dynamic response to biothiols, increasing up to 40-fold in the presence of Cys and Hcy (100 μM), 80-fold for GSH (100 μM), and notably reaching up to 140-fold for 1 mM GSH. This significant fluorescence enhancement underscores the probe's exceptional sensitivity to biothiols, particularly GSH. A plausible explanation for the stronger fluorescence response to GSH compared to Cys and Hcy lies in the reaction mechanism involving the DNBS group. It is hypothesized that GSH forms a transient intermediate through the formation of an S-C bond with the DNBS group. The larger and more flexible structure of GSH, compared to Cys and Hcy, likely facilitates effective intramolecular hydrogen bonding within the intermediate. This hydrogen bonding plays a crucial role in stabilizing the intermediate, thereby promoting efficient hydrogen transfer. Consequently, this process accelerates the cleavage of the sulfonate group, releasing the fluorescent moiety more readily and resulting in a more pronounced fluorescence enhancement.

Additionally, concentration titration experiments performed with **BT-DNBS** revealed its strong potential for sensitive and selective biothiol detection. When biothiol

concentrations were varied from 0 to 1000 μM, good linear relationships (0-30 μM) were observed (Fig. 2.6), demonstrating the probe's reliability in quantitative applications. In the lower concentration range (0–30 μM), the calculated limits of detection (LOD) were 83 nM for GSH, 49 nM for Cys, and 80 nM for Hcy, underscoring the probe's exceptional sensitivity, even at nanomolar levels. These results highlight **BT-DNBS** as a highly effective tool for detecting biothiols with precision.

Table 2.2 Spectroscopic data of BT-DNBS and BT-NH in DMSO: PBS =9:1, v/v, pH 7.4.

Dye	λ_{abs}[a]/nm	λ_{ex}[b]/nm	λ_{em}[c]/m	ε[e]/$M^{-1}cm^{-1}$	Stokes shift/cm^{-1}
BT-DNBS	434	434	630	3.5×10^4	7.14×10^3
BT-NH	436	440	630	2.4×10^4	7.06×10^3

a: absorption maximum. b: excitation wavelength. c: fluorescence emission maximum. e: molar extinction coefficient.

The photophysical properties of **BT-DNBS** (Table 2.2) further enhance its utility. It exhibits a maximum absorption wavelength at 434 nm and a maximum emission wavelength at 630 nm, resulting in a remarkable Stokes shift of 196 nm. This large Stokes shift minimizes spectral overlap between excitation and emission, thereby reducing background interference and improving detection accuracy.

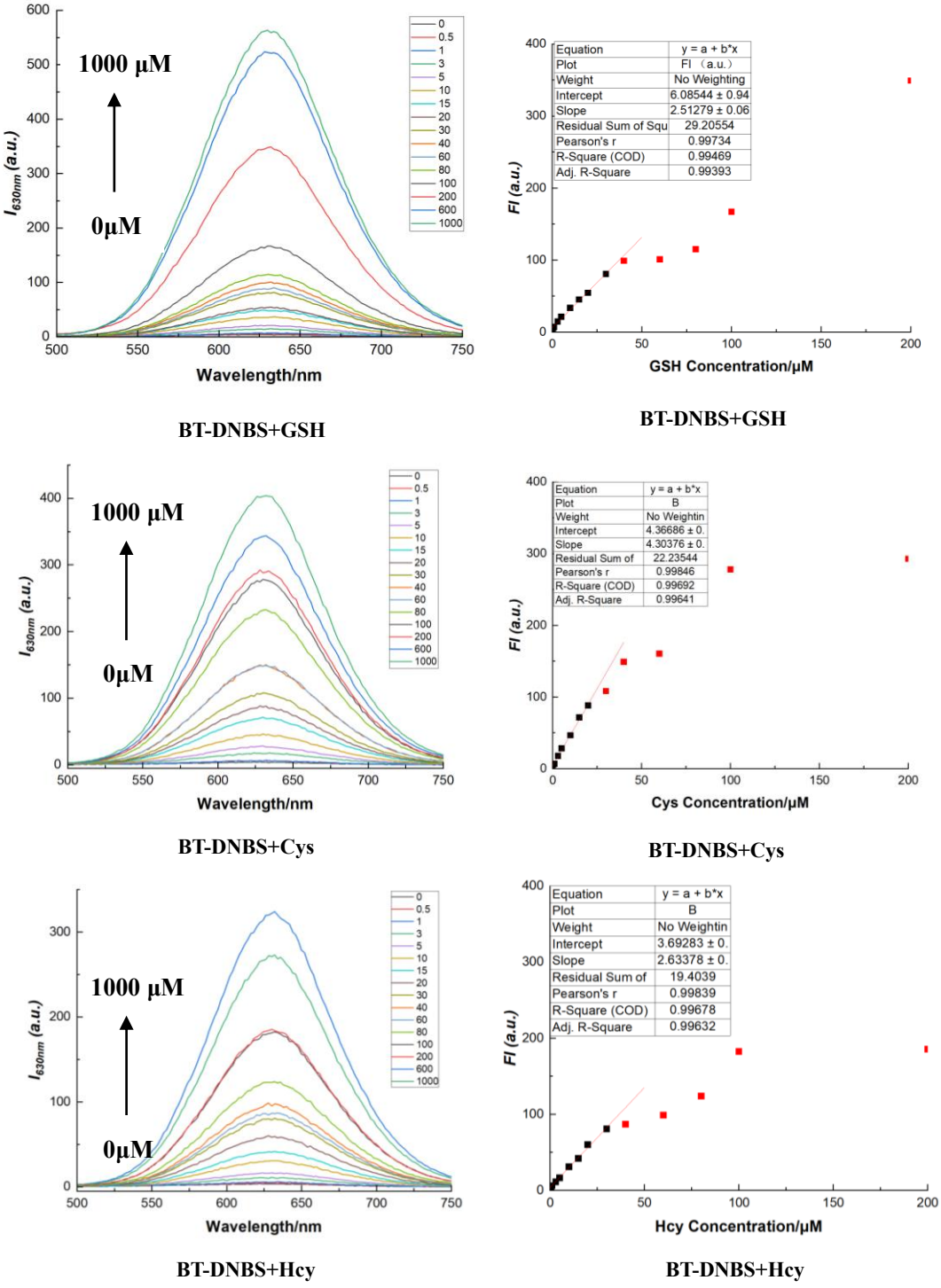


Fig. 2.6 (Left) Fluorescence intensity changes of **BT-DNBS** (10 μM, DMSO/PBS=9/1, v/v) upon addition of different concentrations of GSH/Cys/Hcy in PBS, (pH=7.4). (Right) Linear relationship between fluorescence intensity and analyte concentrations at 630 nm. Incubated for 20 min, r. t., λ_{ex}=434 nm, λ_{em}=630 nm. R^2=0.99469 (GSH), 0.99692 (Cys), 0.99678 (Hcy). LOD=83 nM (GSH), 49 nM (Cys), 80 (Hcy).

2.7 Selectivity analysis of BT-DNBS towards analytes

To validate the sensitivity and specificity of **BT-DNBS** in identifying biothiols, a comprehensive range of analytes was employed for fluorescence analysis. As illustrated in Fig. 2.7, the fluorescence intensity of **BT-DNBS** remained relatively unchanged upon the addition of various potential interferents, including amino acids (Arg, Gly, His, Leu, Met, Phe, Pro, Ser, Thr), anions (Cl^-, Br^-, NO_2^-, HCO_3^-, SO_3^{2-}, SO_4^{2-}), and metal ions (Ca^{2+}, Fe^{2+}, Mg^{2+}, Na^+), as well as reducing agents like ascorbic acid (Vc). This negligible fluorescence response across diverse analytes demonstrated the high stability of **BT-DNBS** in the presence of non-thiol-containing substances. In contrast, a pronounced fluorescence turn-on response was observed exclusively in the presence of biothiols, such as Cys, Hcy, and GSH, underscoring the probe's strong sensing

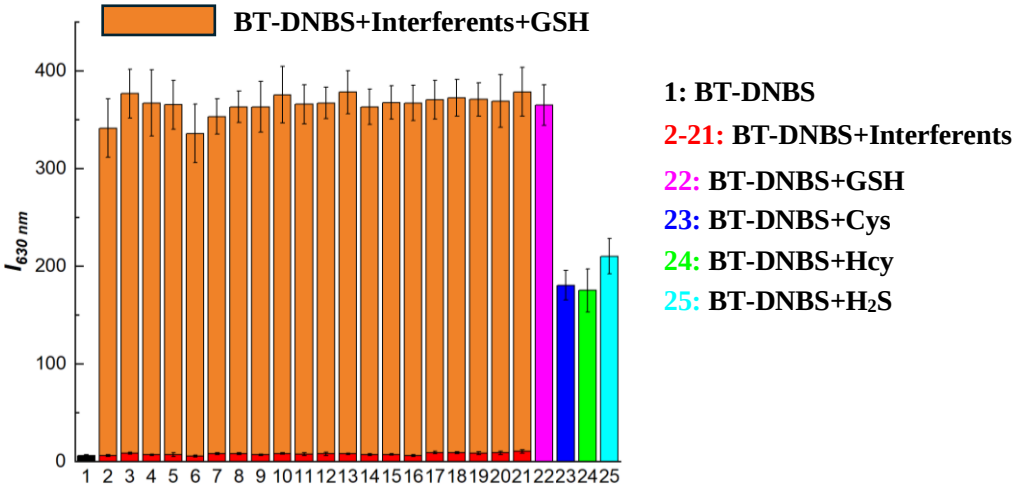


Fig. 2.7 Analysis of fluorescence intensity response of **BT-DNBS** to different analytes. **BT-DNBS** (10 μM) in DMSO/PBS (9:1, v/v, pH 7.4) in the presence of various analytes (100 μM). Incubated for 20 min, λ_{ex}=434 nm, λ_{em}=630 nm. 1: **BT-DNBS** (control); analytes included 2-21: Arg, Gly, His, Leu, Lys, Met, Phe, Pro, Ser, Thr, Cl^-, Br^-, NO_2^-, HCO_3^-, SO_3^{2-}, SO_4^{2-}, Ca^{2+}, Fe^{2+}, Mg^{2+}, Vc; 22-25, GSH, Cys, Hcy, H_2S.
Orange bar: fluorescence response measured by first adding interfering species 2-21, followed by the addition of GSH.

capabilities for these targets. The high selectivity of **BT-DNBS** for biothiols is attributed to the specific nucleophilic reaction between the DNBS moiety and thiol groups, which facilitates cleavage of the DNBS group and activates fluorescence. Additionally, the probe showed significant fluorescence activation in response to H_2S, with intensity levels comparable to those observed for Cys and Hcy. This response is likely due to the nucleophilic properties of H_2S, which enable interaction with the DNBS moiety, leading to a similar fluorescence activation mechanism.

The lack of significant interference from other biological and chemical analytes highlights the exceptional specificity of **BT-DNBS** for biothiols. This selectivity, coupled with its sensitivity, confirms the probe's potential for reliable biothiol detection even in complex biological matrices.

2.8 Time and pH-dependent spectra analysis

To evaluate the temporal and pH response of **BT-DNBS** towards biothiols, we conducted a time- and pH-dependent fluorescence intensity analysis. This analysis aimed to determine the kinetics, sensitivity, and pH stability of **BT-DNBS** when exposed to different biothiols over time and across various pH levels. The fluorescence intensity was monitored at regular intervals to observe the dynamic interaction between BT-DNBS and the target biothiols (GSH, Cys, and Hcy). As depicted in Fig. 2.8 (a), the

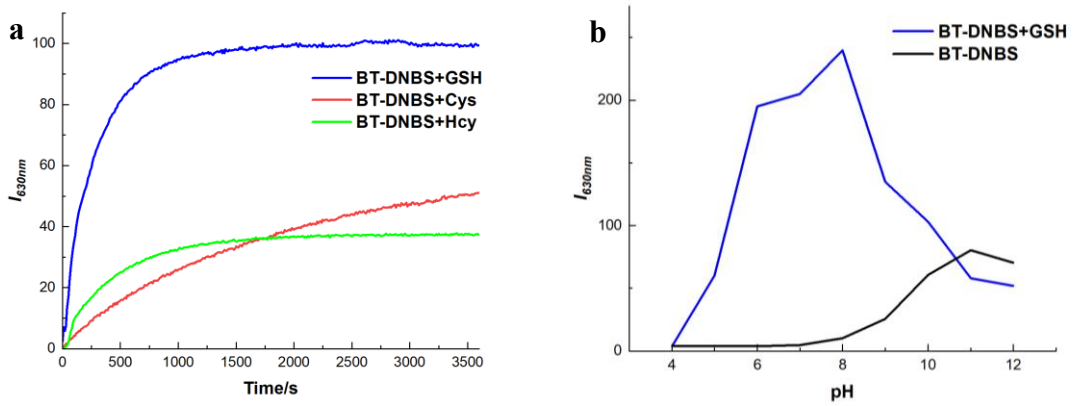


Fig. 2.8 Analysis of response time and pH stability of **BT-DNBS** towards biothiols. **a**): time-dependent fluorescence intensity response of **BT-DNBS** (10 μM, DMSO/PBS = 9:1, v/v, pH 7.4) in the presence of biothiols (100 μM), GSH (blue), Cys (red), and Hcy (green). λ_{ex}=434 nm, λ_{em}=630 nm. **b**): pH-dependent fluorescence intensity response of **BT-DNBS** (10 μM, DMSO/PBS=9:1, v/v) from pH 4 to 12 without analytes (black) and in the presence of GSH (100 μM, blue). Incubated for 20 min, λ_{ex}=434 nm, λ_{em}=630 nm.

fluorescence intensity exhibited a rapid increase within the initial 500 s, reaching near-maximum intensity at approximately 1200 s for GSH and Hcy. Subsequently, the fluorescence intensity stabilized for the remaining 1-hour observation period. This swift and consistent response suggests that **BT-DNBS** possesses high efficiency in detecting biothiols, rendering it advantageous for real-time monitoring applications. Furthermore, it is noteworthy that the response time of **BT-DNBS** is shorter compared to many biothiol-targeted fluorogenic probes [2-4].

The fluorescence intensity changes of **BT-DNBS** in response to pH variation were investigated across a range from pH 4 to pH 12, as shown in Fig. 2.8 (b). Notably, when **BT-DNBS** was tested without biothiols, it exhibited stable weak fluorescence intensity between pH 6 and 8. This stability suggests that **BT-DNBS** remained in a fluorescence-off state under these pH conditions. However, in the presence of GSH, a significant fluorescence-on state was observed within the same pH range of 6 to 8. This indicates that the addition of GSH induced a notable increase in fluorescence intensity, demonstrating the effective response of **BT-DNBS** to biothiols under physiological pH conditions. However, as the pH increases beyond 8, OH^- probably facilitate the nucleophilic cleavage of the DNBS group, breaking the S–N bond and releasing the fluorophore. This might eliminate the PET quenching effect, leading to fluorescence activation. In contrast, at pH 6–8, the DNBS group remains intact, keeping the fluorophore in a fluorescence-off state. Nevertheless, this behavior is not significant under physiological pH conditions, where **BT-DNBS** exhibits stable and efficient fluorescence response, making it ideal for biothiol detection in biological systems.

2.9 Sensing mechanism

Previous studies have demonstrated that probes incorporating DNBS group as a recognition site undergo nucleophilic aromatic substitution reactions with biothiols [5, 6]. This reaction mechanism involves the removal of the DNBS group, which suppresses the photo-induced electron transfer (PET), restoring the inherent fluorescence of **BT-NH**. In the context of **BT-DNBS**, upon interaction with biothiols such as GSH, Cys, and Hcy, the DNBS group, initially acting as a fluorescence quencher by the intramolecular PET, is cleaved, thereby resulting in a pronounced fluorescence enhancement. To validate the sensing mechanism, **BT-DNBS** and isolated product **BT-NH** were analyzed using ^{1}H NMR and ESI-Mass spectrometry, as depicted in Fig. 2.9. The ^{1}H NMR spectra of the isolated reaction product **BT-NH** showed the disappearance of peaks corresponding to the cleaved DNBS group. Additionally, ESI-Mass spectrometry confirmed the presence of a new peak corresponding to **BT-NH**. These findings provide compelling evidence for the nucleophilic substitution reaction and the subsequent formation of the fluorescent **BT-NH** product, corroborating the proposed mechanism.

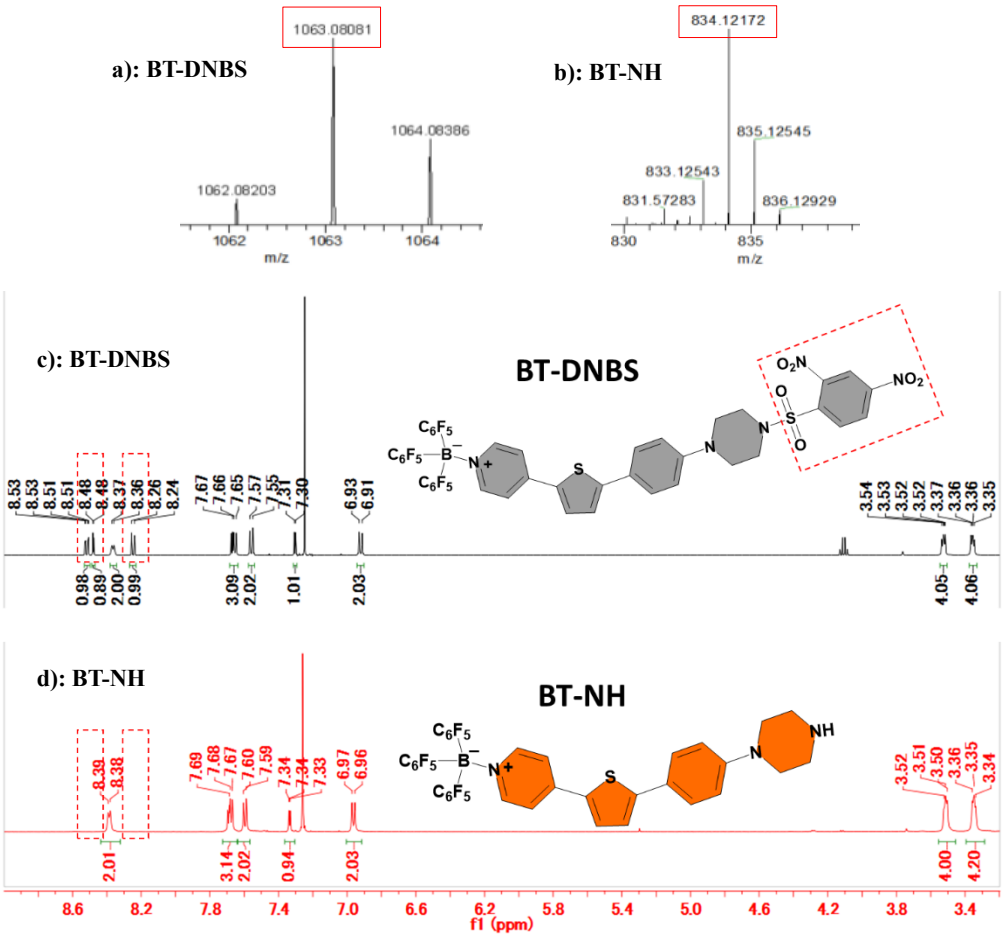


Fig. 2.9 ^{1}H NMR and ESI-Mass spectra confirming the proposed sensing mechanism of **BT-DNBS.** a): ESI-Mass spectrum of **BT-DNBS**. $[M]^{+}$ calculated: 1063.0787; found: 1063.0808. b): ESI-Mass spectrum of isolated **BT-NH** after **BT-DNBS** reacted with GSH. $[M+H]^{+}$ calculated: 834.1220; found: 834.1217. c): ^{1}H NMR spectrum of **BT-DNBS**. d): ^{1}H NMR spectrum of isolated **BT-NH** after **BT-DNBS** reacted with GSH.

2.10 Density functional theory (DFT) calculation

To better understand the fluorescence turn-on mechanism of **BT-DNBS** from the perspective of frontier molecular orbitals, detailed DFT calculations and structural optimizations were performed on **Cl-DNBS**, **BT-NH**, and **BT-DNBS**. These calculations were conducted using the B3LYP functional and the 6-311G(d,p) basis set, as implemented in the Gaussian 09 program. The computational analysis aimed to elucidate the electronic interactions responsible for fluorescence quenching and activation, providing insights into the molecular basis of **BT-DNBS**'s biothiol-responsive behavior.

As illustrated in Fig. 2.10, the results reveal a significant energy alignment between the molecular orbitals of the involved components. Specifically, the LUMO (Lowest Unoccupied Molecular Orbital) energy level of **Cl-DNBS** is calculated to be -4.21 eV, which lies between the HOMO (-5.86 eV) and LUMO (-2.99 eV) energy levels of **BT-NH**. This energy configuration indicates that a PET (photoinduced electron transfer) process from the excited state of **BT-NH** to **Cl-DNBS** is thermodynamically favorable. Such PET activity efficiently quenches the fluorescence moiety in **BT-DNBS**, keeping the probe in a "fluorescence-off" state under normal conditions. Upon interaction with biothiols, the N-S bond between the piperazine unit and the DNBS moiety is cleaved, disrupting the PET pathway. This cleavage eliminates the quenching effect of DNBS, thereby restoring the intrinsic fluorescence of the **BT-NH** structure. This mechanistic insight highlights the role of biothiol-mediated cleavage in enabling the fluorescence turn-on behavior of **BT-DNBS**, making it an effective and selective probe for biothiols.

Furthermore, a closer examination of the frontier molecular orbital distributions provides additional support for the proposed mechanism. For **BT-NH**, the π-electrons are distributed relatively evenly across the HOMO and LUMO orbitals, indicating that the energy transitions involve the entire dye structure. In contrast, for **BT-DNBS**, the orbital distributions exhibit clear segregation: the π-electrons in the HOMO are primarily localized on the fluorescence moiety of**,** whereas those in the LUMO are

predominantly distributed on the DNBS moiety. This separation confirms that the DNBS group acts as a strong electron acceptor, facilitating the PET process from the fluorescence moiety to the DNBS moiety, which quenches fluorescence.

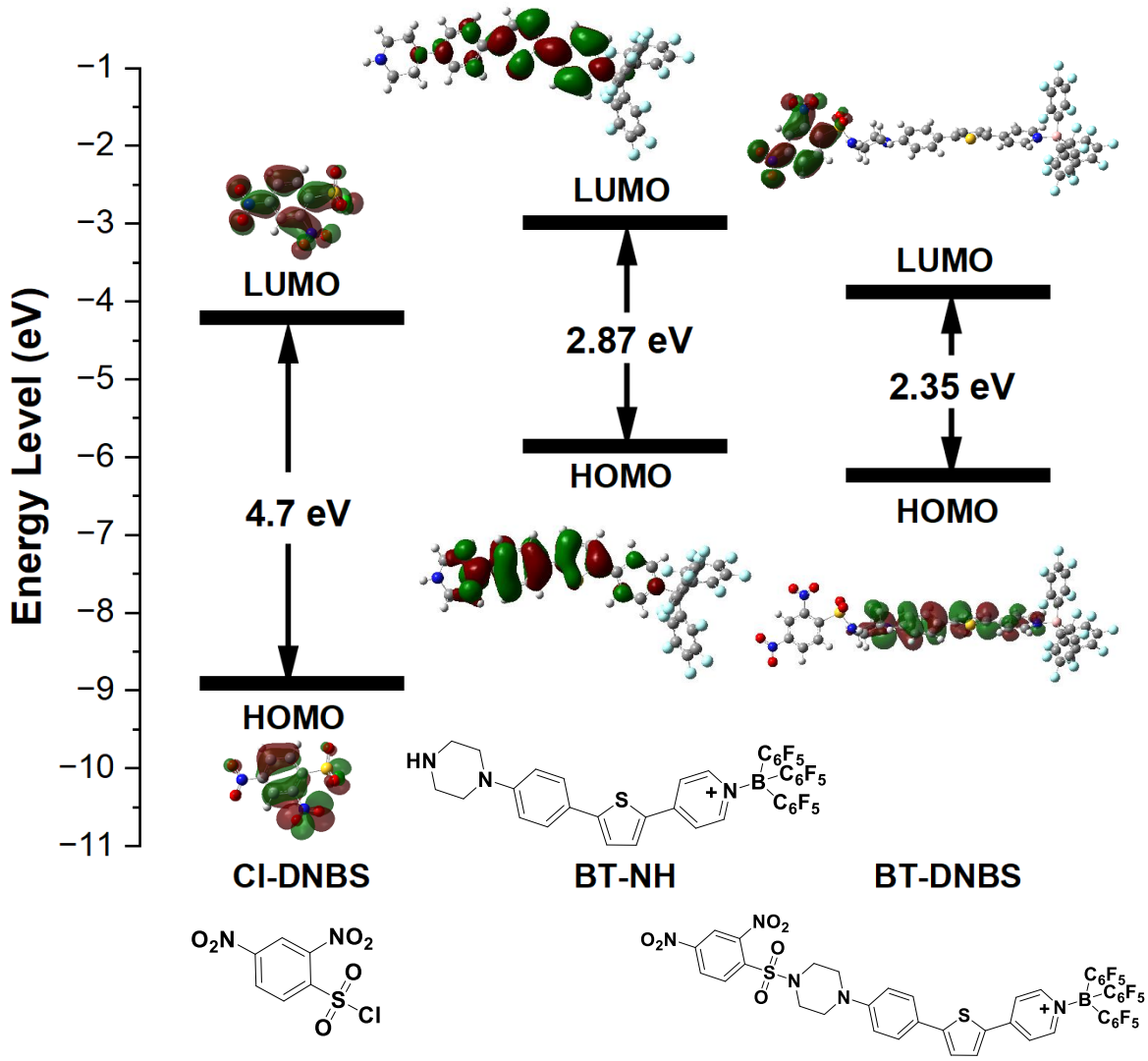


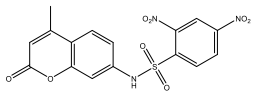
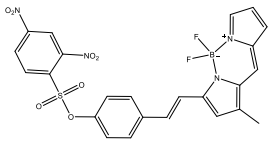
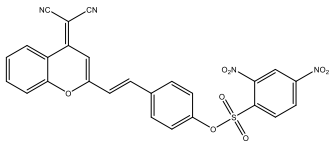
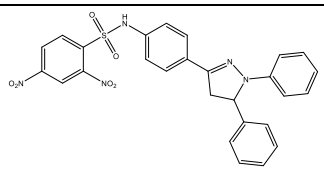
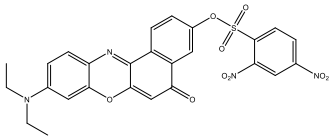
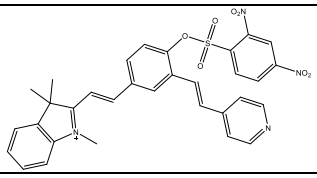
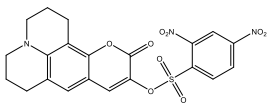
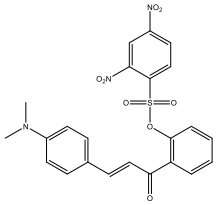
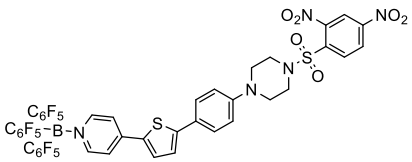
Fig. 2.10 Density Functional Theory (DFT) optimized structures and frontier molecular orbitals (MOs) of **Cl-DNBS**, **BT-NH**, and **BT-DNBS**. Calculations were performed based on ground state geometries using the B3LYP functional and the 6-311G(d,p) basis set with the Gaussian 09W program.

These computational findings strongly corroborate the proposed sensing mechanism of **BT-DNBS**. The cleavage of the DNBS group interrupts the PET process, allowing the fluorescent **BT-NH** to dominate, thereby enabling a clear and measurable fluorescence response. Such theoretical insights into the electronic structure and orbital dynamics provide a robust framework for understanding the fluorescence activation mechanism of **BT-DNBS**, paving the way for its application in biothiol detection in complex biological environments.

2.11 Reported Probes with a DNBS Group

A comparative analysis (Table 2.3) was performed to evaluate BT-DNBS against other reported fluorescent probes containing DNBS groups. The results demonstrate that BT-DNBS exhibits a significantly larger Stokes shift (196 nm) and lower detection limits (83 nM for GSH, 49 nM for Cys, and 80 nM for Hcy) compared to previously reported probes. These advantages enhance its sensitivity and reliability for detecting biothiols in complex biological environments, making it a promising tool for studying biothiol-related biological processes, such as oxidative stress and redox signaling.

Table 2.3, Reported Fluorescent Probes with a DNBS Group in Literature.

Ref	Probe	$\lambda_{ex}/\lambda_{em}$ (nm)	Stokes shift (nm)	Response time to biothiol	LOD
7		353/450	97	2 h	—
8		527/570	43	＞1 min	—
9		560/690	130	5 min	18 μM
10		370/464	94	12 h	411 nM
11		567/645	78	＞15 min	107 nM
12		545/604	59	8 min	134 nM
13		395/517	122	24 min	14.5 nm
14		460/600	140	15 min	227 nm
15		**434/630**	**196**	**20 min**	**83 nm**

2.12 Conclusion

In this chapter, the synthesis, characterization, and photophysical properties of **BT-DNBS** and its precursor compounds were systematically explored. The results revealed that the incorporation of the DNBS group into the fluorescent dye framework effectively quenched fluorescence through a photoinduced electron transfer (PET) mechanism. Upon interaction with biothiols, the DNBS group was cleaved, leading to a pronounced turn-on fluorescence response. Comprehensive spectroscopic analyses demonstrated the probe's excellent sensitivity and selectivity toward biothiols, with minimal interference from other biological analytes. Optimization of spectroscopic testing conditions, including solvent composition and pH, further highlighted the robustness of **BT-DNBS** under physiological conditions, making it suitable for biological applications. Additionally, time- and pH-dependent studies confirmed the stability and rapid response of the probe in detecting biothiols. Finally, density functional theory (DFT) calculations provided deeper insights into the PET mechanism, showing that the DNBS group acted as an efficient electron acceptor, which quenched fluorescence until its cleavage restored the electronic configuration of the fluorescence moiety.

Overall, the findings presented in this chapter establish the design principles and functionality of **BT-DNBS** as a versatile fluorescent probe for biothiol detection, laying a solid foundation for its application in live-cell imaging and other bioanalytical contexts.

References

1. Liu Z, Fang Q, Wang D, et al. Trivalent Boron as an Acceptor in Donor–π–Acceptor-Type Compounds for Single-and Two-Photon Excited Fluorescence. *Chemistry–A European Journal,* **2003**, 9(20): 5074-5084. DOI: 10.1002/chem.200304833.
2. Dai F, Zhao M, Yang F, et al. An ESIPT coupled AIE fluorescent probe for biothiols detection and imaging based on a chalcone fluorophore. *Dyes and Pigments*, **2020**, 183: 108627. DOI: 10.1016/j.dyepig.2020.108627.
3. Gao B, Cui L, Pan Y, et al. A highly selective ratiometric fluorescent probe for biothiol and imaging in live cells. *RSC advances*, **2016**, 6(49): 43028-43033. DOI: 10.1039/C6RA04564B.
4. Wang S Q, Wu Q H, Wang H Y, et al. A novel pyrazoline-based selective fluorescent probe for detecting reduced glutathione and its application in living cells and serum. *Analyst*, **2013**, 138(23): 7169-7174. DOI: 10.1039/C3AN01440A.
5. Wei M, Yin P, Shen Y, et al. A new turn-on fluorescent probe for selective detection of glutathione and cysteine in living cells. *Chemical communications*, **2013**, 49(41): 4640-4642. DOI: 10.1039/C3CC39045D.
6. Yang L, Su Y, Geng Y, et al. An instantaneous near-infrared trimethyl lock based fluorescent probe for biothiols with a large Stokes shift. *Analytica Chimica Acta*, **2018**, 1034: 168-175. DOI: 10.1016/j.aca.2018.06.011.
7. Lu G, Ding S, Meng S, et al. A near-infrared turn on fluorescent probe for specific detection of cysteine and its application based on a corrole fluorophore. *Dyes and Pigments*, **2024**, 227: 112194. DOI: 10.1016/j.dyepig.2024.112194.
8. Wei M, Yin P, Shen Y, et al. A new turn-on fluorescent probe for selective detection of glutathione and cysteine in living cells. *Chemical communications*, **2013**, 49(41): 4640-4642. DOI: 10.1039/C3CC39045D.
9. Li X, Qian S, He Q, et al. Design and synthesis of a highly selective fluorescent turn-on probe for thiol bioimaging in living cell. *Organic & biomolecular chemistry*, **2010**, 8(16): 3627-3630. DOI: 10.1039/C004344C.

10. Li M, Wu X, Wang Y, et al. A near-infrared colorimetric fluorescent chemodosimeter for the detection of glutathione in living cells. *Chemical Communications*, **2014**, 50(14): 1751-1753. DOI: 10.1039/C3CC48128J.
11. Wang S Q, Wu Q H, Wang H Y, et al. A novel pyrazoline-based selective fluorescent probe for detecting reduced glutathione and its application in living cells and serum. *Analyst*, **2013**, 138(23): 7169-7174. DOI: 10.1039/C3AN01440A.
12. Rong X, Xu Z Y, Yan J W, et al. Nile-red-based fluorescence probe for selective detection of biothiols, computational study, and application in cell imaging. *Molecules*, **2020**, 25(20): 4718. DOI: 10.3390/molecules25204718.
13. Zhu Y, Pan H, Song Y, et al. Mitochondria-targeted fluorescent probe for rapid detection of thiols and its application in bioimaging. *Dyes and Pigments*, **2021**, 191: 109376. DOI: 10.1016/j.dyepig.2021.109376.
14. Wang X B, Zhang D. A novel reaction-based fluorescent turn-on probe for biothiols and its application in cell imaging. *Sensors and Actuators B: Chemical*, **2017**, 241: 327-334. DOI: 10.1016/j.snb.2016.10.046.
15. Zhang S, Fujioka Y, Ohba Y, et al. BT-DNBS: a novel cyanine-based turn-on fluorescent probe with large Stokes shift for sensitive and selective detection of biothiols in live-cell imaging. *RSC advances*, **2025**, 15(1): 135-141. DOI: 10.1039/D4RA07109C.

Chapter 3. Cell Imaging

Abstract

This chapter focuses on the application of BT-DNBS in cell imaging, covering cell culture, toxicity testing, and intracellular biothiol detection. The toxicity assays confirmed that BT-DNBS exhibits no significant toxicity at lower concentrations, making it suitable for live-cell imaging. The fluorescence intensity of intracellular biothiols showed a time-dependent increase, with the fluorescence strengthening over time. Comparative experiments using NEM to deplete cellular thiols demonstrated that BT-DNBS specifically responds to biothiols, validating its high selectivity for thiol detection. The results presented in this chapter provide strong evidence for the use of BT-DNBS in intracellular biothiol imaging and highlight its potential applications in biological research.

3.1 Introduction

Fluorescence imaging has emerged as a powerful tool in cellular biology, enabling researchers to visualize and quantify biomolecules with high sensitivity and spatial resolution [1,2]. Among these, the detection of biothiols such as glutathione (GSH), cysteine (Cys), and homocysteine (Hcy) within live cells is of particular significance due to their essential roles in maintaining cellular redox balance, signal transduction, and detoxification [3-5]. Aberrant biothiol levels are associated with various pathological conditions, including cancer, neurodegenerative diseases, and cardiovascular disorders [6,7]. Therefore, the development of robust fluorescent probes for biothiol detection is critical for advancing biological research and diagnostic applications.

BT-DNBS, a newly synthesized turn-on fluorescent probe, offers distinct advantages for intracellular biothiol detection. Its donor-acceptor (D-π-A) design, coupled with the DNBS quenching group, allows for a photoinduced electron transfer (PET)-based fluorescence "off-on" mechanism. Upon reaction with biothiols, the DNBS group is cleaved, restoring the fluorescence of the probe and enabling precise visualization of biothiols within live cells. The large Stokes shift, high selectivity, and

low cytotoxicity of **BT-DNBS** make it a promising candidate for live-cell imaging applications.

This chapter focuses on evaluating the performance of **BT-DNBS** in a cellular context. Key aspects investigated include its fluorescence response to biothiols in live cells, specificity towards biothiol-containing analytes, the effect of pre-treatment with thiol-blocking agents, and its cytotoxicity profile. Through a combination of fluorescence imaging and quantitative analyses, we aim to establish the utility of **BT-DNBS** as a reliable probe for intracellular biothiol detection, highlighting its potential for monitoring of biothiol fluctuations in physiological and pathological conditions.

3.2 Instruments and Methods

Cell images were acquired with IX83 microscope (Olympus, Tokyo, Japan) equipped with a BioPoint MAC 6000 filter and shutter control unit (Ludl Electronic Products, Hawthorne, NY, USA), an automated XY-stage (Applied Scientific Instrumentation, Eugene, OR, USA), a UPlanSApo 60/1.35 oil objective lens, an LDI laser light source (Chroma Technology Corp., Bellows Falls, VT, USA), and an X-Light V3 (CrestOptics, Rome, Italy) spinning-disk confocal unit. The detector used in this study was an EM-C2 electron-multiplying (EM) cooled charge-coupled device (CCD) camera iXon Ultra 888 (Oxford Instruments, Abingdon-on-Thames, UK). The excitation and emission filters adopted for this study included ZET 445/520 and ET 600/50m (Chroma Technology Corp., Bellows Falls, VT, USA). A ZT445/520 dichroic mirror (Chroma Technology Corp.) was used throughout this study. Optical density of cytotoxicity assay was measured by a BIO-RAD Benchmark Microplate Reader.

3.2.1 Cell culture

A431 cells were cultured in DMEM supplemented with 10% fetal bovine serum (FBS), 100 U/mL penicillin, and 100 μg/mL streptomycin. The cells were maintained in a humidified atmosphere with 5% CO_2 at 37°C. For imaging experiments, cells were seeded on glass-bottom dishes and cultured until reaching approximately 70-80% confluency.

3.2.2 Cell viability assay

Cell Viability Assay of **BT-DNBS** was assessed using the Cell Counting Kit-8 (CCK-8) assay on A431 cells. Cells were seeded in a 96-well plate at a density of 1×10^4 cells per well and allowed to adhere overnight. Subsequently, the cells were treated with fresh medium containing varying concentrations of **BT-DNBS** (0, 1, 10, 100 μM) and incubated for 24 hours at 37°C in a humidified atmosphere with 5% CO_2. Following the incubation period, 10 μL of CCK-8 solution was added to each well, and the plate was incubated for an additional hour. Absorbance at 450 nm was measured using a microplate reader to determine cell viability. Cell viability was calculated as a percentage relative to the untreated control cells using the following formula:

$$Cell\ Viability(\%) = \left(\frac{Absorbance\ of\ treated\ cells - Absorbance\ of\ blank}{Absorbance\ of\ control\ cells - Absorbance\ of\ blank}\right) \times 100$$

3.2.3 Fluorescent probe treatment

BT-DNBS was dissolved in dimethyl sulfoxide (DMSO) to prepare a 2 mM stock solution and diluted with culture medium to the desired concentration (10 μM) immediately before use. For fluorescence imaging, cells were treated with **BT-DNBS** at 10 μM for various durations (60, 120, 240 minutes) at 37°C. After incubation, cells were washed three times with PBS to remove excess dye and observed using fluorescence microscope.

3.2.4 Fluorescence Imaging

A431 cells were cultured in DMEM with 10% FBS at 37°C and seeded onto glass-bottom dishes for imaging. The cells were then incubated with BT-DNBS (10 μM), Hoechst 33342 (5 μM, Thermo Fisher Scientific), and Lipi-Deep Red (1 μM, Dojindo, Japan) for 60 minutes, followed by three washes with PBS. Fluorescence imaging was performed using a confocal microscope (Olympus IX83+X-light V3) with the following filter settings: Hoechst 33342 (BP 350/50, BP 460/50, DAPI filter), Lipi-Deep Red (BP 620/60, BP 700/75, Cy5 filter), and BT-DNBS (BP 445/20, TRITC filter). Images were analyzed using imaging software Image J.

3.2.5 Thiol-blocking agent pre-treatment

To investigate the specificity of **BT-DNBS** for biothiols, cells were pre-treated with N-ethylmaleimide (NEM), a thiol-blocking reagent. A431 cells were incubated with 50 μM NEM in culture medium for 60 minutes at 37°C, followed by incubation with **BT-DNBS** (10 μM) for 120 minutes.

3.3 Results and Discussion

3.3.1 Cytotoxicity evaluation

The cytotoxicity of **BT-DNBS** was assessed to ensure its suitability for live-cell imaging applications. As shown in Fig. 3.1, **BT-DNBS** exhibited negligible cytotoxicity at concentrations of 1 μM and 10 μM, with cell viability exceeding 90%. Even after 24 hours of incubation, the cells maintained normal morphology and proliferation rates at these concentrations. However, at a higher concentration of 100 μM, a noticeable decrease in cell viability was observed, with viability dropping to approximately 50%. This suggests that excessive levels of **BT-DNBS** may induce stress or toxicity in cells, likely due to aggregation or interference with cellular processes. The low cytotoxicity of **BT-DNBS** at 10 μM, the concentration used for imaging experiments, highlights its biocompatibility and supports its potential as a fluorescent probe for live-cell imaging. These results also underline the importance of optimizing probe concentration to balance fluorescence performance and cytotoxicity, ensuring accurate and safe imaging of biothiol in live cells.

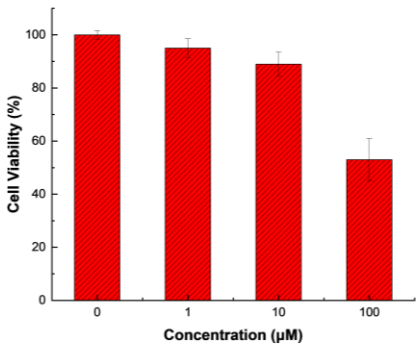


Fig. 3.1 Cell viability assay: A431 cells were treated with various concentrations of **BT-DNBS** (0, 1, 10, 100 μM) for 24 hours.

3.3.2 Fluorescence response in cells

Using A431 cells, the practical applicability of **BT-DNBS** for live-cell imaging was evaluated. Cells were incubated with BT-DNBS (10 μM) for varying durations (60, 120, and 240 minutes) at 37 °C in a humidified atmosphere with 5% CO_2, followed by fluorescence imaging with a spinning disk confocal microscope. As illustrated in Fig. 3.2(a), the untreated cells (control group) displayed negligible fluorescence, confirming the low inherent autofluorescence of the A431 cells under the imaging conditions. This low background fluorescence establishes a strong baseline for observing the fluorescence turn-on effect of **BT-DNBS**. In contrast, cells treated with **BT-DNBS** exhibited a clear, time-dependent increase in fluorescence intensity. After 60 minutes of incubation (Fig. 3.2(b)), only weak fluorescence was detected, indicating the initial stages of interaction between **BT-DNBS** and intracellular biothiols. As the incubation period was extended to 120 minutes (Fig. 3.2(c)), the fluorescence signal became notably stronger, reflecting the progressive cleavage of the DNBS group and subsequent fluorescence activation. By 240 minutes (Fig. 3.2(d)), the fluorescence intensity increased further, highlighting the efficiency of **BT-DNBS** in accumulating within the cells and reacting with biothiols over time. The observed trend suggests that **BT-DNBS** is well-suited for applications requiring prolonged incubation to achieve optimal fluorescence activation. Furthermore, the progressive increase in fluorescence intensity underscores the potential of B**T-DNBS** for imaging biothiol dynamics within live cells.

Fluorescence colocalization imaging was performed to evaluate the intracellular distribution of BT-DNBS in live A431 cells. As shown in Fig. 3.3, A431cells were incubated with Hoechst 33342 (5 μM) and BT-DNBS (10 μM) for 60 minutes, followed by fluorescence imaging. The Hoechst 33342 channel (Fig.3.3a) displays blue fluorescence, indicating nuclear staining, while the BT-DNBS channel (Fig3.3b) shows orange fluorescence corresponding to biothiol detection in the cytoplasm. The merged image (Fig. 3.3c) reveals distinct localization patterns of the two dyes, confirming that BT-DNBS primarily localizes in the cytoplasmic region rather than the nucleus.

Additionally, multichannel imaging was performed using Hoechst 33342, BT-DNBS, and Lipi-Deep Red, a lipid droplet marker (Fig. 3.4). The results showed that the fluorescence signals from the three channels did not overlap, indicating distinct subcellular localization of each probe. This demonstrates the capability of the imaging system to simultaneously distinguish different cellular components, highlighting the potential of BT-DNBS for selective biothiol detection in complex intracellular environments without interference from nuclear or lipid-associated fluorescence.

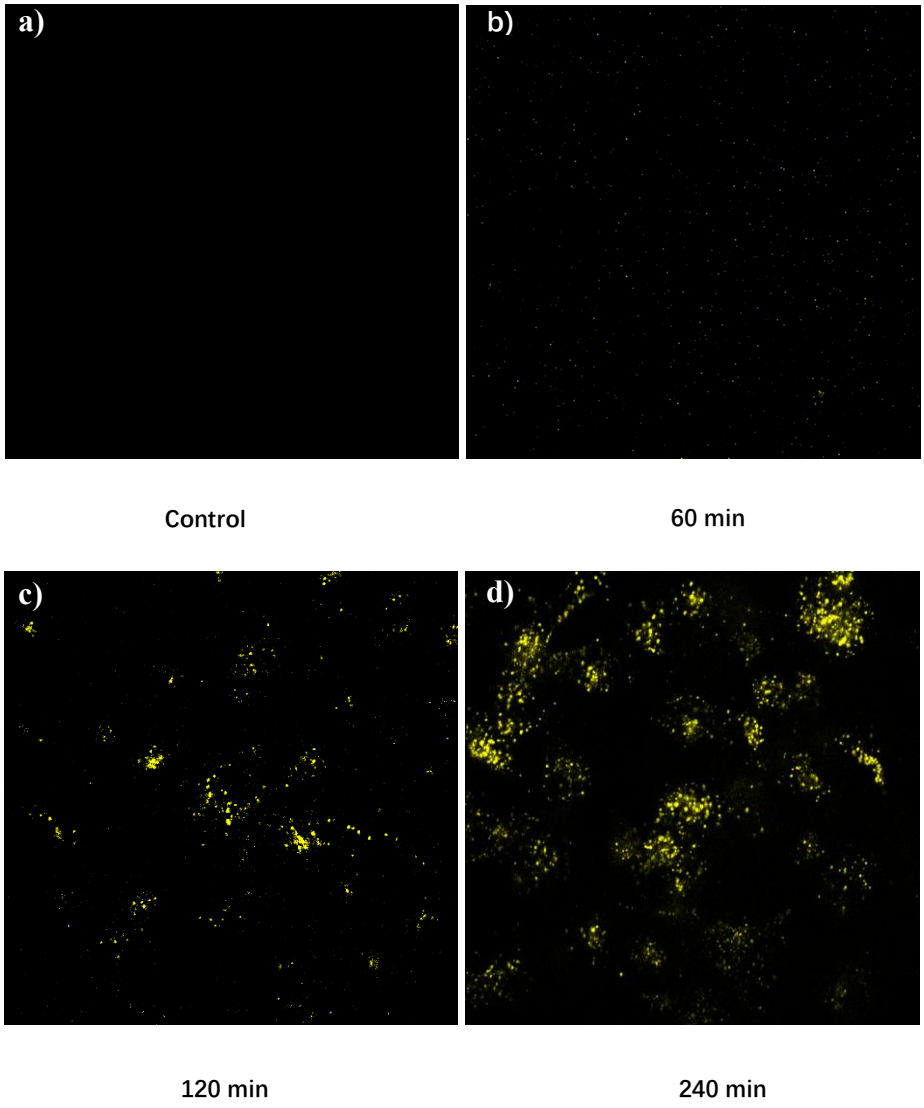


Fig. 3.2: Fluorescent images. a): control group, untreated A431 cells. b-d): cells incubated with **BT-DNBS** (10 μM) for 60 minutes (b), 120 minutes (c), 240 minutes (d). λ_{ex}=434 nm, λ_{em}=630 nm.

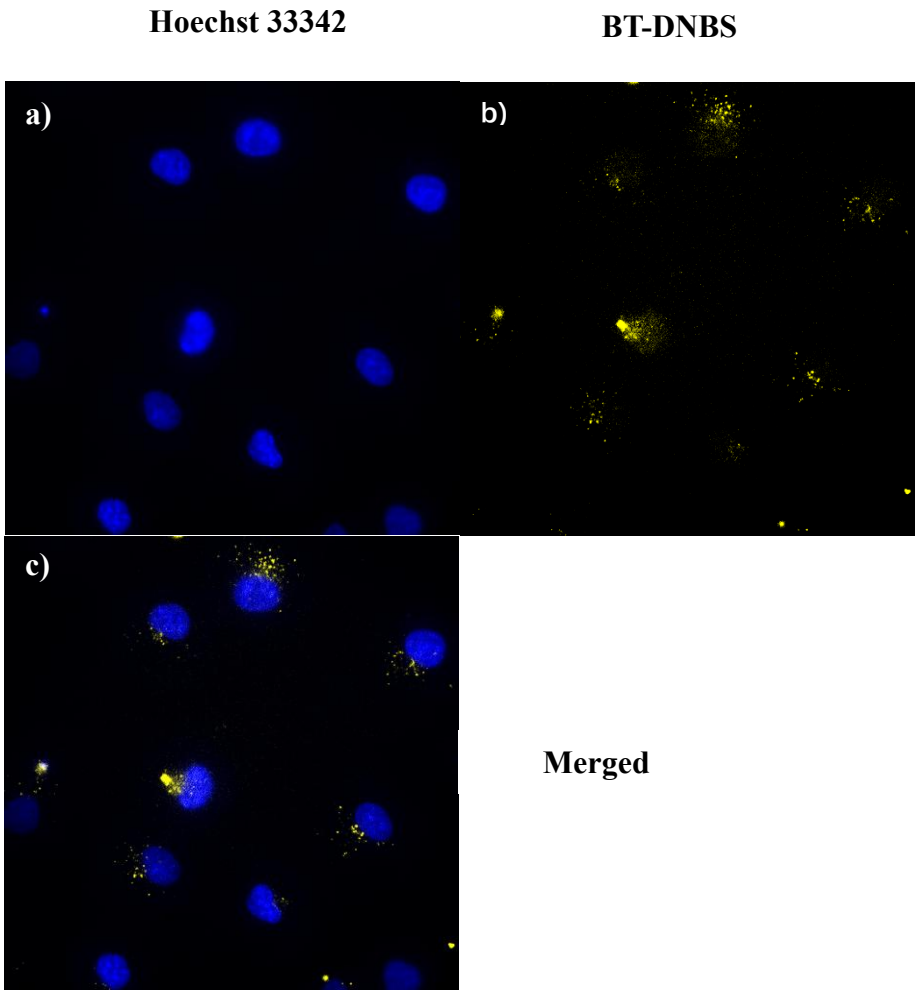


Fig. 3.3: Fluorescence colocalization images of Hoechst 33242 and BT-DNBS in live A431 cells. a): Hoechst 33342. b): BT-DNBS. c): merged image. Cells incubated with Hoechst 33342 (5 μM) and **BT-DNBS** (10 μM) for 60 minutes. λ_{ex}=434 nm, λ_{em}=630 nm.

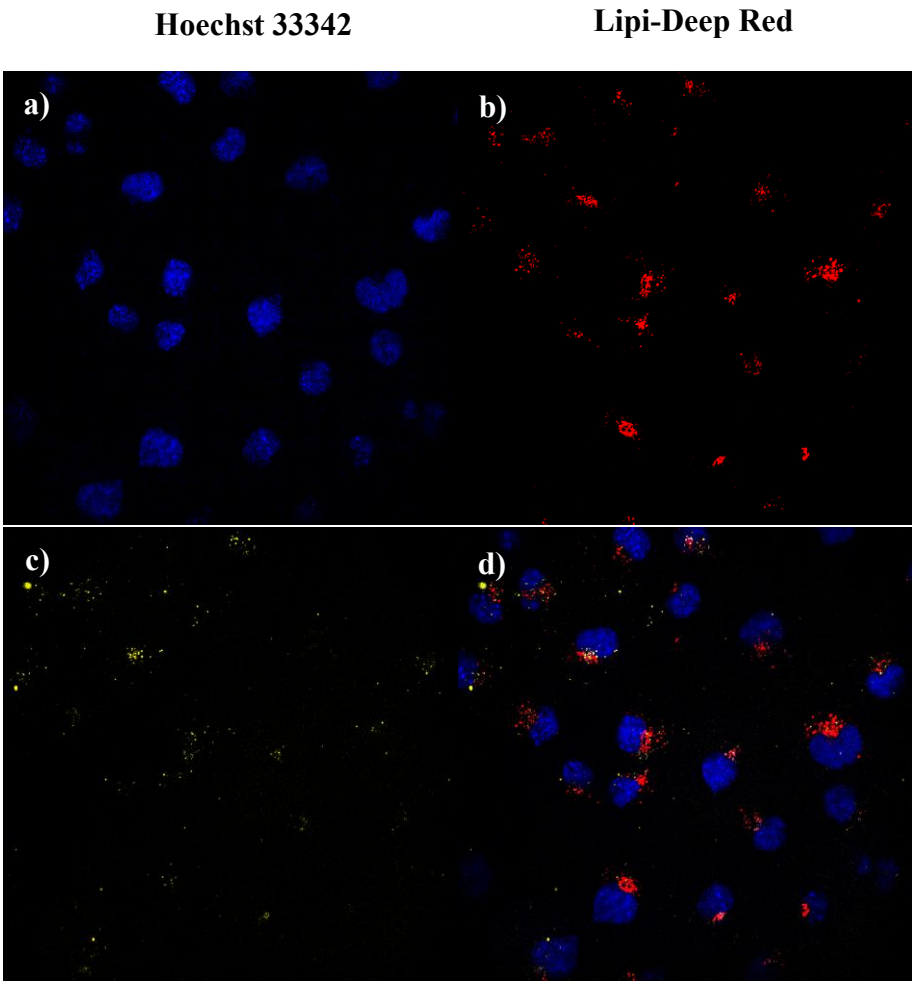


Fig. 3.4: Fluorescence colocalization images of Hoechst 33242, Lipi-Deep Red and BT-DNBS in live A431 cells. a): Hoechst 33342. b): Lipi-Deep Red. c): BT-DNBS. d): merged image. Cells incubated with Hoechst 33342 (5 μM), Lipi-Deep Red (1 μM) and **BT-DNBS** (10 μM) for 60 minutes. λ_{ex}=434 nm, λ_{em}=630 nm.

3.3.3 Effect of pre-treatment with NEM

To confirm the biothiol-specific fluorescence activation of **BT-DNBS**, A431 cells were pre-treated with N-ethylmaleimide (NEM), a thiol-blocking agent (Fig. 3.5) [8], at a concentration of 50 μM for 60 minutes. Following NEM pre-treatment, the cells were incubated with **BT-DNBS** (10 μM) for 120 minutes under identical conditions. As shown in Fig. 3.6(a), cells treated with NEM prior to **BT-DNBS** displayed significantly diminished fluorescence compared to cells treated with **BT-DNBS** alone (Fig. 3.6(b)). This suppression of fluorescence demonstrates that **BT-DNBS** activation is dependent on the presence of intracellular thiol-containing substances.

Control experiments without NEM pre-treatment resulted in a pronounced fluorescence signal, further confirming that the observed fluorescence arises from the interaction between **BT-DNBS** and biothiols. These results underscore the biothiol specificity of **BT-DNBS** and validate its potential as a reliable probe for live-cell biothiol imaging.

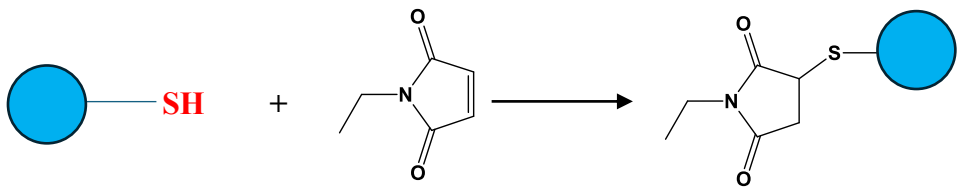
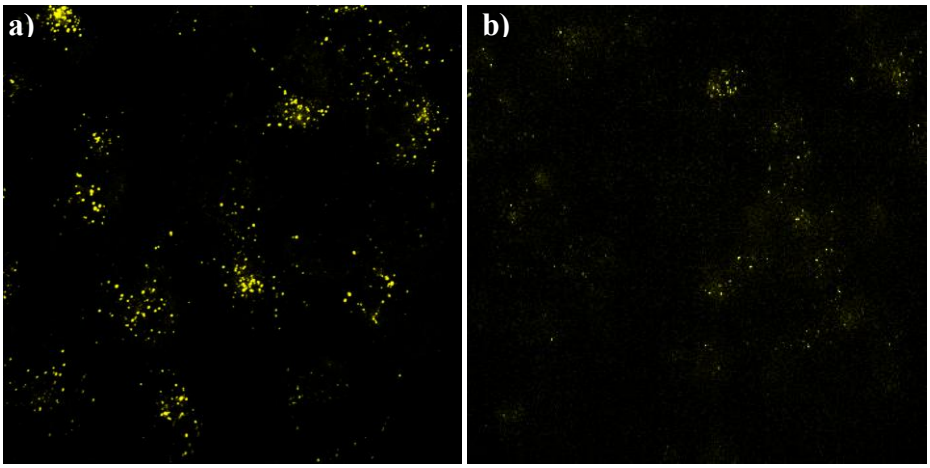


Fig. 3.5: Mechanism of NEM-mediated depletion of biothiols.



120 min, NEM (-), BT-DNBS (+)

120 min, NEM (+), BT-DNBS (+)

Fig. 3.6 Specificity analysis of biothiols. a): cells incubated with **BT-DNBS** (10 μM) for 120 minutes without NEM pre-treatment. b): cells were pre-treated with NEM (50 μM) for 60 minutes, followed by incubation with **BT-DNBS** (10 μM) for 120 minutes. λ_{ex}=434 nm, λ_{em}=630 nm.

3.4 Conclusion

In this chapter, the practical applicability of BT-DNBS for live-cell imaging was thoroughly evaluated using A431 cells. Cytotoxicity assessments confirmed that BT-DNBS exhibits low toxicity at the working concentration of 10 μM, ensuring its suitability for biological imaging applications. Fluorescence imaging experiments demonstrated a time-dependent fluorescence enhancement, indicating efficient intracellular accumulation and biothiol-specific activation of BT-DNBS. Additionally, multichannel imaging was conducted using Hoechst 33342, Lipi-Deep Red, and BT-DNBS, revealing distinct localization patterns with no signal overlap among the three channels. This highlights the feasibility of multicolor imaging and confirms that BT-DNBS selectively responds to intracellular biothiols without interference from nuclear or lipid-associated fluorescence. Furthermore, NEM pre-treatment significantly suppressed fluorescence activation, validating the high selectivity of BT-DNBS for biothiols. These results establish BT-DNBS as a promising tool for intracellular biothiol detection, offering high selectivity, low cytotoxicity, and strong fluorescence activation, with potential applications in monitoring biothiol dynamics in complex biological systems.

References

1. Jung H S, Chen X, Kim J S, et al. Recent progress in luminescent and colorimetric chemosensors for detection of thiols. *Chemical Society Reviews*, **2013**, 42(14): 6019-6031. DOI: 10.1039/C3CS60024F.
2. Lippert A R, New E J, Chang C J. Reaction-based fluorescent probes for selective imaging of hydrogen sulfide in living cells. *Journal of the American Chemical Society*, **2011**, 133(26): 10078-10080. DOI: 10.1021/ja203661j.
3. Wu G, Lupton J R, Turner N D, et al. Glutathione metabolism and its implications for health. *The Journal of nutrition*, **2004**, 134(3): 489-492. DOI: 10.1093/jn/134.3.489.
4. Refsum H, Smith A D, Ueland P M, et al. Facts and recommendations about total homocysteine determinations: an expert opinion. *Clinical chemistry*, **2004**, 50(1): 3-32. DOI: 10.1373/clinchem.2003.021634.
5. Bak D W, Weerapana E. Cysteine-mediated redox signalling in the mitochondria. *Molecular BioSystems*, **2015**, 11(3): 678-697. DOI: 10.1039/C4MB00571F.
6. McCully K S. Homocysteine and the pathogenesis of atherosclerosis. *Expert review of clinical pharmacology*, **2015**, 8(2): 211-219.
   DOI: 10.1586/17512433.2015.1010516.
7. Jones D P, Carlson J L, Mody Jr V C, et al. Redox state of glutathione in human plasma. *Free Radical Biology and Medicine*, **2000**, 28(4): 625-635. DOI: 10.1016/S0891-5849(99)00275-0.
8. Zheng W, Shen D, Pan Y, et al. Enhancing the peroxidase-like activity of ficin by rational blocking thiol groups for colorimetric detection of biothiols. *Talanta*, **2019**, 204: 833-839. DOI: 10.1016/j.talanta.2019.06.073.

Chapter 4. Summary and Conclusion

This dissertation presents a comprehensive study on the design, synthesis, characterization, and biological application of a novel fluorescent probe, **BT-DNBS**, for selective and sensitive detection of intracellular biothiols. The research bridges the fields of organic synthesis, photophysical characterization, and live-cell imaging, contributing valuable insights into the development of fluorescent probes for biological applications.

In Chapter 2, the synthesis and photophysical properties of **BT-DNBS** and its precursors were systematically examined. The probe was designed based on a D-π-A framework incorporating a DNBS group as the biothiol-responsive unit. **BT-DNBS** exhibited a large Stokes shift, excellent photostability, and a fluorescence "turn-on" mechanism upon reacting with biothiols. Density functional theory (DFT) calculations further elucidated the fluorescence quenching mechanism mediated by photoinduced electron transfer (PET), which is interrupted upon biothiol interaction, restoring fluorescence.

Chapter 3 extended the evaluation of **BT-DNBS** to biological applications, particularly in live-cell imaging. Cytotoxicity assessments confirmed the probe's biocompatibility at working concentrations, while fluorescence microscopy demonstrated its time-dependent fluorescence activation in A431 cells. Pre-treatment experiments with NEM validated the probe's selectivity for intracellular biothiols, emphasizing its utility for tracking biothiol fluctuations under physiological conditions.

The outcomes of this research underscore the significance of **BT-DNBS** as a biothiol-specific fluorescent probe, with potential applications in biomedical imaging and disease diagnostics. Its high selectivity, low cytotoxicity, and efficient fluorescence activation position it as a valuable tool for investigating biothiol-related physiological and pathological processes.

Looking ahead, further studies could explore the application of **BT-DNBS** in more complex biological environments, such as animal models or tissues, to validate its *in vivo* imaging capabilities. Additionally, structural modifications could be undertaken to

expand its detection scope to other biologically relevant analytes or to enhance its photophysical properties further.

In conclusion, this dissertation provides a solid foundation for the development of advanced fluorescent probes for biothiol detection, paving the way for innovative approaches in cell imaging and biological analysis

Acknowledgment

First and foremost, I would like to express my deepest gratitude to my supervisor, Associate Professor Koji Yamada, for his invaluable guidance, encouragement, and constant support throughout my doctoral research. His expertise and insights have been instrumental in shaping this dissertation.

I extend my sincere thanks to Professor Yusuke Ohba and Associate Professor Yoichiro Fujioka from the Department of Cell Physiology, Hokkaido University Faculty of Medicine, for their guidance and valuable advice regarding the cell imaging aspects of my work.

I am sincerely grateful to Professor Hisashi Sato and Assistant Professor Yuki Nakaya from the Faculty of Engineering, Hokkaido University, for their expert support and insightful discussions regarding the spectroscopic analysis in my research.

I would also like to thank Professor Shinichiro Noro and Professor Tatsufumi Okino for their guidance and valuable suggestions during the course seminars, as well as Associate Professor Kazuhiro Toyoda for his helpful feedback during these sessions.

My special thanks go to Assistant Professor Tatsuya Morozumi, whose constructive advice and guidance significantly contributed to the development and refinement of this dissertation.

I am deeply appreciative of the members of the Yamada Laboratory, whose friendship, collaboration, and support have greatly enriched my research experience.

Finally, I would like to express my sincere gratitude to my parents for their constant love, encouragement, and belief in me throughout this journey. Their support has been my greatest source of strength.

To all those who have contributed to my research and personal development, directly or indirectly, I extend my sincerest appreciation.